EXPERIMENTAL STUDIES OF THE ANOMALOUS SIGN REVERSAL IN THE VORTEX-STATE HALL CONDUCTIVITY OF $YBa_2Cu_3O_7$

Thesis by

David A. Beam

In Partial Fulfillment of the Requirements

for the Degree of

Doctor of Philosophy

California Institute of Technology

Pasadena, California

1997

(Submitted May 14, 1997)

Acknowledgments

To Gabby, Davie, and "Pufie" with love. Thank you for your love, prayers, support and sacrifice; and for the kaleidoscope...

And I acknowledge the prayers, support, training and assistance of my family.

This work was accomplished with the assistance of many others. Thank you.

Abstract

The DC vortex-state Hall conductivity (σ_{xy}) of $YBa_2Cu_3O_7$ single crystals is found to be independent of the density and orientation of correlated disorder. A universal σ_{xy} is observed for a given reduced temperature (T/T_c), magnetic field strength (H), and magnetic field orientation (θ), in five samples of different controlled defects, using direct current transport measurements. Transport scattering times (τ), derived from our data using the model describing the origin of the anomalous sign reversal in the vortex-state σ_{xy} by Feigel'man et al.[1], are consistent in magnitude with those derived from other measurements. Experimental issues unresolved by the Feigel'man et al. model are also presented.

The complex Hall conductivity, σ_{xy} ($\equiv \sigma_{xy}' + i\sigma_{xy}''$),of a $YBa_2Cu_3O_7$ thin film is measured in the frequency range of 100 Hz to 7 MHz. A frequency independent σ_{xy}', and a frequency dependent $\sigma_{xy}'' \propto \omega$ are observed, in agreement with an extension of the Feigel'man et al. model to finite frequencies, and using the Drude approximation[2] by Yeh[3]. Finally, the magnetic field (B) dependence of the complex Hall conductivity is compared with the model used by Spielman et al.[4], where the Hall conductivity was attributed solely to a quasiparticle contribution, predicting a linear dependence on B for $T \ll T_c$. We observe $\sigma_{xy}' \propto 1/B^{\alpha}$ and $\sigma_{xy}'' \propto 1/B^{\beta}$, where $\alpha, \beta > 1$, and $\alpha \neq \beta$, for $T < T_c$, in sharp contrast to the prediction from the model assuming only quasiparticle contributions. This provides support for any model which requires that both vortices and quasiparticles contribute to the Hall conductivity at low temperatures.

---

[1] M. V. Feigel'man et al., Pis'ma Zh. Teor. Fiz. **62**, 811 (1995) [JETP Lett. **62**, 835 (1995)].

[2] P. Drude, Annalen der Physik **1**, 566, and **3**, 369 (1900).

[3] Yeh, N.-C., private communications (1997).

[4] S. Spielman et al., Phys. Rev. Lett. **73**, 1537 (1994)

Chapter One: Introduction and Background

This chapter contains fundamental background information on superconductivity and the Hall effect. The Hall effect in superconductivity is also examined, as are defects and the effect of defects on flux motion. Finally, it provides motivation for the work in this thesis.

The most well known aspect of superconductivity was first observed in 1911 by Kamerlingh-Onnes, that of "zero" measurable resistivity below the superconducting transition temperature T_c. Forty-six years later Bardeen, Cooper, and Schrieffer (BCS) developed the first microscopic model explaining the mechanism of superconductivity. In April 1986, the age of "high-T_c" superconductors began. K. Alex Müller and J. George Bednorz, of IBM-Zurich reported (Zeitschrift Fur Physik) superconductivity in lanthanum-barium copper oxide at 30K, (which broke the then record-high superconducting transition temperature of 23 K). Their discovery led to studies of a new class of superconducting materials, structurally of the perovskite family (that is, materials with a structure similar to the naturally occurring mineral perewskite or $CaTiO_3$), and the awarding of the Nobel prize in physics in October 1987. In 1988, with the discovery of $YBa_2Cu_3O_7$, by M. K. Wu, with a transition temperature above the temperature of liquid nitrogen, "high temperature" superconductivity became a household concept with superconductors even in the hands of elementary and secondary school students. With that public attention, and the Nobel prize for Bednorz and Müeller the year before, a funding and publishing frenzy began. Some good observations were made, and hard

questions arose. Although experimental methods of old yielded many results, the many questions remain unanswered, including which other materials will superconduct. One phenomenon that was experimentally observed in high temperature superconductivity in 1988, and actually previously observed in conventional superconductors as early as 1967, and to this day remains unexplained is that of the unexpected sign reversal in the vortex-state Hall resistivity.

The Hall effect was discovered in 1879 by E. H. Hall (1879) while studying the force exerted on a current-carrying conductor in a magnetic field. Hall observed a potential difference from an electric field perpendicular to both the direction of the magnetic field, and the direction of current flow in the conductor. This phenomenon is now known as the Hall effect.

Measurement of the Hall effect in materials is traditionally done to gain insight about the mobile charge-carriers of a material. Hall effect measurements are used to determine the sign(s) of the mobile charge carriers, the carrier concentration(s), and, when combined with conductivity measurements, the carrier mobility(ies) within a material. That superconductors are more than ideal conductors and not normal metals required that new models of the Hall effect be developed. Models of the Hall effect in Type II superconductors were first developed by Bardeen and Stephen (1965) and Nozières and Vinen (1966). These models were considered mostly successful for more than twenty years. Anomalous results were observed as early as 1968, but little notice was taken.

Notice was taken in 1988 when Hall effect measurements of the superconducting perovskite materials yielded similar anomalous and unpredicted results (Galffy and

Zirgiebl, 1988; and additional references in chapter 2, Review of Experiments). Over a small temperature range near, but below the transition from normal conductivity to superconductivity, the Hall effect measurements indicated a reversal in the direction of the Hall electric field. That this observation of the sign reversal appeared in many different High-T_c materials, notice was finally taken, and theoretical attempts to explain the anomalous behavior were made(see references in chapter 2, Review of Theory).

In 1993, Hagen et al., in reviewing the literature, observed a commonality, a relation between two length scales, in all samples displaying the anomalous Hall effect. Those materials that had the length scale, the mean free path (how far the charge carrier travels, on the average, before scattering) of about the same size as the superconducting (reported by Hagen et al.(1993) and the authors' referenced therein, as the BCS) coherence length (a characteristic length scale in a superconductor analogous to the mean free path of normal metals) showed the anomalous behavior (Hagen et al., 1993) Hagen et al. used the BCS coherence length, ξ_o, following the convention of the references cited. Clearly, in high-temperature superconductors, sign reversal occurs near T_c, and therefore, reference should be made to the temperature dependent Ginzburg-Landau (GL) coherence length, $\xi(T) = \xi_o \left| 1 - T/T_c \right|^{-1/2}$.

The GL coherence length is intrinsic in a superconducting material and is therefore not easily adjusted. On the other hand, the mean free path is easily adjusted, without changing the fundamental material, by the introduction of defects. Defects also affect the motion of vortices. Recalling that the GL coherence length is temperature dependent, the temperature at which the coherence length is about the same size as the mean free path

can be shifted by changing the mean free path. Shifting the temperature at which the length scales are of the same size should then shift the temperature region where the sign reversal can be observed experimentally.

In 1994, during a conference in France, two theoretical groups, Khomskii and Freimuth (KF), and Feigel'man, Geshkenbein, Larkin, and Vinokur (FGLV), presented phenomenological models offering a possible explanation of the anomalous Hall effect. Two novel mechanisms were presented with an equivalent main result, the anomalous Hall effect in superconductors was due to a difference in the carrier density within the vortex core and far away from the core. Khomskii and Freimuth presented a mechanism of an electron redistribution required to maintain equilibrium of chemical potential throughout the superconductor in the mixed state. The essence of this requirement is that the core of a vortex is normal and the surrounding material outside of the core is superconducting, thereby requiring a redistribution of electrons between inside and outside of the vortex core, resulting in a difference in carrier density within and outside of the vortex core, to maintain the equilibrium of the chemical potential. FGLV had the same requirement of the difference in carrier density within and outside of the vortex core, but attributed the difference to the scattering carriers and momentum transfer. The experimental predictions for the direct current (DC) Hall effect are equivalent using these two models, and the FGLV model allows the incorporation of carrier scattering. The differences in the models are fundamental and are being tested by other groups. Furthermore, these models are not quantitatively rigorous. Even so, these phenomenological models give some insight to the microscopic mechanisms of the sign reversal.

Investigating the origin of the anomalous Hall effect is the main focus of this work. Twinned, fully oxygenated $YBa_2Cu_3O_7$ single crystals were used in the DC experimental studies of this work. A special class of static defects, the columnar (modeled as cylindrical) defects, were induced in some of the single crystals by high-energy heavy-ion irradiation. The initial motivation was to change the mean free path and study the effects of the change on the Hall resistivity and Hall conductivity. The columnar defects were known to induce anisotropy in vortex motion, in addition to that of the uniaxial anisotropy of the samples. Columnar defects are also strong vortex pinning sites in the vortex-state, and become scattering centers in the normal state. Further, the universality class of the vortex-solid to vortex-liquid transitions for samples with columnar defects differs from that of the as-grown twinned single crystals. Therefore, the effect of induced columnar defects on the Hall conductivity (σ_{xy}) is expected to yield important information for the origin of anomalous sign reversal in the vortex-state σ_{xy}. Detailed experimental observations and comparisons are made among the as-grown $YBa_2Cu_3O_7$ single crystals and those with various amounts and orientations of columnar defects. The DC Hall effect data and results are then used to test the validity of the work by FGLV through quantitative comparisons with their conclusions. The DC Hall effect measurements validate the requirement of an "anomalous" term introduced by FGLV. In addition, the magnitude of the transport scattering time derived from our data provides important information for the microscopics of the vortex dynamics and quasi-particle scattering in the vortex-state of high temperature superconductors. Alternating current (AC) Hall effect measurements are conducted to probe the origin of the anomalous term by making

dynamic observations. As elaborated in chapter 5 of this work, due to an equipment imposed constraint on the signal-to-noise ratio in the broadband frequency-dependent measurements, a $YBa_2Cu_3O_7$ thin film was used, instead of single crystals, for these measurements. The result obtained in the DC and AC experiments provide a clearer understanding of the vortex-state Hall conductivity of high-T_c superconductors.

$YBa_2Cu_3O_7$: Structure and Anisotropy

The structure of $YBa_2Cu_3O_7$ is layered with copper oxide planes sandwiched between Ba planes (typically denoted Cu1) and between Ba and Y planes (typically denoted Cu2) as shown in figure 1-1(a). This structure is a variation of the standard ABX_3 perovskite structure, as shown in figure 1-1(b), where A and B denote two types of cations, and X denotes the anion. $YBa_2Cu_3O_7$ has two phases, the orthorhombic phase and the tetragonal phase. The tetragonal phase ($a=b\neq c$), for $YBa_2Cu_3O_{7-x}$ when $x \geq 0.7$, is semiconducting. The superconducting phase of $YBa_2Cu_3O_7$ is obtained with T_c maximized in the orthorhombic phase ($a\neq b\neq c$).

$YBa_2Cu_3O_7$ is anisotropic along the principal axes of the structure. The anisotropy is evident in differences in the effective masses along these axes. $YBa_2Cu_3O_7$ is typically considered to be uniaxially anisotropic to high accuracy, particular for twinned single crystals and thin films. (The observation of an elongated shape of vortex cores in an untwinned $YBa_2Cu_3O_7$ single crystal, using scanning tunneling microscopy has been recently reported. One hypothesis explaining this observation is that there is an intrinsic

ab anisotropy with the ratio of the coherence lengths equal to 1.5 (a and b directions not distinguished). An alternative hypothesis is that the elongations reflect fluctuations in the position of the vortex line in preferential directions.) Therefore, for uniaxial symmetry, the effective masses are such that $m_a = m_b = m_{ab} \neq m_c$ where a, b, and c correspond to the conventional cuprate axes, and c is perpendicular to the CuO (or ab) planes. Whereas for the anisotropy in the ab plane, $m_a \neq m_b \neq m_c$, where again, a, b, and c correspond to the conventional cuprate axes, and c is perpendicular to the CuO (or ab) planes. That twinned single crystals are used, the orientation of a and b interchange throughout each sample, and only an averaged ab plane effective mass, m_{ab}, is observed in this experiment. The mass anisotropy ratio is

$$\varepsilon^{-2} = m_c / m_{ab} > 1.$$

For $YBa_2Cu_3O_7$, $\varepsilon^{-2} \approx 60$. For other cuprates, such as the bisthmuth compound, $Bi_2Sr_2CaCu_2O_{8-x}$, $\varepsilon^{-2} \approx 10^4$. The anisotropy of the $YBa_2Cu_3O_7$ structure results in anisotropic vortex state characteristics, and allows an additional degree of freedom in this work, the angle of the magnetic field relative to either the ab-planes or the c-axis. This anisotropy also appears in other measured or derived parameters.

Twinning

$YBa_2Cu_3O_7$ is processed at high temperatures. Upon cooling through about 700 °C, the crystalline structure of $YBa_2Cu_3O_7$ undergoes a phase transition from a tetragonal structure to an orthorhombic structure, and twin boundaries are formed with separate orthorhombic domains. Note, for fully oxygenated $YBa_2Cu_3O_{7-x}$, where $x < 0.1$, further annealing (for periods up to several months) in O_2 is necessary at 350 °C to 400 °C.

Basics of Superconductivity

The Vortex State

The vortex state derives its name from the screening currents that surround the quantized magnetic field flux lines upon the inclusion of these flux lines in a type II superconductor in the superconducting state. The perfect diamagnetism of a superconductor is valid as long as for a given temperature, the applied external field is below a critical field, H_{c1}, the lower critical field, or for a given field, below a critical temperature, T_{c1}, the lower critical temperature. Beyond this critical field (or critical temperature), the magnetic field penetrates the sample, since the superconducting system has a lower overall energy with the penetrating magnetic field than by excluding the field. (Note that bulk type I superconductors are considered to have only one critical field designated as H_c, with the numeral not present. Type I superconductors transition to the

normal state when the applied magnetic field is above H_c. Type II superconductors transition to the mixed state, a superconducting state with penetrating magnetic field, when the applied magnetic field is above H_{c1}, and transition to the normal state when the applied magnetic field is above the upper critical field, H_{c2}, or for a given field, above a critical temperature, T_{c2}, the upper critical temperature. See type I and type II below.) The magnetic field entering the superconductor is quantized into units called fluxoids, ϕ_o. Each fluxoid has a value, $\phi_o = 2.07 \times 10^{-15}$ Tesla-m^2, and is surrounded azimuthally by a superconducting supercurrent, a vortex. The vortex (interchangeably called a flux line) may be modeled as cylinder of normal material of radius equal to the coherence length, ξ, with the magnetic field inside. (More precisely, the magnetic field decays exponentially from the center (axis) of the vortex and extends into the sample.)

The vortex state of high temperature superconductors has two main phases, the vortex-solid and the vortex-liquid phases. (Conventional type II superconductors have only a vortex solid phase, except possibly near the mixed state to normal state transition.) The thermal fluctuations of the flux lines, as a result of the high temperatures at which the mixed state can occur in high temperature superconductors, allow the vortex solid to become "unstable." The vortex-solid to vortex-liquid transition temperature is most easily described, using the Lindemann criterion (Kwok et al., 1992) relative to the stability of crystalline lattices. (Note, only a vortex solid in a pure, no defects present, crystal forms a vortex lattice. Defects result in a "glass" to be formed instead of a lattice.) The lattice becomes unstable when the size of the fluctuations (the root mean squared amplitude of the vortex displacement, $\sqrt{(<u^2>_{th})}$) increases beyond a fraction, the Lindemann number c_L,

of the lattice constant, a_o. Greater instability results in a "liquid" where flux lines become mobile in the long time scale. Similarly, a vortex solid is considered solid when the mean thermal displacement of a vortex flux line remains near its equilibrium position in the solid. Another important criterion of a vortex-solid is its finite shear modulus, c_{66}. In the liquid state, $c_{66} = 0$.

Flux Quantization

Associated with the superconducting state is a macroscopic complex order parameter, a pseudowavefunction, ψ with amplitude and phase. For any closed path in a superconductor, the phase is restricted to integral multiples of 2π. Taking a closed path around a flux line results in a total flux enclosed of $(e^*/h)\phi$, where e^* is the charge of a Cooper pair, $e^* = 2e$, h is Planck's constant, and ϕ_o is a flux quantum. Equating the two yields,

$$2\pi n = (e^*/hc)\phi = (e^*/hc)n\phi_o.$$

Therefore,

$$\phi_o = hc/e^*.$$

The London Penetration Depth

The London penetration depth $\lambda_L = \left(\frac{mc^2}{4\pi ne^2}\right)^{1/2}$, and is valid over the temperature region from absolute zero to the transition temperature, T_c for fields not significantly suppressing the order parameter. In an anisotropic superconductor,the penetration depths along different principal axes will be different. Another perspective of the penetration depth is given in a review article by Blatter et al.(1994),

> the penetration depth characterizes the decay length of currents rather than magnetic fields: a current density, j, directed along the ab plane (along the c-axis) can be modified on a scale λ (λ_c)

The London penetration depth at zero temperature is $\lambda_L \approx 1400$ Å in the ab plane for a twinned $YBa_2Cu_3O_7$ single crystal. Considering the anisotropy of the $YBa_2Cu_3O_7$ structure, for the mass anisotropy ratio ε,

$$\lambda_c = \lambda_{ab}/\varepsilon,$$

where λ_c is the penetration depth along the c-axis, λ_{ab} is the penetration depth in the ab-plane, and $\varepsilon^{-1} \approx 5 - 7$.

Coherence Length

The coherence length, ξ, is a phenomenological parameter and is the smallest scale in the microscopic solution of the many-body problem. It represents the size of a Cooper pair. Consequently, the coherence length is taken to be the physical length scale of a given disorder potential (Blatter et al., 1994). (The actual disorder potential may be smaller, but the vortex line cannot resolve length scales shorter than ξ.). Historically, there are three different but related coherence lengths in the literature. The coherence length can be estimated by using the Fermi velocity, v_F and the uncertainty principle as follows,

$$\xi = ahv_f/kT_c,$$

from

$$\xi \approx \Delta x = h/\Delta p, \text{ and } \Delta p = kT_c/v_f, \text{ where } a \sim 0.18 \text{ (Tinkham, 1975)}$$

The Pippard coherence length is adjusted by the mean free path,

$$1/\xi = 1/\xi_o + 1/l,$$

where l is the mean free path, and ξ_o is the coherence length in the pure material.

The BCS coherence length is given in terms of the BCS energy gap, $\Delta(0)$, and the Fermi velocity by the following expression,

$$\xi_o = h v_F / 2\pi^2 \Delta(0),$$

where v_F is the Fermi velocity, and $\Delta(0)$ is the BCS gap energy. The BCS coherence length of $YBa_2Cu_3O_7$ single crystals at 0 K is, $\xi_{BCS} \approx 16 - 30$Å at 0 K (Blatter et al., 1994)

The Ginzburg-Landau coherence length, ξ_{GL}, is related to the BCS coherence length as

$$\xi_{GL}(T) = h/(2\pi \mid 2m^*\alpha(T) \mid^{1/2})$$

$$\rightarrow \xi_o \text{ if } T \ll T_c,$$

where ξ_o is the BCS coherence length, and $\alpha(T)$ is an expansion coefficient in the Ginzburg-Landau theory (see, e.g. Tinkham, 1975). ξ_{GL} is derived from the Ginzburg-Landau equations. For the majority of this work, the BCS coherence length will be used.

Anisotropy of the $YBa_2Cu_3O_7$ structure requires that

$$\xi_c = \varepsilon \xi_{ab},$$

where ξ_c is the coherence length along the c-axis, ξ_{ab} is the coherence length in the ab-plane, and ε is the mass anisotropy ratio. For $YBa_2Cu_3O_7$, $\xi_{ab} \approx 16 - 30$Å, and $\xi_c \approx 2 - 4$Å, at 0 K (Blatter et al., 1994)

The Ginzburg-Landau Parameter, κ

$\kappa = \lambda/\xi_o$, is the ratio of the penetration depth to the coherence length. For $YBa_2Cu_3O_7$ single crystals, $\kappa \approx 70$. The Ginzburg-Landau parameter is used to define the dividing line between type I superconductors and type II superconductors, $\kappa = 1/\sqrt{2}$. Type II materials have $\kappa > 1/\sqrt{2}$, while type I materials have $\kappa < 1/\sqrt{2}$.

Type I versus Type II Superconductors

It was mentioned above that the expulsion of an applied magnetic field, the Meissner effect, occurs below the transition temperature when the applied magnetic field is not too strong. Above a certain field strength, but still not too strong, one of two things happen. Either the superconductor (type I) transitions to the normal state, or the superconductor (type II) allows the magnetic field to penetrate while remaining in a superconducting state.

In a type I superconductor, no magnetic field is allowed inside while superconducting (except for a surface layer of thickness λ_L within which screening currents are induced), and the material transitions to the normal state when the magnetic field becomes larger than the critical field, and the applied magnetic field enters the entire sample. (Note: there are subtleties which under certain conditions and geometries allow an intermediate state, such as an infinite flat slab, where the applied magnetic field over part of the surface of the superconductor may exceed the applied field.) In type II

superconductors, there is this same "no penetration zone" in the low-field limit, $H < H_{c1}$, after which as the applied magnetic field strength increases, the material continues to superconduct while allowing the partial penetration of the applied magnetic field, forming a mixed state. At a sufficiently high magnetic field, the type II material also becomes normal and allows the external applied magnetic field to penetrates the entire sample. The fundamental differences between type I and type II superconductors are evident from phase diagrams of applied magnetic field versus sample temperature (see figures 1-2(a) and (b)).

Type I superconductors are typically pure metallic elements, such as Hg, Sn, and Pb. The critical field of type I superconductors is typically $H_c \sim 0.1$ Tesla, and therefore the critical current, j_c, the current above which the type I superconductor becomes normal, is low, as current produces magnetic field. The type I superconductors typically have low thermodynamic critical temperatures, as an amount of condensation energy equal to $H_c^2/8\pi$ is used up expelling the magnetic field.

In type I superconductors, for a given shape, an intermediate state can appear, depending on the demagnetizing factor. If the demagnetizing factor is zero, as for a long thin sheet or a long thin cylinder, the magnetic field along the surface of the superconductor is everywhere equal to the applied magnetic field, and the intermediate state does not occur. For shapes of which the demagnetizing factor is not zero, for example a sphere, the field over part of the material will exceed the applied field, and in these regions may exceed the thermodynamic critical field, H_c, causing these regions to become normal while the rest of the material remains superconducting. Again, this is a

shape specific condition where the applied field H_a is less than H_c. When the applied field is greater than H_c, the type I superconductor transitions to the normal state always.

Type II superconductors, rather than completely expelling the magnetic field or becoming normal have a third option, the mixed state. The mixed state allows the magnetic field to enter, resulting in less energy costs than complete expulsion. Type II superconductors are generally alloys or compounds (with the exception of niobium and vanadium which are type II elements). The high temperature type II superconductors typically have upper critical fields, $H_{c2}(T=0) \sim 10^2$ Tesla, allowing for higher critical currents. The mixed state is formed when $H_{c1} < H_a < H_{c2}$. For thin samples, if the field is applied parallel to the surface and when $H_{c2} < H_a < H_{c3}$, a surface superconducting state is formed.

In the mixed state, magnetic fields enter the type II superconductor in quantized fluxoids. Each fluxoid is screened with a circulating supercurrent, call a vortex.

Conventional versus High Temperature Type II Superconductors in the Mixed State

Conventional Type II superconductors are characterized by low thermodynamic critical temperature, $T_c \sim 10^0 - 10^1$, $\kappa \sim 10^0$. (Amorphous- Mo_3Si, a conventional type II superconductor with a T_c of 7.8K, has a large $\kappa \approx 80$, since the mean free path $l << \xi_o$.) The phase diagram of the conventional type II superconductors has well defined transitions and critical fields between the Meissner state and the mixed state, and the mixed state and the normal state. The resistive transition versus temperature of

conventional type II superconductors is also relatively sharp, even when a magnetic field is applied.

High temperature superconductors, HTS, are characterized by large penetration depths and short coherence lengths, resulting in large $\kappa >> 1$, ($\kappa \sim 10^2$). The thermodynamic critical temperature, also called the transition temperature, $T_c \sim 10^2$. The large fluctuation effects allow superconductivity to remain well above T_c, so that the upper critical field, H_{c2} is no longer an experimentally well defined quantity. Below H_{c2}, there are two vortex phases, the vortex-liquid phase at higher temperatures, and the vortex solid phase at low temperatures. In the presence of defects, the glassy vortex-solid is described as a vortex-glass, if random point or cluster defects are present, a Bose-glass if the defects are dominated by columnar defects (see Defects, below), and a splayed-glass, if columnar defects are introduced at more than one orientation. The vortex-solid to vortex-liquid transition line, $B_{VS\text{-}VL}(T)$ separates the vortex-solid phase from the vortex-liquid phase. The vortex-liquid phase may be approximately divided into a pinned liquid region, and an unpinned liquid region. The vortex dynamics in the pinned liquid region is characterized by thermally assisted flux flow (TAFF), and the unpinned liquid region is characterized by flux flow (FF). The superconductor is considered to be truly superconducting only in the vortex-solid phase (see Flux Creep, TAFF, and FF below). While the resistive transition versus temperature of HTS is sharp in zero applied field, the large fluctuation effects cause a broadening of the transition in finite magnetic fields.

Flux Creep

There is a finite probability for flux lines to creep, even when in the pinned regime, if sufficient thermal energy is available to allow flux lines to "jump" among pinning sites. The Anderson-Kim flux creep theory (Anderson, 1962; Anderson and Kim, 1964) assumes that flux lines jump in bundles. This collective motion is assumed because of the correlation among flux lines. In the presence of a gradient in the flux density, the jumps will occur in the direction of the pressure gradient, and a net creep velocity will develop. The flux creep regime is characterized by motion,

$$v = v_o \exp[-E_a/k_B T],$$

where v is the drift (or creep) velocity, v_o is the drift velocity in the absence of barriers, E_a is a temperature and magnetic field dependent activation energy, k_B is the Boltzmann constant, and T is the temperature. Flux creep causes a decay in the magnetization or an increase in the magnetic field in the hollow superconducting cylinder experiment. (If a magnetic field sensor is placed inside a hollow superconducting cylinder, as the external field (normal to the cylinder axis) is increased, no field is initially measured inside the cylinder. Once the lower critical field is reached, a field is present inside the cylinder. The presence of flux creep is indicated by an increasing of the internal field as flux tubes jump across pinning barriers.)

Thermally Assisted Flux Flow (TAFF)

Thermally assisted flux flow (TAFF) describes an activated vortex dynamics in the small driving force limit. In this limit, finite barriers to vortex motion exist. The TAFF regime is characterized by the relation (Kes et al., 1989)

$$E = \frac{vB}{c} = \frac{\nu_o \omega B}{c}\left\{\exp\left[\frac{-(U_o - \Delta W)}{k_B T}\right] - \exp\left[\frac{-(U_o + \Delta W}{k_B T}\right]\right\} = 2\frac{\nu_o wB}{c}\sinh(\frac{\Delta W}{k_B T})\exp\left[\frac{-(U_o}{k_B T}\right]$$

where both forward and backward hopping probabilities are considered. Here w is the hopping distance, ν_o is the attempt frequency, $\Delta W = jBwV_c/c$ is the work done by the applied current density j, V_c is the correlated volume of vortex bundles, and $U_o = j_c B r_p V_c/c$, where j_c is the critical current density, and r_p is the pinning range of vortex bundles. In the small current limit, the sinh factor becomes $\propto$ j, so

$$E = \rho j, \text{ where } \rho \propto \exp(-U_o/T),$$

in the small current limit, where U_o is a function of current density, hopping distance, pinning strength, and current density. In the TAFF regime, thermal energy allows vortex motion in the presence of finite energy barriers.

Flux Flow(FF)

The flux flow (FF) regime is where the barriers inhibiting vortex motion can be neglected. The FF motion is characterized by

$$E = \rho_{flow}(B)j,$$

where $\rho_{flow} = \rho_n B/H_{c2}$, and j is the applied current density.

Depinning Temperature/Current

Depinning occurs when the pinning force density, F_{pin} is no longer sufficient to pin the flux line (or vortex). The Lorentz force density, F_L, on vortices is

$$\mathbf{F}_L = \mathbf{j} \times \mathbf{B}/c,$$

(or on a single vortex, $\mathbf{F}_L = \phi_o \mathbf{j} \times \mathbf{n}/c$), where **j** is the applied current density. When $F_L > F_{pin}$, depinning occurs. This can be caused by a current density, j, greater than the critical current density, j_c,

$$j > j_c = F_{pin} / B.$$

Similarly, thermal fluctuations interfere with pinning sites by affecting the pinning potential and changing the dynamics of the system. Small thermal displacements average the pinning potential over the mean amplitude of the displacements, $\langle u^2 \rangle_{th}^{1/2}$. For the mean amplitude of the displacements greater than the size of the pinning potential, fluctuations smooth the pinning potential, and pinning strength is reduced. The depinning temperature for a given field-temperature condition (the depinning line) is determined by (Blatter et al, 1994)

$$\langle u^2(T_{dp}) \rangle_{th} \approx r_p^2,$$

where r_p is the pinning range.

The Hall Effect

The Hall Effect in Normal Metals

The Hall effect occurs in current-carrying materials in an applied magnetic field, in which part of the field is perpendicular to the current. The moving charges, of which the current is comprised, experience a force due to the electric field driving the current, and a force due to the charges moving through a magnetic field. The direction of the force due to the motion of charges through a magnetic field is at a right angle to the direction of

motion of the charges and the component of the magnetic field perpendicular to the direction of motion of the charges.

$$\mathbf{F} = q(\mathbf{E} + \mathbf{v}\mathrm{x}\mathbf{B}/c),$$

where **v** is the velocity of the charges, **E** is the electric field driving the current, and **B** is the magnetic induction. This force causes a deflection in the motion of the charges, and in opposite directions for opposite sign of charges. As the charge builds up along the transverse direction, an additional electric field, the Hall field, increases. The orientation of this Hall field is such that it opposes the force on the charge carriers resulting from their motion in the magnetic field, and thereby opposes the transverse motion of additional charge. The Hall voltage, in a normal metal, results from a balance of the two forces on the charge carriers. A transverse voltage measurement, made perpendicular to both a component of the direction of the current and a component of the applied magnetic field which is also has a component perpendicular to the direction of the current, in normal metals will indicate the high and low potential sides of the potential difference, from which is derived the sign of the moving charges. Varying the field allows the determination of the number of moving charges from the relation,

$$V_H = BI/tnec,$$

where n is the number density of carriers, B is the magnitude of the magnetic induction, I is the applied current, t is the sample thickness, and V_H is the measured transverse potential difference. The relation between Hall voltage and current is linear in magnetic field. The slope of the line of Hall resistivity, B/nec, as a function of the magnetic induction gives the inverse of the charge density. The carrier density is derived with a knowledge of the magnitude of charge per carrier. This explanation of the Hall effect is valid for normal metals with one type of carrier, and is even applicable within the vortex cores of most conventional Type II superconductors.

The Hall Effect in Type II High-Temperature Superconductors

A simple picture of the Hall effect in conventional type II superconductors (other than vanadium and niobium when $l \sim \xi_o$) is shown in figure 1-4 (Reed et al., 1965). The sign of the Hall voltage in the normal state (where the Hall voltage is linear in field) is the same as that in the superconducting state (the Hall voltages at applied magnetic fields less than the region where Hall voltage versus field is linear).

The Hall effect in vanadium and niobium when $l \sim \xi_o$, conventional Type II superconductors, and in the cuprates (those superconductors with the common copper-oxide planes in the peroskvite structure) is anomalous, as shown in figures 1-5(a) and (b) (Rice et al., 1992; Hagen et al., 1993). Where the Hall effect in an ordinary metal yields a Hall voltage of always one sign for each material, in high-temperature superconductors, in the conventional elemental superconductors vanadium and niobium, and in the

conventional amorphous Mo_3Si, the vortex-state Hall effect shows a sign reversal for some fields and temperatures.

The magnetic field enters the superconductor as quantized flux lines. The magnetic field of each flux line is screened by a circulating supercurrent. A typical model has the region on the axis of the flux line is considered to be completely normal. The region far outside the circulating flux line is considered to be completely superconducting. The region between shows a mixture of both states. That is, on the axis, the Ginzburg-Landau (GL) order parameter is zero, and it increases in value until its square equals the effective superfluid density far from the axis.

The magnetic field enters the superconductor as quantized flux lines. The magnetic field of each flux line is screened by a circulating supercurrent. The region on the axis of the flux line is considered to be completely normal. The region far outside the circulating flux line is considered to be completely superconducting. The region between shows a mixture of both states. That is, on the axis, the Ginzburg-Landau (GL) order parameter is zero, and it increases in value until it square equals the effective superfluid density far from the axis.

For simplicity, a vortex core is approximated by a normal cylindrical entity of radius ξ_o, which is completely normal inside and fully superconducting outside. Early theory (Bardeen and Stephen, 1965; Nozieres and Vinen 1966) provided different mechanisms to explain a current flow within the vortex core, perpendicular to the direction of the flux line. Both mechanisms allowed vortex flow only when a real current flow was present.

Bardeen and Stephen (1965) modeled that the transport current, **j**, produces a force, F, a Lorentz force, that drives flux motion. This Lorentz force was balanced by a frictional force, f, such that $F + f = 0$. Normal electrons passing through vortex cores experience the usual magnetic force, and a Hall voltage results. The vortex velocity then has a small component parallel to the transport current, J, and the Hall effect in flux flow is of the same sign as that of the normal state. "... the Hall angle as measured in the mixed state should be equal to that of the normal metal for a field equal to the field in the core of the vortex." (Bardeen and Stephen, 1965).

Nozieres and Vinen (1966) wrote the paper "... to stress certain important concepts (e.g. Magnus force, and the nature of the friction force) and to emphasize that, on the basis of results that can at present be rigorously proved, other descriptions of vortex motion are possible besides that proposed by Bardeen and Stephen." The Magnus force was balanced by a friction force such that again the total force on each vortex is zero and the vortex drift velocity is a constant.. The Hall voltage comes from the motion of a normal core through a magnetic field, with the resultant Hall angle independent of the applied field below H_{c2}. Clearly, neither the theory by Bardeen and Stephen nor that by Nozières and Vinen can account for the observed sign reversal in the vortex-state Hall resistivity of high-temperature superconductors.

Dynamics of Vortices

Although there are many descriptions of the dynamics of vortices, there are a few commonalities as described here from Blatter et al.(1994). The description here is limited for vortices in those materials which produce a small Hall force. This description also neglects the effects of disorder and critical fluctuations. For a vortex system with an applied current density, **j**, the flux lines move as a result of depinning by a Lorentz force:

$\mathbf{F}_L = -\eta\mathbf{v}$, where **v** is the steady-state velocity, and $\mathbf{v} = \mathbf{j} \times \mathbf{B}/c\eta$.

A finite electric field is generated due to flux motion:

$\mathbf{E} = \mathbf{B} \times \mathbf{v}/c$.

Power is dissipated for **j** // **E**, such that

$P = \mathbf{j} \bullet \mathbf{E} = (\mathbf{j} \times \mathbf{B})^2/c^2\eta$.

Using the Bardeen-Stephen [1965] friction coefficient $\eta \sim BH_{c2}/c^2\rho_n$,

$P = \rho_n j^2 B/H_{c2}$ for $\mathbf{j} \perp \mathbf{B}$.

This is equivalent to the dissipation of a normal metal reduced by the fraction B/H_{c2}.

For dissipation-free current flow, $\mathbf{v} = 0$, even though $\mathbf{F}_L \neq 0$. This comes about in the presence of some pinning force, F_{pin}, if $F_{pin} > F_L$ where a depinning critical current density is defined as

$$j_c = cF_{pin}/B.$$

The pinning force can be the result of quenched disorder or defects. The ratio of the depinning critical current density, j_c, to the depairing critical current density, j_o, characterizes the strength of the quenched disorder.

Defects

Although there are three main classes of disorder, quenched, thermal and quantum (Blatter et al., 1994), this work only examines the effects of the quenched disorder on the vortex-state Hall effect. Thermal disorder has the obvious effect of flux creep at any finite temperature, if the energy barrier is finite, even for current densities less than the depinning critical current density. The result of thermal disorder is dissipation, if in a pinned vortex liquid regime. However, thermally-induced dissipation will not exist in a vortex-solid with infinite barriers against flux creep. Thermal disorder also has the effect of causing the vortices to average disorder potentials over the spatial extent of the thermal

displacement. Thermal disorder thereby reduces the pinning efficiency of quenched disorder and the depinning critical current density, j_c. Macroscopic quantum fluctuations at very low temperatures are not relevant to the Hall effect in the vortex-liquid state, and are therefore neglected in this work.

Defects are any variance in the regular crystalline structure of a superconductor. Defects occur intrinsically, as a result of growth conditions, including doping, and extrinsically, as a result of radiation or other intentional damage. There are three basic types of defects, point defects, line defects, and planar defects. Point defects are considered to be random, and typically involve either one atom, or a small cluster of atoms. They naturally occur due to vacancies or substitutions during growth, and may be induced via irradiation, either electron, proton, or ion implantation (Audouard et al., 1990; Civale et al., 1991, Konczykowski et al., 1991; Jiang et al., 1993, Tombrello, 1995). Line defects are extended variances in the regular crystal structure. Intrinsically, they include edge dislocations (an extra plane of atoms introduced within the crystal) and screw dislocations (visualized as the helical pattern of the end of a screw). Induced line defects include columnar (cylindrical) defects which are induced by heavy ion irradiation at sufficient energies. Although the areal distribution of the induced linear defects is random in high temperature superconductors, each defect is correlated along its length.

Quenched disorder, also called static disorder, affects the dynamic behavior of vortices in the thermally activated flux flow regime (TAFF) and in the pinned liquid regimes, and reduces the long range order of the triangular Abrikosov flux lattice, changing the vortex-solid phase into a glassy state. The effect of quenched or static

disorder on vortices (and Hall conductivity) in the flux flow regime is currently debated (Vinokur et al., 1993; Samoilov et al, 1994; Khomskii and Freimuth, 1995; Feigel'man et al., 1995; Kang et al., 1996; Smith and Lobb, 1997; Samoilov, 1997). There are clear observations of a reduction in the magnitude of the resistivities (both longitudinal and transverse), but the effect of static disorder on the Hall conductivity is disputed. An investigation of the effect of static disorder will be studied in detail in this work.

Quenched disorder consists of random points defects, twin boundary defects, and columnar defects. In addition, the layered structure in high-temperature superconductors is an intrinsic pinning mechanism when the applied magnetic field is aligned with the ab plane. In the current discussion, we will focus on the effects of the first three.

Weak Pinning: Point Defects

The effect of random point defects on a single vortex line is now considered. For simplicity, we will only consider an isotropic superconductor in this discussion. Again following the development of (Blatter et al., 1994), for an isotropic superconductor, the vortex line is elastic. Individual point pins compete with one another. Only inhomogeneities in the density and force of the pins yield a net pinning force on a flux line. The total force of random pins acting on the vortex line is (Blatter et al., 1994)

$$F_{pin}(L) = (f_{pin}^2 n_i \xi^2 L)^{1/2} \propto L^{1/2},$$

where n_i ~ the volume density of pins, f_{pin} is the local pinning force per defect, ξ ~ the superconducting coherence length, comparable to the physical length scale of the disorder potential (since the vortex line cannot resolve lengths smaller than this), and L is the length of the vortex. This pinning force competes with the Lorentz force, F_L. For a rigid vortex, the Lorentz force will eventually win for long L and the vortex will remain unpinned, as (Blatter et al., 1994)

$$F_L = j\phi_o L/c \propto L.$$

For an elastic (non-rigid) flux line, elastic deformation allows the flux line to find the most favorable position in the random potential. The bending has a cost in elastic energy. The corresponding pinning energy gain is (Blatter et al., 1994)

$$E_{pin} \sim F_{pin}(L)\xi.$$

Under equilibrium conditions, the pinning and elastic energies for a given length should be equal. For a greater length than the given length, the energy cost will be greater than the gain by pinning. The given length is called the collective pinning length, L_c. Therefore, for a vortex of length $L > L_c$, the vortex deforms elastically to an optimal local configuration up to some length L_c. The vortex then "segments" into length L_c, each of which is independently pinned. Each segment therefore competes with $F_L(L_c)$ (Blatter et al., 1994).

The above considered the effect of random point pinning on a single vortex line. If multiple vortices are now considered, then vortex-vortex interactions will compete with vortex-random point pinning interactions. In a dense vortex liquid, that is with many vortices present, the vortex-vortex interaction will be greater than the vortex-random point pinning interaction. Since the vortex-vortex interaction is weak when compared with temperature effects on a vortex-liquid, the effect of a random point potential is negligible on a vortex-liquid.

Restating, disorder is always relevant in the vortex solid phase, causing the vortex lattice of a homogeneous system to become a vortex-glass in the presence of disorder, with $\rho(j\rightarrow 0)\rightarrow 0$, following the collective flux-creep theory by Feigelman et al. (1989) and Blatter et al. (1994). Disorder is irrelevant in the flux flow regime which has a linear response resistivity, $\rho(j\rightarrow 0) > 0$. Just above the vortex-solid to vortex-liquid phase transition, the liquid is viscous and may be characterized by a plastic deformation time (Blatter et al., 1994). The plastic deformation time, t_{pl}, is an inhomogeneity duration time, such that any defect-induced inhomogeneity in the vortex system becomes irrelevant for time scales $t > t_{pl}$. If the plastic deformation time is greater than the vortex-pin interaction time (t_{pin}), $t_{pl} > t_{pin}$, the liquid can be pinned over the time scales $t < t_{pin} < t_{pl}$, with $\rho(j\rightarrow 0) \sim \rho_o \exp(-U_{pl}/T) << \rho_{flow}$. (TAFF regime), where U_{pl} is the plastic deformation energy. As $t_{pl} \leq t_{pin}$, the inhomogeneities are no longer relevant, and the system crosses over to the unpinned liquid with $\rho(j\rightarrow 0) \sim \rho_{flow}$ (FF regime). Suggestive experimental evidence for such a crossover in the vortex-liquid state has been reported in the resistive measurements of $YBa_2Cu_3O_7$ single crystals. A "kink" in the resistivity versus temperature data (Kwok

et al., 1992, Fleshler et al., 1993) is attributed to the crossover between the pinned liquid at low temperatures and unpinned liquid at high temperatures. T_k is the temperature where

$$t_{pin}(T_k) \sim t_{pl}(T_k) \sim t_{th}(T_k)\exp(U_{pl}(T_k)/T_k),$$

where t_{th} is the thermal fluctuation time associated with the short-scale elastic deformation, the thermal relaxation time for vortices. This discussion follows that of (Blatter et al., 1994).

Strong Pinning

Strong pinning results from extended defects. Twin boundaries (intrinsic) and columnar (induced) defects are in this category. Extended defects are also known as correlated disorder, since along the direction of the extension, the disorder is the same at each point. This is fundamentally different for point disorder. The pinning force of random point disorder sums proportional to $L^{1/2}$ (Blatter et al., 1994). The pinning force of extended disorder sums proportional to L for a single vortex aligned with the extended disorder (Blatter et al., 1994).

Enhanced pinning by correlated disorder has been observed, as has the anisotropy of the pinning effect (Blatter et al., 1994). When the field is aligned with the correlated disorder, enhanced pinning appears as an increase in the critical current density, j_c, an

increase in the depinning temperature, T_{dp}, and as a shift in the vortex-solid to vortex-liquid transition line towards higher temperatures (Blatter et al., 1994; this work chapter 4). One consequence of the strong pinning sites is the reduction in the resistivity in the flux-flow regime. Blatter et al. have attributed this phenomenon to an additional indication of enhanced pinning. Others (Iye et al., 1989; Kwok et al. 1990; Fleshler et al., 1993) interpreted the drop in the flux-flow resistivity for samples with columnar defects as a suppressed vortex dissipation within the TAFF regime. For strong pinning systems, the shift in the vortex-solid to vortex-liquid transition line results in a slower onset of vortex dissipation, such that the linear (or Ohmic) resistivity, ρ_{lin}, is effectively shifted to higher temperatures, giving rise to a reduction in the flux-flow resistivity along the complete curve below T_c. It is important to realize that there is no longer any pinning in the flux-flow regime, so the reduction in ρ_{lin} does not imply that vortices are still pinned by columnar defects.

While twin boundaries are a common occurrence during the growth process of $YBa_2Cu_3O_7$ due to its orthorhombic structure, columnar defects can be induced in almost any material, by high energy heavy-ion irradiation. Additionally, the suppression of the order parameter within columnar defects (which are at best, nonsuperconducting material, possibly insulating) appears to be stronger than that caused by twin boundaries (boundaries between superconducting orthorhombic domains). Consequently, columnar defects result in a marked increase in the critical current (Civale et al., 1991; and Konczykowski et al., 1991), and a shift in the vortex-solid to vortex-liquid transition line towards higher temperatures and fields (Jiang et al., 1994; and Reed et al., 1996). In

comparison, proton irradiation results in pointlike or cluster defects which yield an increase in the critical current density, j_c, and smaller shifts in the vortex-solid to vortex-liquid transition line (Jiang et al., 1993).

Twin Boundaries

The effect of twin boundaries (or twin planes) on the motion of vortices is undecided in the literature. Under certain conditions, the pinning appears to be enhanced. Under others, it appears to be reduced. Most studies have indicated that pinning is enhanced by the twin boundaries, (see references in Blatter et al., 1994; e.g. Kwok et al., (1990) saw a drop in the resistivity within the TAFF regime, Gyorgy et al., (1989) via torque experiments; Liu et al., (1991) in magnetization experiments; and Vlasko-Vlasov (1994) in magneto-optical experiments, where the vortices accumulated on one side of the twin boundaries and depleted on the other side, with some entering the channel along the twin boundary well). Duran et al. (1992) analyzed the results of real time imaging experiments of flux profiles and suggested that the twin planes provided channels for flux penetration, and possibly reduce pinning. Gurevich (1992) observed the attraction of the vortices to the twin boundaries, and (Blatter et al., 1994) deduced that the order parameter was reduced, the vortices elongated along the boundaries, and therefore, pinning was reduced. These seemingly contradicting effects of twin boundaries on vortex dynamics may be understood in terms of the following simple picture. Energetically speaking, twin boundaries are sites with a reduced superconducting order parameter, and

therefore are preferred channels for vortex penetration if the external field is greater than the magnetic induction of the superconductor. However, once an equilibrium vortex state is established, it is energetically more favorable to place more vortices in the twin boundaries. Furthermore, if the external field is reduced or the temperature is raised, vortices away from the twin boundaries will diffuse out first due to energetic considerations, and the twin boundaries appear to be pinning sites. In addition, at high temperatures it is possible that dimensional reduction of vortex fluctuations due to the presence of twin planes can occur for vortices pinned by twin boundaries. The dimensional reduction results in reduced thermal fluctuations, giving rise to less thermal smearing of the pinning potential and therefore more efficient pinning. This reduced thermal smearing effect may be most evident at higher temperatures. The dimensional reduction follows from Blatter et al.'s (1994) argument that the magnetic field aligned with the plane has increasingly large segments trapped within the wells of the TB's. The partial trapping in the potential wells suppresses transverse thermal fluctuations, leading to enhanced pinning of the trapped segments.

Columnar Defects

Columnar defects are considered the most versatile and strong pinning sites. The columnar defects are considered versatile in that they can be induced into any sample by high energy (5 GeV) heavy-ion irradiation. Their pinning strength derives in that they have the ability to trap an individual vortex along its linear dimension, and yet the

columnar defects damage only a minimal amount of superconducting material for this ability. If the energy of the heavy-ions is sufficiently large, the columnar defects are columns of nonsuperconducting material of diameter ~ ξ, the vortex core size. If the ions are not heavy enough, or if the energies are not sufficiently high, the induced damage will be "sausage like" or even worse. (Note, although the actual columnar defect diameter may be less than ξ, ξ is the smallest length that the vortex can resolve, so the columnar defect potential is effectively smeared out to the diameter of the vortex core. Also, from private communication with M. Konczykowski, recent work demonstrates that the material within the columnar defects is insulating.)

Columnar defects give rise to anisotropic vortex dynamics. Consequently, there should be an optimal orientation of the magnetic field for pinning by the columnar defects. As is intuitive, that direction is when the field is aligned with the columns. Considering the same argument of reduced dimensionality relative to thermal fluctuation, the pinning and consequently the critical current density are relatively temperature independent in regimes where pinning is important (Civale et al., 1991; and Konczykowski et al., 1991). The diameter of the columns induced by either Pb or Au heavy ions with energies ~ 1 GeV are on the order of 50 to 70 Å (Konczykowski et al., 1991).

Two important factors in addressing the effect of columns on vortex dynamics are the vortex-columnar interactions and vortex-vortex interaction. Additional considerations include the misalignment of vortices with the columns, ranges of misalignment for which the vortex can expend sufficient energy to align itself with the column (the depinning

angle, (Fleshler et al., 1993),also known as the accommodation angle), and effects of scattering from columns, etc.

The original papers on the Bose-glass transitions associated with the vortex-column interaction by Nelson and Vinokur (1992), and the review article by Blatter et al.(1994) only address two obvious considerations. They state that if the vortex-column interaction is large when compared to the vortex -vortex interaction, then the problem is effectively reduced to that of a single vortex mapped onto a single particle in a two-dimensional random potential, with translation invariance of the defect structure along the magnetic field direction, resulting in a static potential. This assumes that the vortex is aligned with the column. Equivalently, if the vortex-vortex interaction is greater than the vortex-column interaction, as might be the case for large magnetic fields, the problem reduces to that of a many-vortex pinning problem, which can be mapped to the vortex/2D boson analogy, in which Bose statistics are applicable with the exchange of two particles.

Motivation of Thesis

A complete explanation of the vortex-state Hall effect in type II superconductors, either an effective phenomenological or a microscopic model, is still lacking today. The challenge is that of a many-body problem, that is not in its ground state, within an inhomogeneous material, with many different issues, including vortex-vortex interactions, vortex-quasiparticle interactions, vortex-pin interactions, carrier redistributions, and thermal fluctuations.

As mentioned above, the only commonalities of the vortex-state Hall effect in type II superconductors are that the sign reversal occurs in the mixed state, when there is vortex motion, and the mean free path, l, is on the order of the high temperature coherence length, $\xi(T)$. Motivated by this latter commonality, an experiment was undertaken to examine the effects of columnar defects on the Hall conductivity. This work tests the validity of the FGLV approach by varying the amount and orientation of the columnar defects, thereby changing the defect-induced scattering time and possibly the Hall conductivity, provided that the relevant transport time for Hall conductivity is related to scattering by impurities. Systematic direct current (DC) Hall effect measurements were conducted to examine the validity of the FGLV model. Alternating current (AC) Hall effect measurements were conducted to probe the origin of the anomalous sign reversal by making dynamic observations. The results of this experimental work establish a clearer understanding of the phenomena of the vortex-state Hall effect in high-T_c superconductors: the vortex-state Hall conductivity is found to be associated with quasiparticle transport and is independent of either random or correlated static disorder. The observation of universal Hall conductivity provides a stringent criterion for future theoretical development.

Overview of Thesis

This thesis is a presentation of detailed experimental studies of the vortex-state Hall conductivity in high-temperature superconductors, including data analysis, conducted over a period of several years combined with an examination of and comparison with

relevant literature, both experimental and theoretical, and with recommended experiments to further advance the present understanding of this issue. Chapter 1 is a brief introduction of some of the issues relevant to the study of the Hall effect in type II superconductors. Chapter 2 is an overview of current theoretical and experimental developments in the study of the Hall effect in type II superconductors. Chapter 3 describes sample preparation, apparatus, and experimental setup of the DC experiments. Chapter 4 covers the DC experiment, and includes data, analyses, discussion, results, and a summary. Chapter 5 details the new experimental setup developed for AC Hall resistivity measurements, and includes data, analysis, results and discussion. Chapter 6 summarizes this work, and presents suggestions for future work.

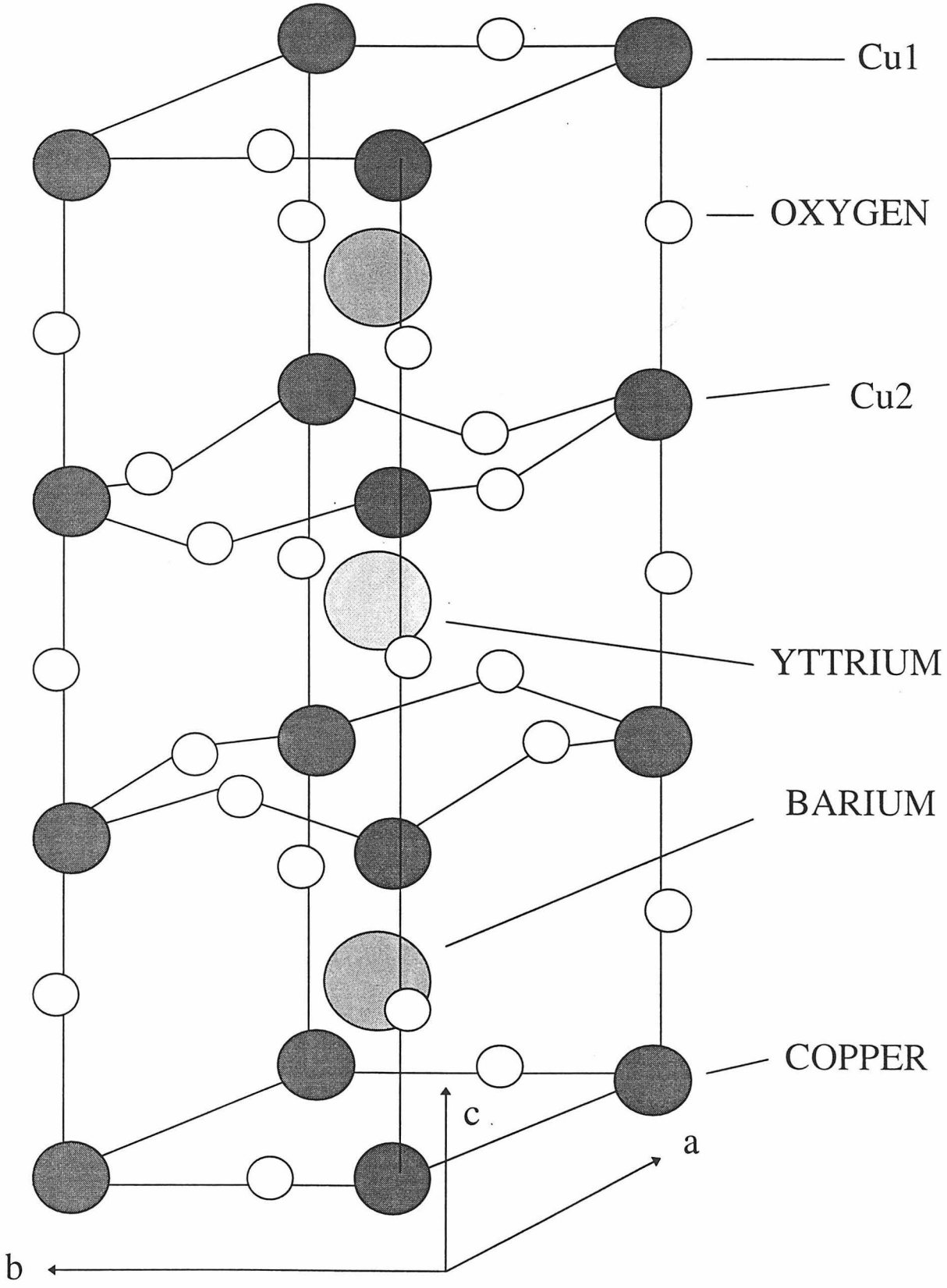

Figure 1-1 The molecular structure of orthorhombic $YBa_2Cu_3O_7$

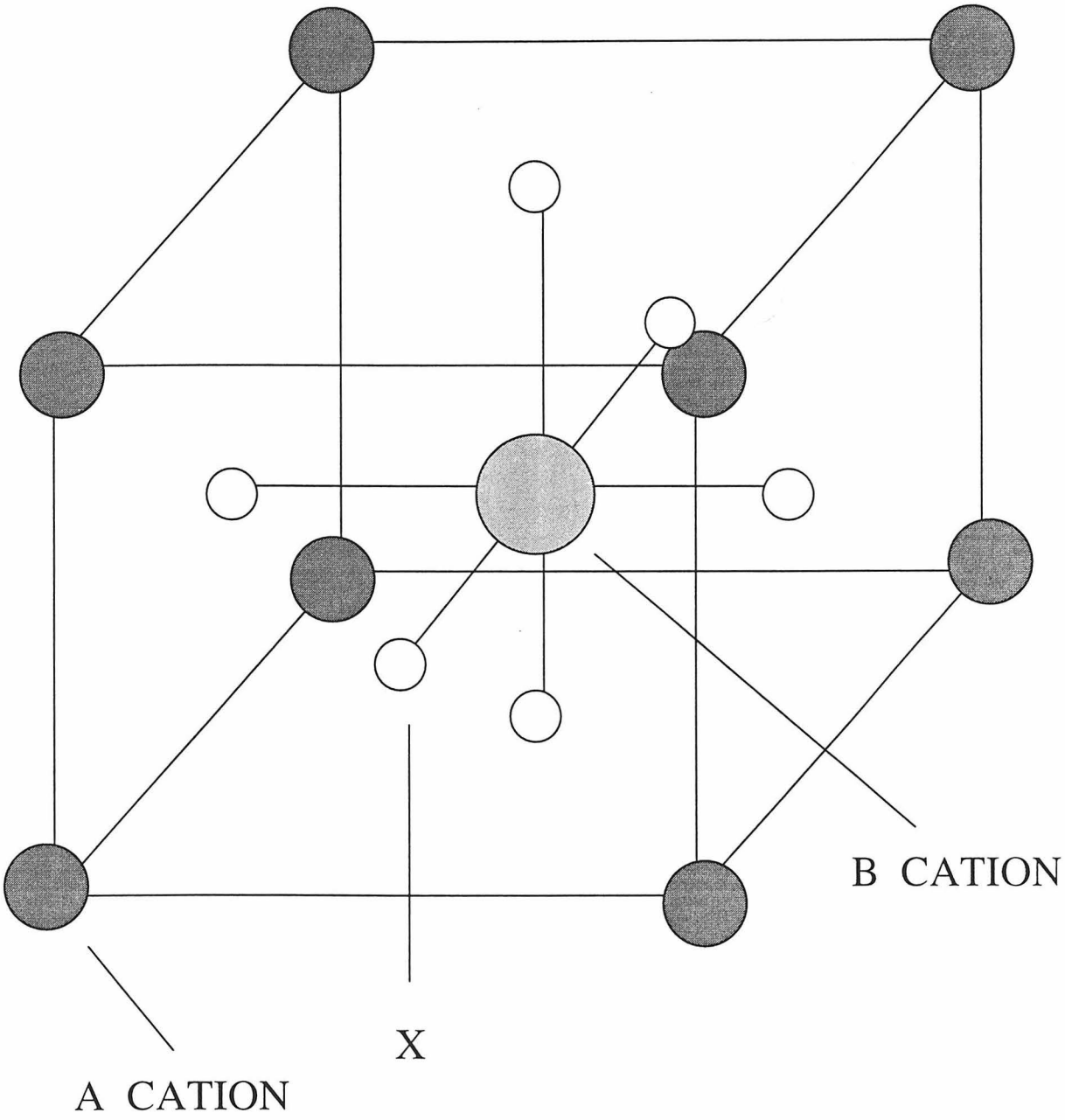

Figure 1-2 The ABX_3 perovskite structure

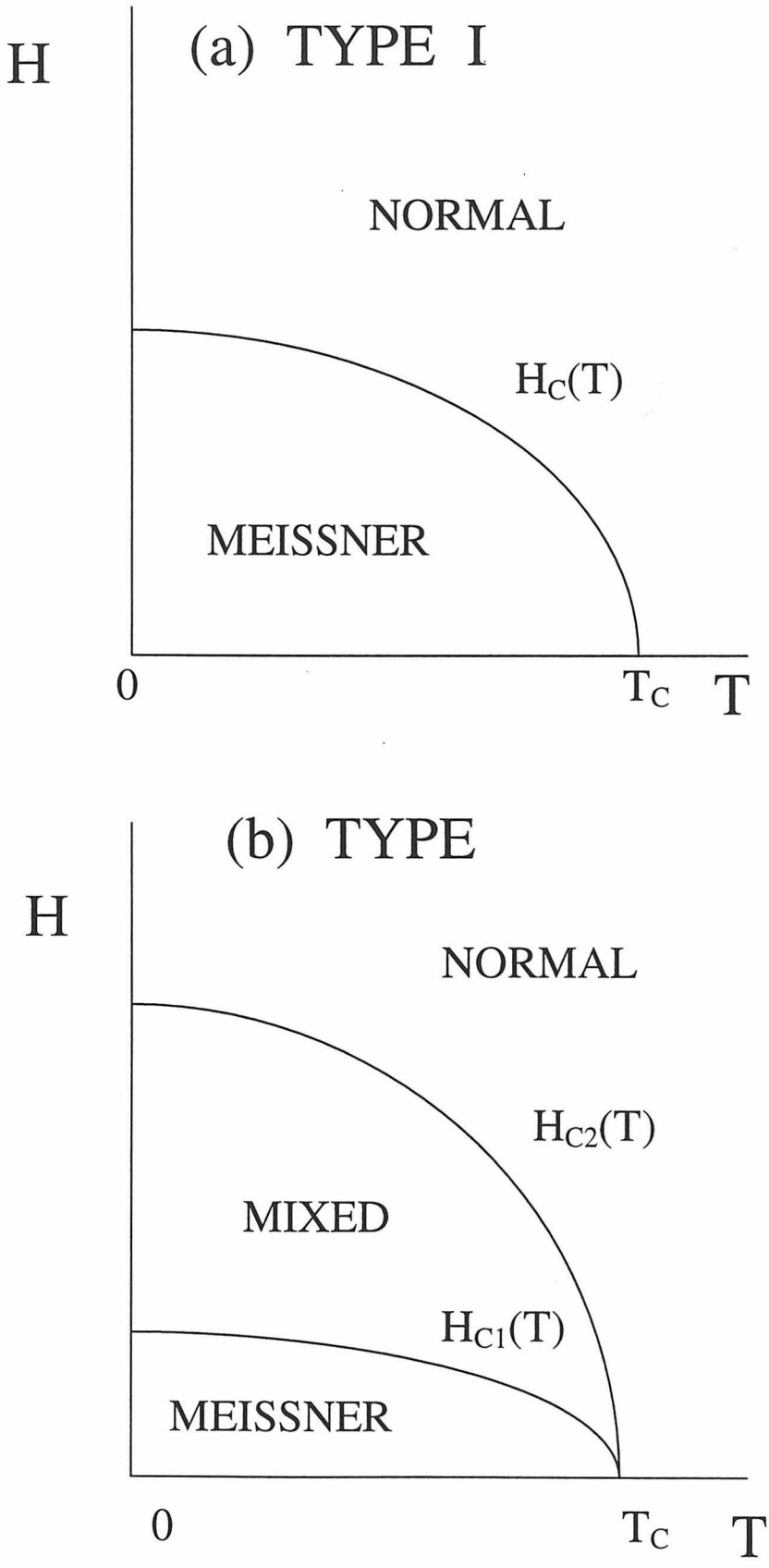

Figure 1-3 Field versus temperature phase diagram of Type I and Type II superconductors

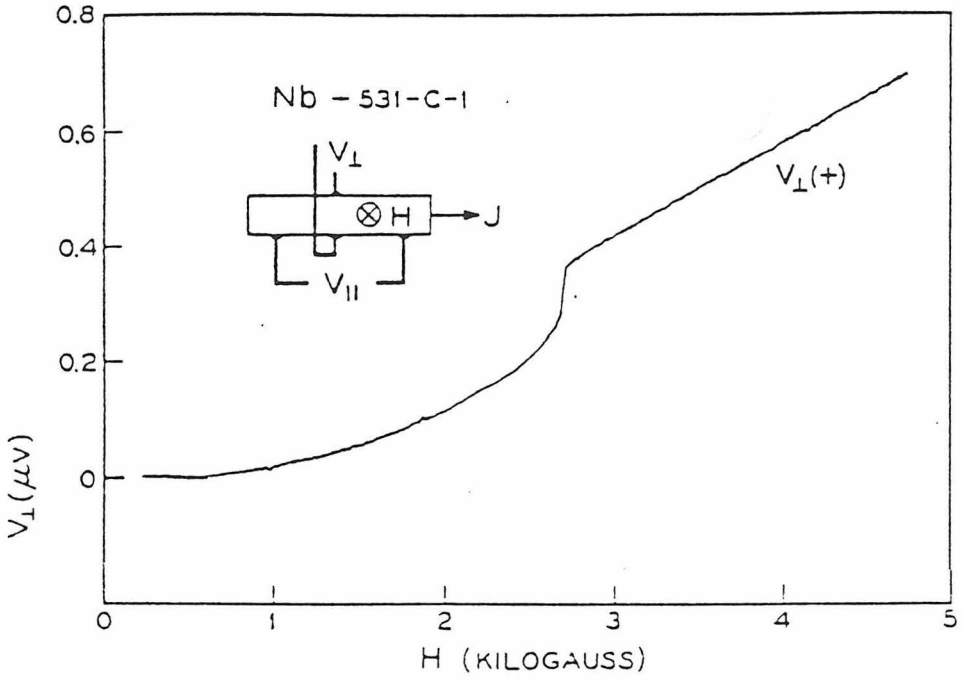

Figure 1-4 FIG. 1. of Reed et al. (1965) modified for clarity

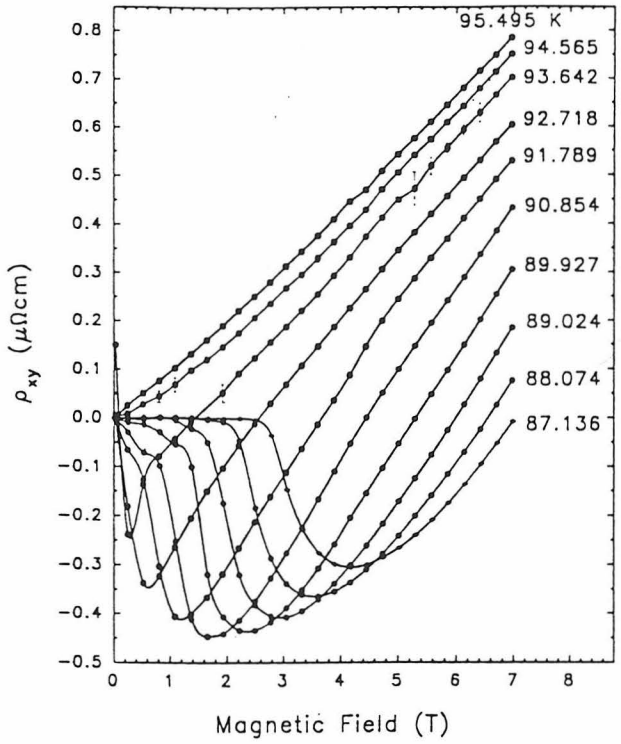

(a)

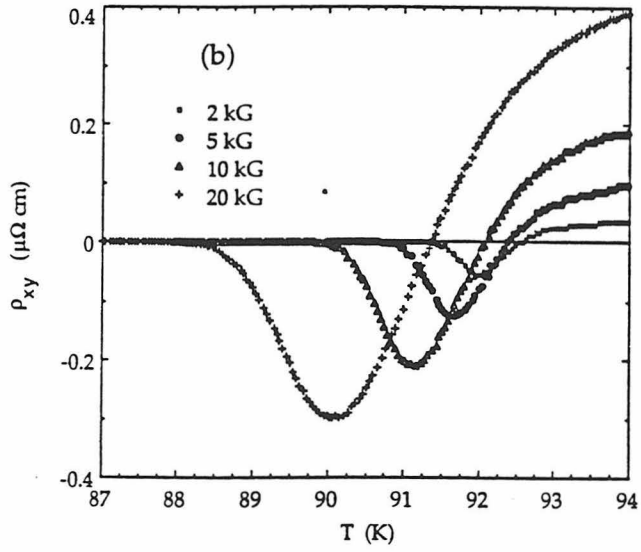

(b)

Figure 1-5 (a) FIG. 1. of Rice et al., (1995) , and (b) FIG. 1. of Hagen et al., (1993)

Chapter Two: Review of Theory and Experiments

Review of Theoretical Models that Failed

Prior to 1965, several attempts to observe the Hall effect in superconductors had failed. Two theoretical works describing the Hall effect appeared in 1964, but they were quickly challenged theoretically and unsupported by experiment. The first observation of the Hall effect in any type II superconductor was made by Reed, Fawcett, and Kim (1965), in niobium and indium. As described in chapter 1, after the report and subsequent publication of the observation of the Hall effect in niobium and indium, Bardeen and Stephen (1965) and Nozières and Vinen (1966) proposed theoretical models which appeared to explain the observatons of Reed, Fawcett and Kim (1965).

Bardeen and Stephen used a local model as a generalization of the London theory to describe the behavior of relatively clean superconductors ($l > \xi_o$). In addition to describing models for viscosity and flux flow, a prediction was made that the Hall angle would be that of the normal state for a magnetic field equal to that in the core. In the local model of Bardeen and Stephen, a vortex core of a radius on the order of the coherence length is assumed. The outside of the core is a superconducting region. The inside of the core is a region of gapless superconductivity which contains low lying quasiparticle excitations, essentially that of a normal region of radius ξ. All quasiparticles external to the core return to the ground state through scattering with the lattice. By considering the fields external to the core, continuity of the chemical potential across the core boundary

and continuity of the tangential electric field are used to define the required field within the core. This model requires an unrealistic surface charge density as a result of the discontinuity in the radial component of the electric field at the core boundary. The above considerations lead to a uniform electric field E_c in the core given by (Bardeen and Stephens, 1965)

$$e\mathbf{E}_c = (\mathbf{v}_L \times \mathbf{k})(\delta P_o/\delta r)_\xi,$$

where $\mathbf{v}_L$ is the vortex velocity relative to the lattice, $\mathbf{k}$ is the normal vector pointing along the flux line in the direction of the field, $P_o(r)$ is the momentum of the superfluid flow of a stationary vortex, and ξ is the core radius.

The above considers only the field as a result of the motion of the vortex line $\mathbf{v}_L = v_{Ly}$, normal to the transport current. The Hall fields will induce a component of the electric field within the core, E_{cy}, perpendicular to the transport current, $\mathbf{J}_t = \mathbf{J}_{tx}$. The total electric field within the core is at the Hall angle, α, such that

$$\tan\alpha = (e\tau/mc)H = \omega_c\tau,$$

where ω_c is the cyclotron frequency, and τ is the electron-lattice relaxation time. Bardeen and Stephen found the component of motion of quasiparticles within the core parallel to

the transport velocity to equal the transport velocity times the ratio of the applied magnetic field to the upper critical magnetic field,

$$v_{Lx} = (H/H_{c2})v_{Tx},$$

where v_{tx} is the transport current drift velocity. This result implied that the predicted Hall angle in mixed state should be equal to that of the Hall angle in the normal state for a field equal to the field in the core. Although the experiments by Reed, Fawcett, and Kim(1965) on clean niobium supported the model of Bardeen and Stephen, there were discrepancies in the predictions of the models when compared with measurements by Niessen and Staas(1965) on alloys.

Nozières and Vinen(1966) modeled the motion of flux lines in type II superconductors using a simplified approach by considering only systems for which $\xi << \lambda$, at low temperatures such that few quasiparticles were present, in the flux flow regime in homogenous material, and a two-dimensional geometry (such as would currently be described as motion in the ab plane of $YBa_2Cu_3O_7$, for example). As mentioned above, the intent of Nozières and Vinen was to demonstrate that the model of BS was not the only model that could explain the current "rigorously proved" results. The Nozières and Vinen model used a hydrodynamic approach which considers the more general Magnus force,

$$f = (Ne/c)(\mathbf{v}_S - \mathbf{v}_L) \times \phi,$$

where N is the density of the superconducting electrons, $\mathbf{v}_L$ is the vortex velocity, $\mathbf{v}_S$ is the superfluid velocity, and ϕ is a flux quantum. Again, Nozières and Vinen (1966) used the local model with a cylindrical vortex core of radius equal to the coherence length, containing normal electrons with a uniform velocity $\mathbf{v}_{ne}$. The electron velocity is induced by the vortex motion $\mathbf{v}_L$. The core current is purely normal on the axis of the core, and becomes superflow at $r \geq \xi$. Charge conservation outside of the vortex core requires the existence of a dipolar backflow, $\mathbf{v}_b(r)$

$$\mathbf{v}_S(r) = \mathbf{v}_{S0}(r) + \mathbf{v}_{S1}(r) + \mathbf{v}_b(r),$$

where v_{S0} is the circular velocity distribution of the vortex, v_{S1} is the velocity distribution of the applied flow, and v_b is the velocity distribution of the backflow, and,

$$\mathbf{v}_b(r) = \nabla[(\mathbf{v}_{S1} - \mathbf{v}_{ne})r(\xi^2/r^2)],$$

where $\mathbf{v}_b(r) \approx 0$ for $r \gg \xi$. The Magnus force is countered by a friction force, such that the vortex moves at a constant velocity. The force due to the lattice is effectively the Lorentz force, and the Hall angle, θ_H is

$$\tan\theta_H = (eH_{c2}/mc)\tau = \omega_{C2}\tau,$$

and is field independent below H_{C2}, and of the same sign as the normal metal. (ω_{C2} is the cyclotron frequency at the upper critical field, and τ is the electron-lattice relaxation time.)

Both the Bardeen and Stephen and the Nozières and Vinen models yielded the prediction that the Hall effect measurements in the mixed state would result in the same sign as the normal metals. The most important concern of both the Bardeen and Stephen and the Nozières and Vinen models is what the models did not predict. Neither model predicted the anomalous sign reversal of superconductors in the mixed state. As early as 1968, sign reversal of Hall effect measurements in the mixed state was reported (van Beelen et al., 1967).

Subsequent theoretical models were developed in attempts to explain the anomalous sign reversal. Hagen et al. (1990), proposed that since sign reversal occurs in both elemental and high temperature type II superconductors, it must be caused by vortex motion rather than by subtleties of the electronic band structure. By analogy with vortex motion in superfluid ^{4}He, Hagen et al. proposed that the origin of sign reversal is from a component of vortex motion in the opposite direction as the transport current. Hagen et al. further hypothesized that near vortex-solid to vortex-liquid transition, only a few quasiparticles are present, and therefore the backflowing motion dominates. At higher temperatures and fields, in the vortex-liquid phase and still below $H_{c2}(T)$, large numbers of quasiparticles are excited, and result in a positive Hall effect. That the sign reversal remains until near $H_{c2}(T)$ clearly cannot be described by this model. Furthermore, at low fields, there is only a small temperature difference between the vortex-solid to vortex-liquid transition temperature and the zero-field superconducting transition, T_c, implying

similar numbers of quasiparticles within this temperature interval, yet the sign reversal is present.

Hirsch and Marsiglio (1991) developed a two band model. The two band model expanded on the description of superconductivity in oxides having its origin in the pairing of oxygen hole carriers of $p\pi$ orbitals in a single band. The two band model included the effects associated with the Cu d_{x2-y2} and O $p\sigma$ orbitals. These additional effects consisted of a second band with a second and smaller energy gap. Assumptions included a single scattering time, τ, for both bands. The main point of the approach is the presence of paired holes and paired electrons. The paired holes have a larger gap parameter than that for the paired electrons. Consequently, at lower temperatures or fields, the electrons would depair while the holes remained paired, resulting in an electron Hall effect. Only at higher fields or temperatures would the more numerous holes depair, resulting in a hole Hall effect. Assuming equal mobility in both bands, the Hall angle would be

$$\tan\theta = CH[n_1^{eff}(T,H) - n_2^{eff}(T,H)]/ [n_1^{eff}(T,H) + n_2^{eff}(T,H)], \quad (22)$$

with C a constant in T and H, and n_i the number of particles in each band, i = 1, 2, and

$$n_i^{eff}(T,H) = \quad [H/H^i_{c2}(T)]n_i^{eff},$$

with the values of n_i^{eff} chosen to reproduce the normal state Hall coefficient at zero temperature. The main limitation of this model is that it only applies to the cuprates, yet

the anomalous sign reversal is also evident in conventional elemental type II superconductors, such as Vanadium and Niobium, and in amorphous superconductors.

Shortly after the work of Hirsch and Marsiglio, Ullah and Dorsey (1991) presented a model using the time-dependent Ginzburg-Landau (TDGL) theory to describe the effect of fluctuations (other than Gaussian) on transport properties in the mixed state. The main requirement of the model was the breaking of the particle-hole symmetry resulting in the relaxation rate having an imaginary part. Without the imaginary part, the Hall conductivity would equal itself under field reversal, requiring that the Hall conductivity be equal to zero. The unfortunate part of this model is that it was apparently developed before the authors were aware of the sign reversal, and consequently, it predicts the mixed state Hall effect to be of the same sign as that of the normal state Hall effect.

Ferrell (1992) proposed that the sign reversal in the mixed-state Hall conductivity was brought about by thermally excited quasiparticles with an opposing drift. This was essentially a backflow argument (previously used by Hagen et al. (1990), and later used by Khomskii and Freimuth (1995)). The model by Ferrell has the quasiparticles collide with the circulation superfluid far outside the vortex core, and transfer a reverse momentum to the core.

Charge redistribution was explored by Khomskii and Kusmartsev (1992). Noting the presence of two groups of carriers within a superconductor, for example, the CuO_2 planes and the CuO_2 chains, and that there is an energy gain for holes condensed in the CuO_2 planes, it would therefore be energetically favorable to redistribute hole from the reservoir to the planes. The redistribution would result in an increase in the "active"

concentration of holes, N_h, in the CuO_2 planes, even with a fixed stoichiometry. Khomskii and Kusmartsev carried out a theoretical study of the chemical potential, μ, of the system. Based on the standard weak-coupling BCS theory, the chemical potential is assumed independent in temperature, since $\mu \sim \varepsilon_F$, and $T_c << \varepsilon_F$. The resultant chemical potential is

$$\mu = \mu_o - c\,\rho'\Delta^2/\rho = \mu_o - \Delta^2/4\mu_o,$$

where $\rho(\varepsilon_F)$ is the density of states, ρ' its derivative, c is a constant ~ 0.3, $\Delta(T)$ is the temperature dependent energy gap, and μ_o is the zero temperature chemical potential. The consistency of the approach follows in that a superconductor in the normal state, when the temperature decreases, the chemical potential increases and for a superconductor in the superconducting state, the chemical potential decreases as the temperature decreases, at least initially. The net change in hole concentration is on the order of 10^{-2} per unit cell, from $(\Delta/\varepsilon_F)^2$. The model requires a much larger than the usual 5 - 10% increase in N_h to explain the observed $\Delta(0)$ value of 5 - $7.3k_BT_c$ (see Wei et al., 1997). Furthermore, high-temperature superconductors are known to be in the strong coupling limit, where conventional BCS theory fails.

Alan T. Dorsey (1992), in a study of vortex motion, considered the anomalous Hall effect using a complex order-parameter relaxation time in time-dependent Ginzburg-Landau (TDGL) equations. Dorsey noted that the particle-hole symmetry was broken both by the imaginary part of the relaxation time, and by the vortex core Hall effect. If the imaginary part of the complex relaxation time follows London equations in the

hydrodynamic limit, similar to the work of Nozières and Vinen (1966), then there is no sign reversal. If the imaginary part can be positive, based on some microscopic approach, then a sign reversal in the Hall effect is possible in this approach. However, to date, no physically feasible microscopic approach has been proposed for a positive imaginary time in the TDGL equation.

Andreev scattered quasiparticles was also used in an attempt to explain the anomalous sign reversal in the mixed state Hall effect (Hoffmann and Kümmel, 1993). (Note, that although "Andreev reflection" is used conventionally, Hoffmann and Kümmel used Andreev scattering throughout this work.) Hoffmann and Kümmel developed a microscopic explanation of the momentum transfer from the condensate to the vortex core. Half of the transfer is accounted for by Bernoulli's theorem from the electrostatic field inside the vortex core. The other half is from Andreev scattering. Andreev scattering is the conversion of incident electrons to reflected holes (and scattered Cooper pairs) in a metal at its interface with a superconductor. Converting electrons to holes requires that the Cooper pair receive momentum equivalent to that of the condensate. Equally, breaking the pairs results in an amount of momentum equal to the condensate momentum going into the quasiparticles. Sign reversal is incorporated into viscosity terms (coefficients), and the model does reproduce the main features of sign reversal. The big question remains in the viscosity terms, as the sign reversal occurs in the flux flow region, where the viscosity is negligible.

Chen and Yang (1994) modified the thermoelectric model of Freimuth, Hohn, and Galffy (1991), by incorporating the Seebeck effect. For the geometry of an applied

current density in the x-direction, the Lorentz force in the y-direction would cause the vortices to move with velocity $v_{L,y}$ in the y-direction. The resultant heat current due to the motion of the vortices would be

$$q_{v,y} = nTs_{\phi}v_{L,y},$$

n is the vortex density, s_{ϕ} is the entropy per unit length of a vortex, and $v_{L,y}$ is the vortex motion in the y-direction due to the Lorentz force. The heat current results in a temperature gradient, such that

$$q_{v,y} = -q_{n,y} = \kappa(\nabla T)_y,$$

where κ is the thermal conductivity, and $-q_{n,y}$ is the normal heat current compensation in the steady state. The electric field resultant from the thermal gradient is

$$E_y = S(\nabla T)_y,$$

where S is the Seebeck coefficient in the mixed state. Adding this to the flux flow Hall electric field yields,

$$\rho_{xy} = \rho_{xx}\tan\theta_H = \rho_{xx}\tan\theta_f + S(\nabla T)_y/j_x,$$

where θ_f is the Hall angle due to direct flux flow. Using the above expressions to determine the transport energy, and then comparing with Maki's theory (Caroli and Maki, 1967; Maki, 1971), the Hall resistivity becomes

$$\rho_{xy} = \rho_{xx}[\tan\theta_f - S\langle M\rangle L/\kappa],$$

where $\langle M\rangle$ is the equilibrium magnetization, and L is the transport coefficient of order l/ξ, with mean free path l. If the second term is larger than the first, then sign reversal will occur. Again though, in high-temperature superconductors, the sign reversal occurs in the flux-flow limit, where $\langle M\rangle \approx 0$. Combining negligible $\langle M\rangle$ with very large κ in high-temperature superconductors, it is unlikely that the Seebeck effect may be the origin of the sign reversal.

Ping Ao (1995) published a model in which the motion of vacancies in a pinned vortex lattice was examined. The conclusion that the sign reversal in the Hall effect could be explained by considering the vacancies to be antivortices, in HTS as well as niobium and vanadium missed one crucial element. The sign reversal appears in the flux-flow regime, and definitely after the vortex-solid melting transition, where there is vortex motion. In the vortex-solid, the Hall resistivity is essentially zero.

Review of Theoretical Models Presently Being Tested

In 1995, Khomskii and Freimuth extended the previous work of Khomskii and Kusmartsev (1992), by specifically considering the chemical potential in the normal core as compared with that far away from the core, and again invoked charge redistribution (Khomskii and Freimuth, 1995). In this model, the vortex cores become charged oppositely to the sign of the dominant carriers with an extra charge density δn per unit length. The charged vortex cores are screened on a length scale of λ. The consequence of the charged core is that of an extra force on a moving vortex, since the motion of the vortex results in an additional current density. Khomskii and Freimuth invoke charge neutrality and require a backflowing supercurrent which exerts forces on the vortex and can give rise to sign reversal. The resultant Hall angle,

$$\tan\alpha = \tan\alpha_n(T, B) + \tan\alpha_q(T),$$

where α_n is related to the Hall angle due to the normal core, and α_q is related to the backflow (and charged core). Although from the perspective of transport measurements, this work is equivalent to that of Feigel'man et al.(1995), the required change in carrier density within the core has the opposite sign of the work of Feigel'man et al.

Feigel'man, Geshkenbein, Larkin, and Vinokur (1995) (FGLV) developed a model where again, the vortex core has an additional carrier density, δn. The origin of the additional carrier density is from the thermodynamic potential density, and can be

expressed as a topological term in terms of the superconducting part of the total conductivity as,

$$\sigma_{xy}^{t} = -(d\Omega_{sc}/d\mu)ec/B,$$

where Ω_{sc} is the superconducting part of the thermodynamic potential density and μ is the chemical potential. FGLV use a model which includes a scattering mechanism characterized by a relaxation time, τ, in addition to the added charge density. The model considers a normal vortex core of radius $r_c \sim \xi$, where far outside the core, the carrier density is n_∞, and within the core, the carrier density is n_o, for $T \ll T_c$. For T near T_c, FGLV have multiplied n_o by a factor of g, where g is proprotional to the superfluid fraction and is a function of Δ/T and Δ is the superconducting energy gap and $g(x\rightarrow\infty)\rightarrow 1$, and $g(x\rightarrow 0) \approx x$. Therefore, where the FGLV model has the Hall conductivity as

$$\sigma_{xy} = \frac{nec}{B}\left[g\frac{(\omega_o\tau)}{1+(\omega_o\tau)^2} - \frac{\delta n}{n}\right] + \sigma_{xy}^{n}(1-g), \quad \sigma_{xy}^{n} \equiv \frac{nec}{B}\frac{(\omega_c\tau)}{1+(\omega_c\tau)^2},$$

where n is the total carrier density, $\delta n(\equiv n_o - n_\infty)$ satisfies $\delta n \ll n(\approx n_o \approx n_\infty)$, and $\delta n(T\rightarrow 0) \rightarrow$ constant and $\delta n(T\rightarrow T_c^-) \rightarrow 0$. $\omega_o = eB/[mcf(B/H_{c2})]$, where $f(B/H_{c2}) = 1$ for $B > H_{c2}$, and $f \propto B/H_{c2}$, for $B \ll H_{c2}$. $\omega_o \approx \Delta^2/\hbar\varepsilon_F$ for $B \ll H_{c2}$ in clean materials, and is the level spacing between localized states in the normal core. $\Delta = \Delta(T)$, and is the temperature

dependent superconducting energy gap, and ε_F is the Fermi energy. σ_{xy}^n is the normal state Hall conductivity, and $\omega_c \equiv eB/mc$, is the cyclotron frequency of the normal carriers. $g = g(\Delta/T)$ such that $g(x\rightarrow\infty)\rightarrow 1$, and $g(x\rightarrow 0) \approx x$. $\delta n/n \sim (\Delta/\varepsilon_F)^2$, as for an uncharged superconductor model, and, with screening taken into account, $\delta\tilde{n}/n = \text{sign}(\delta\tilde{n})(\Delta/\varepsilon_F)^2$.

FGLV take into account the Coulomb screening which suppresses the inhomogeneous charge density. As mentioned by KF, that the total charge of the vortex is zero does not change the results, since inside the screening distance (but outside the core), the charge is nonzero. KF and FGLV use different screening lengths. KF assumes screening to be complete for distances from the core axis, $R > \lambda$. FGLV assumes that complete screening occurs over a distance from the core boundary, $r_D \ll \xi_o$. After screening considerations, δn becomes $\delta\tilde{n}$, which does not depend on screening, where

$$\delta\tilde{n} = - H_c^2(T)\delta\ln(T_c-T)/4\pi\delta\mu.$$

Estimates are then made of $\delta\tilde{n}/n = \text{sign}(\delta\tilde{n})(\Delta/\varepsilon_F)^2$, and $\omega_o = \Delta^2/\hbar\varepsilon_F \ll \tau^{-1}$. The concern of the ω_o approximation is that above, FGLV state that $\omega_o \approx \Delta^2/\hbar\varepsilon_F$ at $B \ll H_{c2}$. Otherwise, $\omega_o = eB/[mcf(B/H_{c2})]$, where $f(B/H_{c2})=1$ for $B > H_{c2}$, and $f \propto B/H_{c2}$ for $B \ll H_{c2}$. Ignoring the $f(B/H_{c2})$ discrepancy, FGLV approximate the model by,

$$\sigma_{xy} \cong n_o ec\Delta^2[(\Delta\tau)^2 g - \text{sign}(\delta\tilde{n})]/B\varepsilon_F^2 + \sigma_{xy}^n(1-g).$$

Hence a sign change can occur whenever $\Delta\tau < 1$ is satisfied.

The FGLV work is supported by the microscopic analysis of van Otterlo et al.(1995). In this analysis, both hydrodynamic and vortex core contributions are considered. That the sign reversal occurs whenever the mean free path, l, is of the order of the coherence length, ξ, is interpreted in terms of the broken particle-hole symmetry in the analysis. Ultimately, the analysis focuses on the hydrodynamic contribution from which a sign change is derived if the electronic dispersion is modified such that the derivative of the density of states at the Fermi level is negative.

Anisotropic-to-Isotropic Scaling Transformation

Some of the early misconceptions for the origin of the sign reversal (e.g. Harris et al., 1993) were largely due to the complications and the lack of understanding of the effect of the mass anisotropy on σ_{xy}. The anisotropic to isotropic scaling was developed by Blatter, Geshkenbein, and Larkin(1992). The specific application to Hall conductivity was later clarified in a comment by Geshkenbein and Larkin(1994) on the work of Harris et al.(1993). Blatter et al.(1992) developed scaling rules obtained from anisotropic Ginzburg-Landau theory, and applied them to transform anisotropic results to isotropic superconductors. (The conventional approach is to start from the anisotropic Ginzburg-Landau equations and repeat the calculations as done for the isotropic equations.) The resulting general scaling rule is,

$$Q(\theta, H, T, \xi, \lambda, \varepsilon, \gamma) = s_Q \tilde{Q}(\varepsilon_\theta H, T/\varepsilon, \xi, \lambda, \gamma/\varepsilon),$$

where $s_Q = \varepsilon$ for volume, energy, temperature, and action, and $s_Q = 1/\varepsilon_\theta$ for magnetic field, where $\varepsilon_\theta = (\cos^2\theta + \varepsilon^2\sin^2\theta)^{1/2}$, for θ denoting the angle of the applied magnetic field relative to the sample c-axis, and $\varepsilon = \lambda_{ab}/\lambda_c = (m_{ab}/M_c)^{1/2}$. We note that the approximation $m_a \approx m_b = m_{ab}$ has been assumed in this discussion.

Clarifying the scaling approach of Blatter et al.(1992), Geshkenbein and Larkin showed that

$$\rho_{ik}(H) = \rho_{xy}^{c}(\tilde{H})\varepsilon_{ikl}H_l/\tilde{H},$$

where H is the applied magnetic field, $\tilde{H} = (H_z^2 + H_t^2\varepsilon^2)^{1/2}$ is the scaled field, H_z and H_t are the c-axis and ab-plane magnetic field components, respectively, and $\varepsilon = \lambda_{ab}/\lambda_c$ is the anisotropy ratio. That the above scaling relation is temperature independent, and the scaling for temperature is a simple scalar (a numerical constant), the scaling equation versus H can be directly brought over to versus H and versus T,

$$\rho_{ik}(H, T) = \rho_{xy}^{c}(\tilde{H}, T)\varepsilon_{ikl}H_l/\tilde{H}.$$

Noting that for θ denoting the angle of the applied magnetic field relative to the z-direction, $\tilde{H} = H(\cos^2\theta + \varepsilon^2\sin^2\theta)^{1/2} = \varepsilon_\theta H$, where $\varepsilon_\theta = (\cos^2\theta + \varepsilon^2\sin^2\theta)^{1/2}$, and for i = x, k = y, and l = z, with $H_z = H\cos\theta$, this equation can be written explicitly in terms of θ,

$$\rho_{xy}(\theta, H, T)[1 + \varepsilon^2\tan^2\theta]^{1/2} = \rho_{xy}(\theta=0^\circ, \varepsilon_\theta H, T).$$

Consequently, for a fixed T and at various angles, θ, of the applied magnetic field, the $\rho_{xy}(\theta, H)$ should all transform upon scaling into a scaled curve, $\widetilde{\rho}_{xy}(\widetilde{H})$.

Vinokur, Geshkenbein, Feigel'man and Blatter (1993) developed a scaling relation between the Hall resistivity and the longitudinal resistivity, $\rho_{xy} \propto (\rho_{xx})^2$, for isotropic superconductors, which was nothing more than a first principles derivation of the Hall conductivity. $\sigma_{xy} = \rho_{xy}/(\rho_{xx}^2 + \rho_{xy}^2) \approx \rho_{xy}/\rho_{xx}^2$., for $\rho_{xy} \ll \rho_{xx}$. The important result of the latter work is the phenomenological argument that random pinning sites renormalize the friction coefficient and causes no change in the Hall conductivity. It was further claimed that this result applies to FF, TAFF and creep behavior. The assumption made is that the pinning force is the gradient of a random potential, determined by the positions of the vortices relative to the pins, and is invariant with respect to the reversal of the magnetic field. The only vectorial quantity that is independent of the sign of the magnetic field and characterizes vortex motion is the velocity, **v**, of the vortices. Therefore, only the friction term is affected. The authors considered only the issue of random potentials and did not address the possible effects of correlated disorder.

Review of Experiments

The sign reversal of the Hall effect in the mixed state is observed in many different materials of type II superconductors. This sign reversal is well known to occur in the high transition temperature superconductors, and even in some conventional type II superconductors. That this phenomenon has remained unresolved for so long (nearly 29 years at this writing), is astounding. That it appears in materials properly characterized by BCS theory, as well as those yet to be properly characterized by a theory makes its understanding more challenging.

There are only a few commonalities of the occurrence of the sign reversal among the various superconductors. The obvious commonalities are that the superconductors are all type II, and that in every case of sign reversal, it occurs in the mixed state. This latter observation is simply by definition, as the correct sign for the Hall effect is assumed to be that of the superconducting material in the normal state. In highly anisotropic materials, the mixed state often shows two signs of the Hall effect (e.g., Hagen et al., 1991; Hagen et al., 1993). Possibly most important is that for most of the cases where the sign reversal in the Hall effect occurs, the mean free path is comparable to the GL coherence length at a finite temperature. However, the observed sign reversal in the mixed state Hall effect of $Pb_{1-x}In_x$ ($x<=0.35$) where the mean free path $\sim 0.01\xi_o$ is of additional concern, as $Pb_{1-x}In_x$ is a conventional low temperature type II superconductor (Weijsenfeld, 1968). There is one other key commonality among the superconductors showing sign reversal in the Hall effect, the sign reversal only occurs when the vortices are moving. There is no indication

of sign reversal for stationary vortices. Sign reversal in the mixed state Hall effect eventually disappears at high applied magnetic fields, $H \rightarrow H_{c2}$, and at high temperatures, $T \rightarrow T_{c2}$.

This section will review the experimental studies relevant to the following areas. The earliest report of sign reversal in the mixed state Hall effect occurred in 1967 (van Beelen et al., 1967; Weijsenfeld, 1967). The expanse of type II materials showing this effect will be reviewed, and commonalities will be presented in more detail. Finally, the experimental studies of correlated defects, their anisotropic effects and the debate over their effects on Hall conductivity will be discussed. The information in this section will be presented mostly in a logical order, rather than chronological. First we will establish the flux flow regime, by looking at work studying longitudinal resistivity and other mechanisms. Within this study of flux flow regime, we will also observe how twin boundaries and columnar defects affect the shape of the longitudinal resistivity curve at its lower temperatures. We will then consider the anisotropy effects induced by the correlated defects. In particular, we will comment on the effect of the correlated disorder on the vortex-solid to vortex-liquid phase transition line, which has important effects on reducing the flux-flow resistivity for a given temperature. Then, we will briefly review the wide range of materials in which the sign reversal of the mixed state Hall effect occur. The relevance of the correlated defects to the vortex-state Hall resistivity will also be discussed.

The first observation of the Hall effect in superconductors was make in 1965 by Reed, Fawcett, and Kim (Reed et al., 1965). Their work was marked by seeing a

nonlinear region (versus applied magnetic field) in the mixed state, followed by a linear region in the normal state. They also noted a temperature and current dependence on the magnitude of the Hall voltage as compared with the longitudinal voltage measured. The sign reversal of the mixed state Hall effect was observed two years later, first in Niobium (van Beelen et al., 1967), and later in studies of Vanadium and of different purities (Usui et al., 1968, and Usui et al, 1969). The first observation in high-temperature superconductors was in 1988 by Galffy and Zirngiebl (Galffy and Zirngiebl, 1988) in $YBa_2Cu_3O_7$ and $Bi_2Sr_2CaCu_2O_8$. Iye et al. reported on sign reversal in $ErBa_2Cu_3O_7$ and $Bi_2Sr_2CaCu_2O_{8+y}$ thin films (Iye et al., 1989). In addition to the appearance of sign reversal in $HoBa_2Cu_3O_{7-x}$ (González, et al., 1991), in January 1993, Hagen et al., on surveying the literature, noted that sign reversal occurred in the mixed state of 13 other type II superconductors (Hagen et al., 1993). In May 1994, Smith et al., observed sign reversal in the mixed state Hall effect of amorphous Mo_3Si (Smith et al., 1994). The summation of these samples includes elemental, hole-conducting cuprates, electron-conducting cuprates, and to amorphous Mo_3Si materials. Colino et al., reported that sign reversal occurs in a-axis films (Colino et al., 1994). With sign reversal appearing in so many different materials, it appears that sign reversal in the mixed state Hall effect is an intrinsic property of the mixed state. Yet, even of the materials mentioned above as having mixed-state sign reversal, among these materials, they do not always have a sign reversal in the mixed stated.

Hagen et al. (1993) noted a commonality among most of the type II superconductors showing the sign reversal, that the mean free path is on the order of the

GL coherence length, $\xi(T)$. In this work, Hagen et al., also clearly showed that with increasing temperature (or field, (Hagen et al., 1990)), the onset of the Hall resistivity was at or after the onset of longitudinal resistivity. When comparing with above issues of vortex-solid to vortex-liquid phase transition and flux flow, the sign reversal clearly occurs in the flux-flow regime of the mixed state. This is of importance when pinning effects are considered. Wang and Ting (1991) attribute the sign reversal to strong pinning. That the sign reversal occurs in the flux flow regime implies that pinning has little effect.

The effect of quasiparticles on the sign reversal has been considered by various authors. The present assumption is that quasiparticles participate in such a manner that results in a positive Hall current, $\propto H$. The negative sign anomaly is therefore considered to result from vortex motion. Harris et al. (1995), consider d-wave or anisotropic s-wave pairing. For $T > 70K$, these pairings would result in a large quasiparticle population outside the core (Harris et al., 1995). Harris et al. notes that zero field microwave experiments suggests a sharp increase in quasiparticle lifetime below T_c. Harris et al. then assume that vortices act as "impurities" in a sea of quasiparticles. Harris et al., subsequently consider that instead of changes in quasiparticle population, that the two competing terms grow in opposite ways. With increasing fields, the normal (positive) term grows, and with small fields, the vortex motion (negative) term dominates. Harris et al., report that the vortex motion term has a functional form of

$$\sigma_{xy}^{f} = -2.1 \times 10^{7}(T/T_c)/B \ (\Omega m)^{-1},$$

where

$$\sigma_{xy} = \sigma_{xy}^{n} + \sigma_{xy}^{f},$$

where σ_{xy} is the total Hall conductivity, σ_{xy}^{n} is the contribution to the Hall conductivity from the quasiparticles, and σ_{xy}^{f} is the contribution to the Hall conductivity from the motion of vortices.

Almasan, et al.(1995) developed a different temperature dependence of the vortex motion term. Given

$$\sigma_{xy} = C_1 / B + C_2 B.$$

The vortex motion term is C_1/B, where,

$$C_1 = A(1-T/T_c)^{\alpha}., \alpha = 2.3 +- 0.07 \text{ for } YBa_2Cu_3O_{6.84},$$

and $A < 0$ is a constant.

Nuss et al.(1991) use coherent time-domain spectroscopy in the frequency range from 500 GHz to 2.5 THz to study the real and imaginary parts of the conductivity in YBCO thin films. A peak in the real part of the conductivity was observed using the coherent time-domain spectroscopy, but was not observed using nuclear magnetic resonance. The implication of the latter is that the peak's origin is caused by a 'strongly decreasing inelastic-scattering rate below T_c' rather than coherence factors.

Using microwave surface resistance data of a single crystal $YBa_2Cu_3O_7$, Bonn et al.(1992; 1993; and 1994) estimated a large drop in the quasiparticle scattering rate just below T_c. They attributed the "much faster than linear" fall in $1/\tau$ to a suppression of the strong inelastic scattering process responsible for the linear dc resistivity temperature dependence above T_c (Bonn et al., 1992). They further suggested that the existence of a gap below T_c for the quasiparticles is responsible for scattering above T_c.

Krishana, Harris, and Ong (1995) measured the thermal conductivity in $YBa_2Cu_3O_7$ single crystals to determine the quasiparticle mean free path. The experiment was an asymmetric scattering experiment with no induced vortex motion. The approach used the handedness of the superfluid circulation around a flux line to yield asymmetric scattering. For a given current, there will be a preferred direction of scattering. This work again used the assumption that vortices reduce the quasiparticle lifetime. Fitting the data using a parameter representing the quasiparticle lifetime, the authors obtained a large increase of the mean free path in the Meissner state from about 90 Å at 92K to 2500 Å at 15K, and a Fermi velocity of $v_F = 2 \times 10^5$ m/s (Krishana et al., 1995). (A recent report by Numssen et al.(1996) claims similar mean free path magnitude and temperature dependence derived from microwave surface impedance measurements.) Again, d-wave pairing was considered, with the conclusions that the dominant scattering mechanism above T_c is electronic, and that again, there may be a gap below T_c associated with the excitations above T_c.

The only Hall effect experiments at frequencies other than DC have been those done in the terahertz range. Parks et al.(1994) conducted phase-sensitive spectroscopy to

study the complex resistivity tensor of YBCO films in the mixed state. The studies were conducted in the frequency range of 100 to 500 GHz. Transmission coefficients were determined using parallel, t_{xx}, and crossed, t_{xy}, polarizers. From the transmission coefficients, the real and imaginary parts of ρ_{xx} and ρ_{xy} were determined. Using a two fluid model, and describing the quasiparticle contribution by a single quasiparticle scattering time, τ_{qp}, Parks et al. calculated the scattering time to reach $\tau_{qp} \sim 0.7$ ps for $T \leq 40$ K. This value was an order of magnitude lower that that determined by Bonn et al., which was attributed by Parks et al. to an increase in the scattering rate by the disorder present in the films. Additionally it was observed, that based on the behavior of ρ_{xy} (no data shown), the Magnus force parameter was frequency dependent and complex at all temperatures and frequencies in the studied range.

Spielman et al. (1994), the same group as Parks et al., simultaneously published work in which the complex conductivity tensor was derived in the frequency range of 150 to 800 GHz. Using coherent time-domain spectroscopy, the complex transmission tensor was measured in the temperature range of 10 to 200K. Again YBCO thin films were used. Near 40K, the real and imaginary parts of σ_{xy} were found to exceed the normal state values by an order of magnitude. On the other hand, in this frequency range, the imaginary part of the Hall conductivity near T_c ($T_c \approx 84$K) was observed to be about 1% of the DC Hall conductivity magnitude measured at 100K. The real part of the Hall conductivity was found to be frequency dependent and vary from about 2% to 4% of the magnitude of the DC Hall conductivity measured at 100K. It is interesting to note that although both the real and imaginary parts of the transmission ratio t_{xy}/t_{xx} undergo sign

changes as a function of temperature, they undergo the sign changes at different temperatures. In fact, when the imaginary part is positive and at a maximum, the real part is negative and at a minimum. Similarly, when the imaginary part is negative and at a minimum, the real part is positive and at a local maximum. The difference in temperature between the minimums is approximately 10 K.

The work of Kwok et al. (1992), Fleshler et al. (1993), and Legris et al. (1993) give clear indication of the location of flux-flow regime of the longitudinal resistivity versus temperature curves. In addition, these works demonstrate the effect of correlated defects on the longitudinal resistivity. Fleshler et al. (1993) demonstrate that flux flow perpendicular to the twin boundaries is characterized by a "shoulder" in the resistivity, and that in a detwinned sample, it is characterized by a "kink." Most importantly, Fleshler et al.'s results demonstrate that the presence of twin boundary pinning can significantly suppress the flux-flow resistivity for the applied magnetic field aligned with the sample c-axis. The significant reduction in flux-flow resistivity for **H** // **c** is the result of increased vortex-solid to vortex-liquid temperatures due to the presence of twin planes. This reduced flux-flow resistivity is not to be mistaken as an indication of pinning at the given temperatures and fields, because the current-voltage characteristics in the flux-flow region are strictly Ohmic.

The effect of correlated defects on the Hall conductivity remains unresolved in the literature. According to Vinokur et al. (1993), random defects should not have an effect on the Hall conductivity, provided that their presence does not change either the position of the vortex-solid to vortex-liquid phase transition line or the transport scattering time, τ.

Correlated defects meet neither the criteria of randomness nor that of invariant vortex phase transition temperatures. Correlated defects, such as columnar defects, are random in two dimensions, but correlated in the third dimension. As discussed above, correlated (columnar) defects change the position of the vortex-solid to vortex-liquid phase transition line (Reed et al., 1996). Also, as mentioned above, the correlated defects do cause apparent changes in the Hall and longitudinal resistivities. A vortex 'locked-in state' in irradiated (inducing columnar defects) $YBa_2Cu_3O_7$ thin films is even observed at ~ 10 GHz using cavity microwave absorption techniques (Lofland et al., 1995; and Lofland et al., 1996).

The question is, do the correlated defects affect the Hall conductivity?. Samoilov (1994) reported that there was no observed change in the Hall conductivity for a $YBa_2Cu_3O_7$ single crystal and a $Tl_2Ba_2CaCu_2O_8$ thin film before and after heavy-ion irradiation, for magnetic fields aligned with the columnar defects. In fact, as seen in the copy of the Hall conductivity data for the $YBa_2Cu_3O_7$ single crystal and the $Tl_2Ba_2CaCu_2O_8$ thin film, shown in figure 2-1(a) (Samoilov et al., 1995, figure 3), where the before irradiation is shown as open circles, and after irradiation is shown as solid symbols, the after irradiation data has a more steep slope than the before irradiation data. Even if the data is plotted in reduced temperature, T/T_c, the slope of the before and after irradiation data do not change. Further, at low temperatures, near the loss of resolution of the Hall conductivity, particularly when a high magnetic field was applied, there appeared to be a departure in the low-temperature Hall conductivity between the before and after heavy-ion irradiation curves. Therefore, the conclusion of defect independence is an

overinterpretation of the presented data by Samoilov et al. One important experimental detail about Samoilov's work is that the same samples were used for both before and after irradiation comparisons. The limitation of the work is that only measurements with the magnetic field parallel to the c-axis columnar defects were made. (Note: the inset of Samoilov et al. (1995) figure 3 is a log $|\rho_{xy}|$ vs log $|\rho_{xx}|$ plot for the thalium sample measured at 2 Tesla, where the open squares are before irradiation data, and the solid circles are after irradiation data.)

Kang et al. (1996), published a duplicate study in which two $YBa_2Cu_3O_7$ single crystals were used, one as grown, and one with the same amount of heavy-ion irradiation (although at a lower energy) as that of Samoilov's sample. Contrary to the claims of Samoilov et al. (1996), dependence of the Hall conductivity on defects was claimed by Kang et al. (1996), as shown in figure 2-1(b) (Kang et al., 1996, figure 4), where the before irradiation is shown as open circles, and after irradiation is shown as solid symbols, and suggested the necessity of adding a pinning term to the theoretical work of Vinokur et al. (1993). The work by Kang et al. was subsequently commented by Smith and Lobb and by Samoilov (comments, to appear in Physical Review Letters, 1997). Smith and Lobb (1997) and Samoilov (1997) pointed out that the departure between the as-grown and heavy-ion irradiated Hall conductivity curves, reported by Kang et al. (1996), occurred when both ρ_{xy} and ρ_{xx} are very small, yielding great uncertainties in the quantitative details of $\sigma_{xy}(\equiv \rho_{xy}/(\rho_{xx}^2 + \rho_{xy}^2))$. Smith and Lobb further point out in their comment that the temperatures where Kang et al. suggested a pinning-dependent σ_{xy} are in fact in the ohmic regime, where pinning is irrelevant. The work in this thesis resolves this controversy.

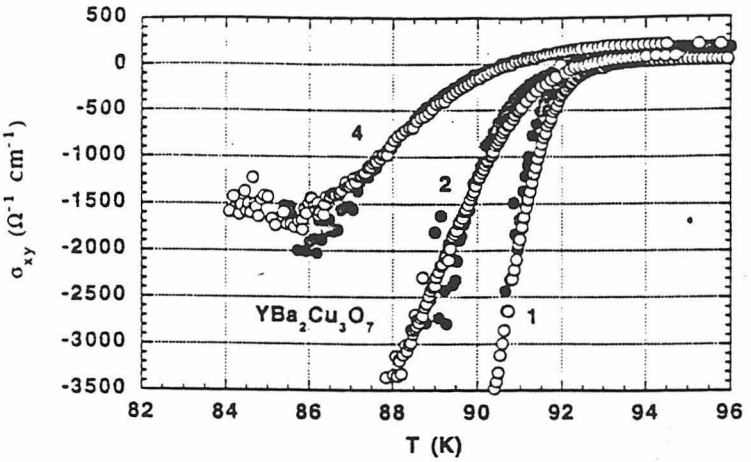

(a)

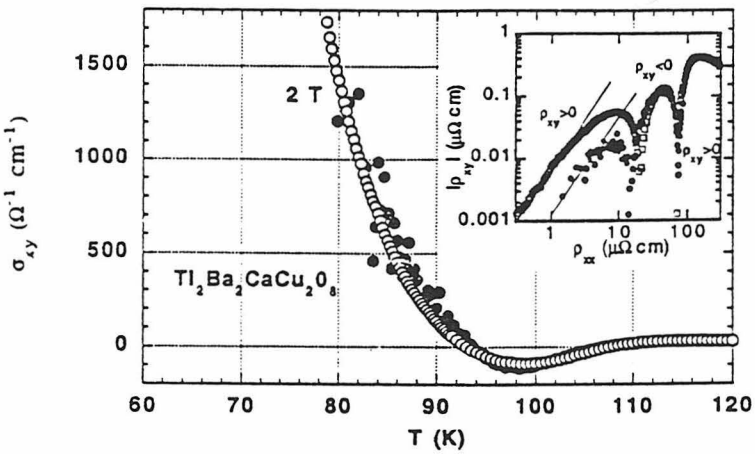

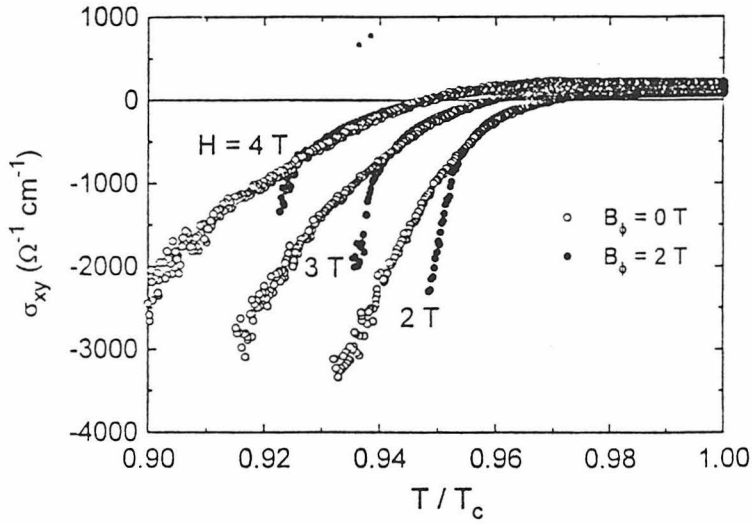

(b)

Figure 2-1 (a) FIG. 3. of Samoilov et al., (1995) , and (b) FIG. 4. of Kang et al., (1996)

Chapter Three: DC Experiment

Apparatus

The DC Hall effect experiments were performed using a four-point method with modified van der Pauw corrections. A functional block diagram of the DC Hall measurement system is shown in figure 3-1. The voltage was measured using a Keithley 182 Sensitive Digital Voltmeter via coaxial cables from the $YBa_2Cu_3O_7$ single crystals to the Model 7168 nV Scanner Card in the Keithley 705 Scanner, and from the Model 7168 nV Scanner Card via triaxial cables to the Keithley 182 Sensitive Digital Voltmeter. The current was supplied to the sample by the Keithley 220 Programmable Current Source via the General Purpose switch card in the Keithley 220 Programmable Scanner and via coaxial cables from the Model 7056 General Purpose Scanner Plug-In Card to the sample in the probe. The temperature was controlled using a Lakeshore DRC-93C temperature controller and two different types of temperature sensors, a CGR-1-2000 carbon glass resistor, and a CS 501 capacitance sensor for temperature control in the presence of high magnetic fields.. The system employed two heaters, by Minco Products, Inc., a HK5537R26.1L12D heater in direct contact with the sample holder for fine temperature control, and the HK5207R42.1L36A heater as an outer can heater for coarse temperature control. Cooling power was provided by liquid helium in an inner dewar and separated from the samples by thermal insulating vacuum jackets and low pressure exchange gas.

Hall and longitudinal resistivity measurements were conducted versus temperature using the carbon-glass temperature sensor as the temperature measuring and controlling sensor. Consequently, the temperature measured has offsets from the actual temperature due to the positive magnetoresistance of the carbon-glass temperature sensor. Even so, the greatest offset was not more than 0.4K, and the offset was reproducibly fixed for a given applied magnetic field strength and orientation of the temperature sensor holder (and consequently the temperature sensor) in the field. Therefore, the temperatures measured in high fields can be calibrated.

Hall and longitudinal resistivity measurements were conducted versus field in the following manner. First, the carbon-glass temperature sensor was used to set the temperature in zero field. Then, while still in zero field, the capacitance sensor was made the controlling sensor. After stabilizing, and still monitoring the carbon-glass sensor, the capacitance sensor continued as the controlling temperature sensor because it is not affected by the applied magnetic field, and the field sweeps (in the direction of increasing fields) were performed.

The magnetic field used during measurements is provided by a Cryomagnetics niobium alloy wire superconducting magnet with maximum field of 9 Tesla. Field stability is achieved via isolation of superconducting magnet in the persistent current mode. The theoretical decay time of the magnetic field is effectively infinite when compared to that of experiment duration time. The actual stability of the magnetic field approaches the theoretical limit, as long as the liquid helium level is maintained above the minimum required level.

The measurement data was acquired using an IBM PS/2 Model 30 286 computer with IEEE-488 (GPIB) card and 80286 16-bit processor. Acquisition and control programs were mostly written by D. S. Reed, as specified in his thesis (D. S. Reed, 1995).

Measurement Probes

The probes used in the experiments conducted in support of this thesis are the AC transport probe and the Ball Probe. Detailed diagrams and descriptions of these probes are available in the thesis by D. S. Reed (1995). The applications of these probes are similar to that of Reed (1995) and Jiang (1995).

Samples

Five fully oxygenated $YBa_2Cu_3O_7$ twinned single crystals were used in this experiment. The samples were obtained from F. Holtzberg, IBM. The samples had varying twin densities from lightly twinned to heavily twinned, when viewed with a microscope. The variances in twin density do not appear to have made any noticeable difference in the measured data. Prior to irradiation and transport measurements, the samples were characterized using AC susceptibility techniques, and all samples were found to be 100% superconducting in zero-field at low temperatures.

The samples length and width dimensions each were approximately 0.5 - 0.8 mm. Identifying the samples as one through five, the thicknesses and conditions off irradiation

are summarized in table 3-1, where the matching field, B_ϕ, is defined as the magnetic field at which the flux lines have the same areal density as the induced columnar defects, when the field is aligned with the columnar defects.

Sample Preparation

Utensils for sample handling were washed with soap and deionized water, and rinsed with deionized water. The utensils were then rinsed in pure acetone. After rinsing, the utensils were immersed in pure acetone and placed in an ultrasonic cleaner for approximately 5 minutes. Then the utensils were rinsed in pure ethanol followed by being immersed in pure ethanol and again placed in an ultrasonic cleaner for approximately 5 minutes.

Early sample preparation included an etching procedure using a 1% bromine in pure ethanol mixture. Single crystals were etched for 5 - 10 minutes (films at 1/2% for 5 - 30 seconds), to remove nonstoichiometric surface layers prior to sputtering (or evaporation) of gold, followed immediately by many pure ethanol rinses. It was observed that even for high quality as grown single crystals, long-time bromine etch would eventually cause the crystal surface to become rough by creating what appeared to be grooves of several microns thick. The grooves were most likely due to different etching rates along the twin boundaries and within the twin planes. Consequently, this approach was not undertaken in this study. An alternative procedure was subsequently developed.

It was observed that after first rinsing with pure ethanol, then pure acetone, then pure ethanol, a 30 second rinse with room temperature pure toluene or pure xylene would remove any grease. More importantly, it was observed that the contact resistance, after sputtering, was comparable to that of the previous samples that had received the bromine etch and sputtering. (The contact resistance was also comparable to samples that had received bromine etch and with gold contacts made with evaporation and subsequent oxygen annealing. The sputtering process clearly has the advantage of creating better cohesion of gold to the sample surface, even without removing the nonstoichiometric surface layer.)

Prior to sputtering gold contacts on the single crystals, masks were prepared to limit the area of exposure of the single crystal to the gold. Masks of pure gold were fashioned to result in only a small portion of the four corners of the single crystal (or film) being exposed to gold during sputtering.

An Edwards sputtering system was used. Sputtering occurred in argon gas at a pressure of 1 mTorr. A 3 inch gold (.9995 pure) target of approximate thickness 1.6 mm. was placed approximately 50 cm from the sample. Target power was set at approximately 20 W, yielding a current of approximately 430 mA. Gold thickness sputtered on the sample was approximately 120 nm. It should be noted that only gold and silver are nonreactive with $YBa_2Cu_3O_7$ over a long period of time, and therefore are the only choices of materials from which to make contacts.

After gold was sputtered, four of the five samples were sent to GANIL in France for heavy-ion irradiation. 5.9 GeV lead ions were used to create columnar tracks in the

single crystals. At this energy, column lengths of 30 angstroms are typical (39 keV/nm) and diameters of about 70 angstroms (Civale et al., 1991, Konczykowski et al., 1991, Tombrello, 1995). The thicknesses of the samples were chosen to meet this criteria. Alignment of the columns with desired orientation is to within ± 1°. After heavy-ion irradiation, zero field transition widths remained ~ 0.2K and T_c for the irradiated samples are within 0.2K of the as grown sample's T_c.

Electrical contact from the sample to the sample probe was made using indium pressed on the gold contacts, and pure (.9999) copper wire pressed in the indium and soldered to the probe contact. The indium was cleaned by rinsing in pure ethanol. (The indium had a purity of .999, and was grease free. An alternate approach for cleaning was to immerse the indium wire in pure acetone and place it in an ultrasonic cleaner for about 30 seconds, then rinse in pure ethanol, immerse pure ethanol, and place again in the ultrasonic cleaner for about 30 seconds. If the indium wire was placed in the ultrasonic cleaner for much more than a minute, it would begin to break apart.) The pressing of the indium on the gold sample contact was done using the cleaned plastic handle (from a scalpel) fashioned to a point.

Sample - Magnetic Field Orientation

A diagram of the applied magnetic field and sample orientation is shown in figure 3-2. The magnetic field was fixed in the vertical direction, parallel to the z-axis of the diagram, and the sample rotated about an axis perpendicular to the c-axis, parallel to the

x-axis of the diagram. The angle between the magnetic field direction and the sample c-axis is labeled as θ. The rotation of the sample probe allowed the magnetic field to be applied to the sample at various orientations, from - 10° to 92° relative to the samples' c-axes.

Modified van der Pauw Resistivity Measurement Technique

van der Pauw has written two papers referencing the determination of resistivity. In the first paper, (van der Pauw, 1958), van der Pauw discusses the measurement of specific resistivity and Hall effect in flat samples (disks) of arbitrary shapes. Regarding the applicability of the van der Pauw approach to inhomogeneous materials, such as type II superconductors in the vortex state, van der Pauw makes no mention. van der Pauw does write, "specific resistivity and the Hall effect of a flat sample of arbitrary shape can be measured without knowing the current pattern if the following conditions are fulfilled: (van der Pauw, 1958):

a. The contacts are at the circumference of the sample.
b. The contacts are sufficiently small.
c. The sample is homogeneous in thickness.
d. The surface of the sample is singly connected, i.e., the sample does not have isolated holes".

As stated by van der Pauw, the only homogeneity requirements is that the sample be of homogeneous thickness and that the surface be singly connected. Although homogeneity

is not specifically mentioned, there is an assumption of required homogeneity, since van der Pauw considers materials with specific resistivity. What isn't clear is the required homogeneity, as the van der Pauw corrections are essentially geometric. That a superconductor has a constant ratio of resistances R_{xx}/R_{yy} from well above T_c to below T_c in the vortex-state through the flux flow regime implies that the "inhomogeneity" caused by the presence of vortices should not affect the van der Pauw corrections. (In the TAFF regime, there is no longer a linear current-voltage response and the van der Pauw corrections are not applicable.) That samples with columnar defects (verified for samples with a matching field up to 2 Tesla, corresponding to about a 1% inhomogeneity) also have a constant ratio R_{xx}/R_{yy} from well above T_c to below T_c through the flux flow regime suggests that the 1% inhomogeneity caused by the presence of columnar defects should not affect the van der Pauw corrections.

For the measurements reported in this thesis, a van der Pauw resistivity measurement technique was used to determine the longitudinal resistivity (van der Pauw, 1958), and a modified van der Pauw resistivity measurement technique (van der Pauw, 1961; Konczykowski, 1994) was used to determine the Hall resistivity. The van der Pauw approach allows longitudinal and Hall resistivity measurements to be made by placing four contacts on the perimeter of the sample. The contacts were as small as possible, to reduce additional corrections, and typically one contact was placed in each corner. One sample, number five (45°, 0.5T), had an irregular shape. Four contacts were again placed on the perimeter, but only two of them were on the corners. This resulted in a slightly different current injection pattern as compared with the other four samples. The typical sample

contacts layout for the samples is shown in figure 3-3(a). The contacts for (45°, 0.5T) is as shown in figure 3-3(b).

Voltage measurements made on each sample were V_{xx}, V_{yy}, and diagonally, V_{d1} and V_{d2}, with respective applied currents, I_x, I_y, I_{d1}, and I_{d2}, as diagrammed in figure 3-4 where voltage paths are schematically shown as dashed lines between two contacts with arrows pointing to the low potential side, and current paths are schematically shown as solid lines between two contacts with arrows pointing to both sides since each voltage datum recorded was an average of two measurements (taken within 0.1 seconds) with the current in opposite directions.

The voltages were then divided by the respective currents and converted to resistances, R_{xx}, R_{yy}, R_{d1}, and R_{d2}. To obtain longitudinal resistivity from measured resistances (van der Pauw, 1958),

$$\rho_{xx} = \tfrac{1}{2}(\pi d/\ln 2)(R_{xx} + R_{yy})f(R_{xx}/R_{yy}),$$

where d is the sample thickness, and f satisfies the relation

$$(R_{xx} - R_{yy}) / (R_{xx} + R_{yy}) = f\cosh^{-1}[\tfrac{1}{2}\exp(\ln 2/f)].$$

We have approximated the function f by,

$$f(x) \sim 1 - x^2(\ln 2/2) - x^4\{(\ln 2)^2/2 - (\ln 2)^3/12\} - x^6\{(\ln 2)^2/2 + (\ln 2)^3/12 + (\ln 2)^4/2\},$$

where $x = (R_{xx} - R_{yy}) / (R_{xx} + R_{yy})$. Since x enters the equation only as powers of x^{2n}, for n = 0, 1, 2, 3, it is irrelevant whether R_{xx} or R_{yy} has the larger magnitude. This approximation was empirically derived to fit (within 2%) figure 7 of van der Pauw (1958), for x from 1 to ~ 10^2. The approximation to this accuracy is required, since a van der Pauw correction to each measurement at a given temperature and field must be made for accurate results, particularly at temperatures and fields near T_c.

R_{xx} and R_{yy} versus temperature data measured in an applied magnetic field of 2 Tesla parallel to the samples' c-axes are shown in figure 3-5(a) and (b) for the (ag) and (C,2T), respectively. The data is typical of the data of the irradiated samples when the field is aligned along the columnar defects. The onset of the dissipation in the XX and YY directions is nearly simultaneous in temperature. The ratio of R_{xx} / R_{yy} versus temperature data measured in an applied magnetic field of 2 Tesla parallel to the samples' c-axis is shown in figure 3-6(a) and (b) for (ag) and (c, 2T), respectively. As is seen in 3-6(a), the ratio R_{xx} / R_{yy} is nearly constant over the temperature range of interest. Therefore, an average value for the van der Pauw function, f(x) appears acceptable, as there is only a deviation from its approximate value over a narrow temperature interval, about 0.3K. This same deviation for (c, 2T) occurs over a 1 K temperature interval, and is not acceptable, as is evident in fig 3-6(b).

The average f(x) value method of determining resistivity is inaccurate when the applied magnetic field is aligned with the columns. R_{xx} and R_{yy} versus temperature data measured in an applied magnetic field of 2 Tesla at $\theta = 51^\circ$ for (ag) and $\theta = 45^\circ$ for (c, 2T)

are shown in figure 3-7(a) and (b). The onset of dissipation in the YY direction is shifted to a higher temperature than the onset in the XX direction for (c,2T), when the applied magnetic field is along the sample c-axis, as is shown in figure 3-7(b). The ratio of R_{xx} / R_{yy} versus temperature data measured in an applied magnetic field of 2 Tesla at $\theta = 51^{\circ}$ for (ag) and $\theta = 45^{\circ}$ for (c, 2T) are shown in figure 3-8(a) and (b). The ratio R_{xx} / R_{yy} shows an order of magnitude of variation in the temperature range of interest for (c, 2T). This results in a 60% variation in the f(x) function of van der Pauw over the temperature range of interest. Therefore, temperature by temperature van der Pauw corrections are required to accurately obtain the longitudinal resistivity.

The van der Pauw corrections are applicable in the linear current-voltage response regime. Throughout the flux flow regime, and in the normal state, in the linear current-voltage response regime, the ratio $R_{xx}/R_{yy} \approx$ constant. When there is no dissipation, the voltage response is not considered to be linear in current. Therefore, in the temperature regions where R_{xx} is > 0, and R_{yy} is measured as zero or noise, the van der Pauw corrections are no longer meaningful. In the regions where $R_{yy} > 0$, the ratio $R_{xx}/R_{yy} \approx$ constant. Furthermore, R_{xy} has onset of sign reversal (beyond noise) at a higher temperature (or field) than the onset of dissipation for R_{yy}. Consequently, little Hall resistivity data are avaliable outside of the region where $R_{xx}/R_{yy} \approx$ constant, and for analyses in this thesis, only data in the region where the ratio $R_{xx}/R_{yy} \approx$ constant are used.

To obtain Hall resistivity, a modified van der Pauw Hall resistivity correction, developed by M. Konczykowski (1994), is used. The technique developed by M. Konczykowski, is actually the van der Pauw Hall resistivity correction applied two

different ways and averaged. The Hall resistance, using the van der Pauw method, is given by (van der Pauw, 1961),

$$R_{xy} = R_{d1} - R_{yy} + R_{xx}.$$

The Hall resistance, using the Konczykowski method, is (Konczykowski, 1994),

$$R_{xy} = \tfrac{1}{2}(R_{d2} - R_{d1}).$$

Effectively, van der Pauw has logically assumed that in zero magnetic field, the difference $R_{xx} - R_{yy} = R_{d1}$, as is required for no current or voltage source or sink within the sample. Therefore, in a magnetic field, whatever remains is the Hall resistance. The Hall resistivity is equal to the Hall resistance multiplied by the sample thickness (van der Pauw, 1961).

The modified van der Pauw correction for Hall resistance is more clear when considering V_{d1} and V_{d2} in figure 3-3. Clearly, subtracting $V_{d2} - V_{d1}$ removes the longitudinal components of the diagonal potential differences, and sums of the transverse (Hall) components. The resultant Hall voltage is (Konczykowski, 1994),

$$V_{xy} = (V_{d2} - V_{d1})/2.$$

Again, the Hall resistance is obtained by dividing the measured voltages by their respective currents, and the Hall resistivity is equal to the Hall resistance multiplied by the sample thickness (van der Pauw, 1961).

Each measurement was repeated nine times, sequentially at a given temperature and field, (drift in temperature during each measurement was negligible) and averaged, effectively reducing noise by a factor of 3. That the repeated measurements at the given current did not heat the sample was determined by measuring the voltage as a function of current at a fixed temperature and field, and examining the I-V curves.

Thickness

The thickness of each sample was measured using an optical microscope. Resolution of the measurement was to within ±3 microns. The actual limitation of the measurement is that the samples are not flat along the edge. Variations in edge thickness of up to 2-4 microns were observed on some of the samples.

Electrical Transport Measurements

Longitudinal and Hall resistivities, as measured and described above, were obtained versus field, at fixed temperatures, temperatures, at fixed fields, all at various angles and currents as outlined in the table below. Temperature intervals in regions of interest were about 0.05K. Field intervals were 0.1 Tesla. In each temperature and field

region, current-voltage measurements of the same orientations as the resistivities were obtained to ensure that all measurements were conducted in the linear ohmic regime, and that no heating was present. Temperature-dependent measurements were made on the five samples at five different constant applied magnetic fields of H = 1, 2, 3, 4, and 6 Tesla, at various angles θ. Magnetic field dependent measurements were made from 0 to 6 Tesla at three constant temperatures of T = 88.0, 90.0, and 92.0 K, and again at various angles θ.

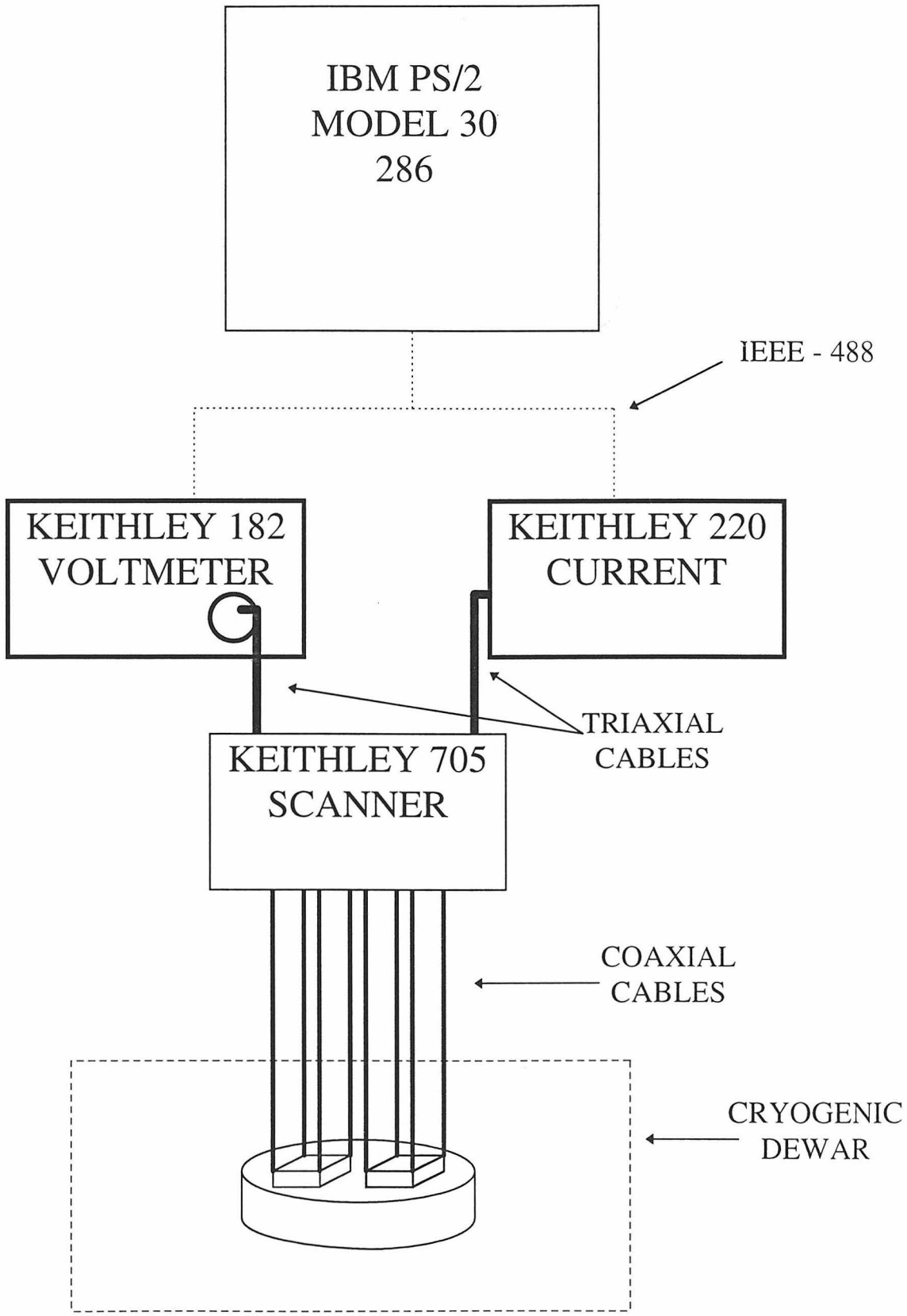

Figure 3-1 DC Functional Diagram

Sample	thickness	irradiation orientation	T_c fluence (cm^{-2})		B_ϕ	identification
1	42.7 μm	as grown	0	92.94 K	0T	(ag)
2	37.7 μm	c-axis	10^{11}	92.74 K	2T	(c, 2T)
3	21.0 μm	45°	10^{11}	92.96 K	2T	(45, 2T)
4	26.3 μm	c-axis	$2.5x10^{10}$	92.57 K	0.5T	(c, 0.5T)
5	18.9 μm	45°	$2.5x10^{10}$	92.81 K	0.5T	(45°, 0.5T)

Table 3-1 $YBa_2Cu_3O_7$ single crystals used in DC electrical transport experiments.

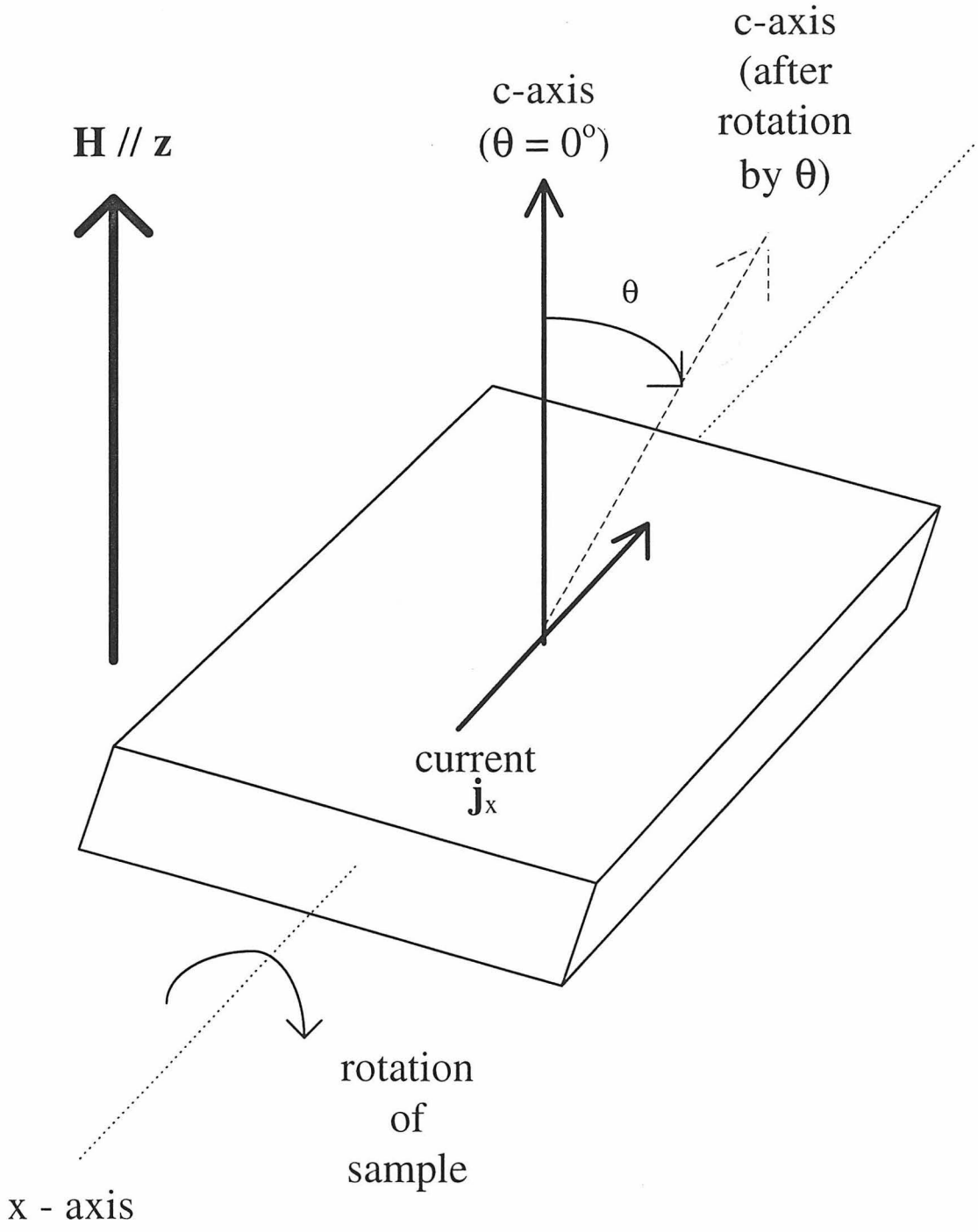

Figure 3-2 Field, Current, Sample c-axis Orientations

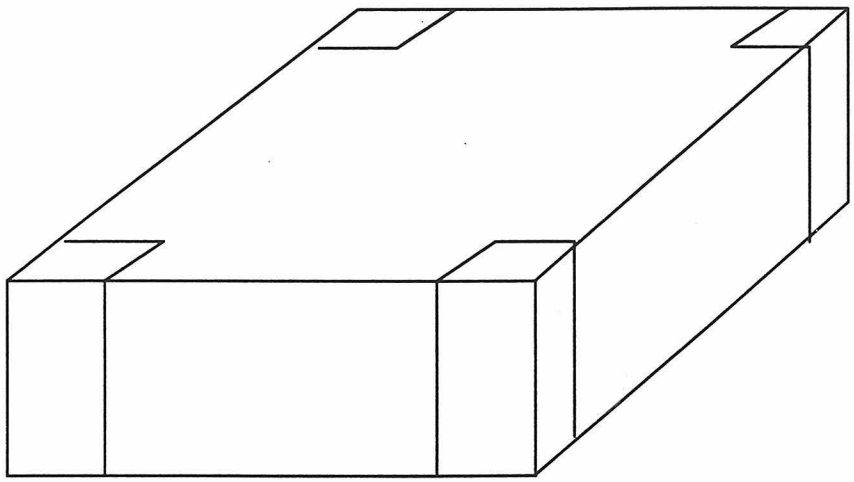

TYPICAL CONTACT
LAYOUT

(a)

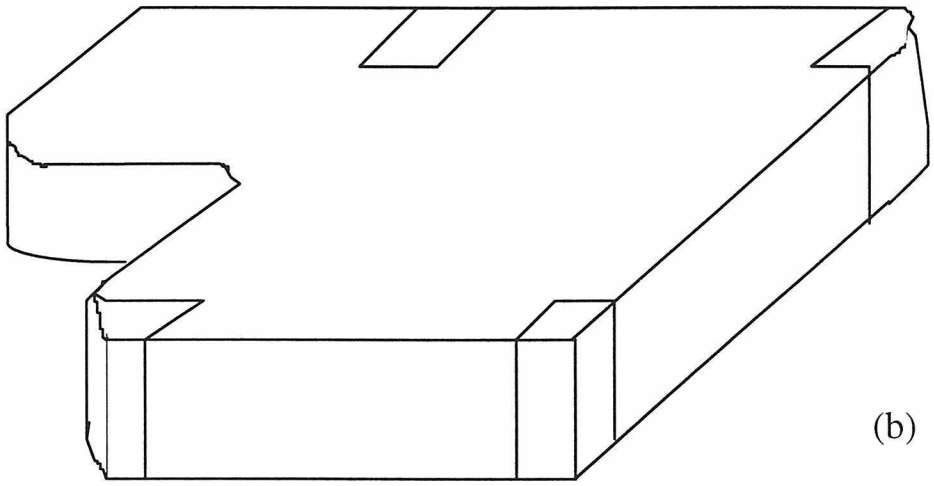

(b)

LAYOUT FOR
(45°, 0.5T)

Figure 3-3 Contact Layouts
(a) contacts for (ag), (c, 2T), (45°, 2T),
and (c, 0.5T), (b) contacts for (45°, 0.5T)

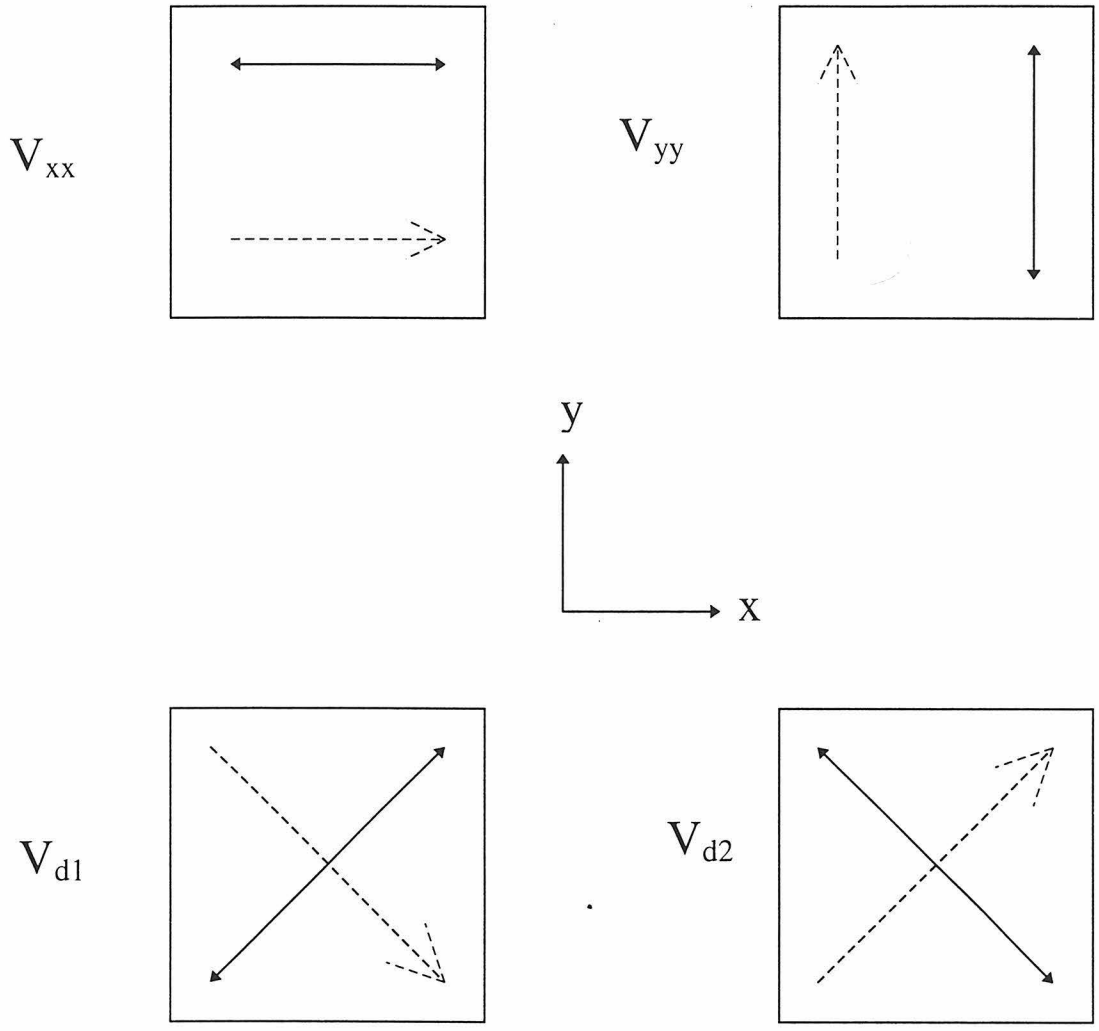

Figure 3-4 Voltage and Current Measurement Orientations

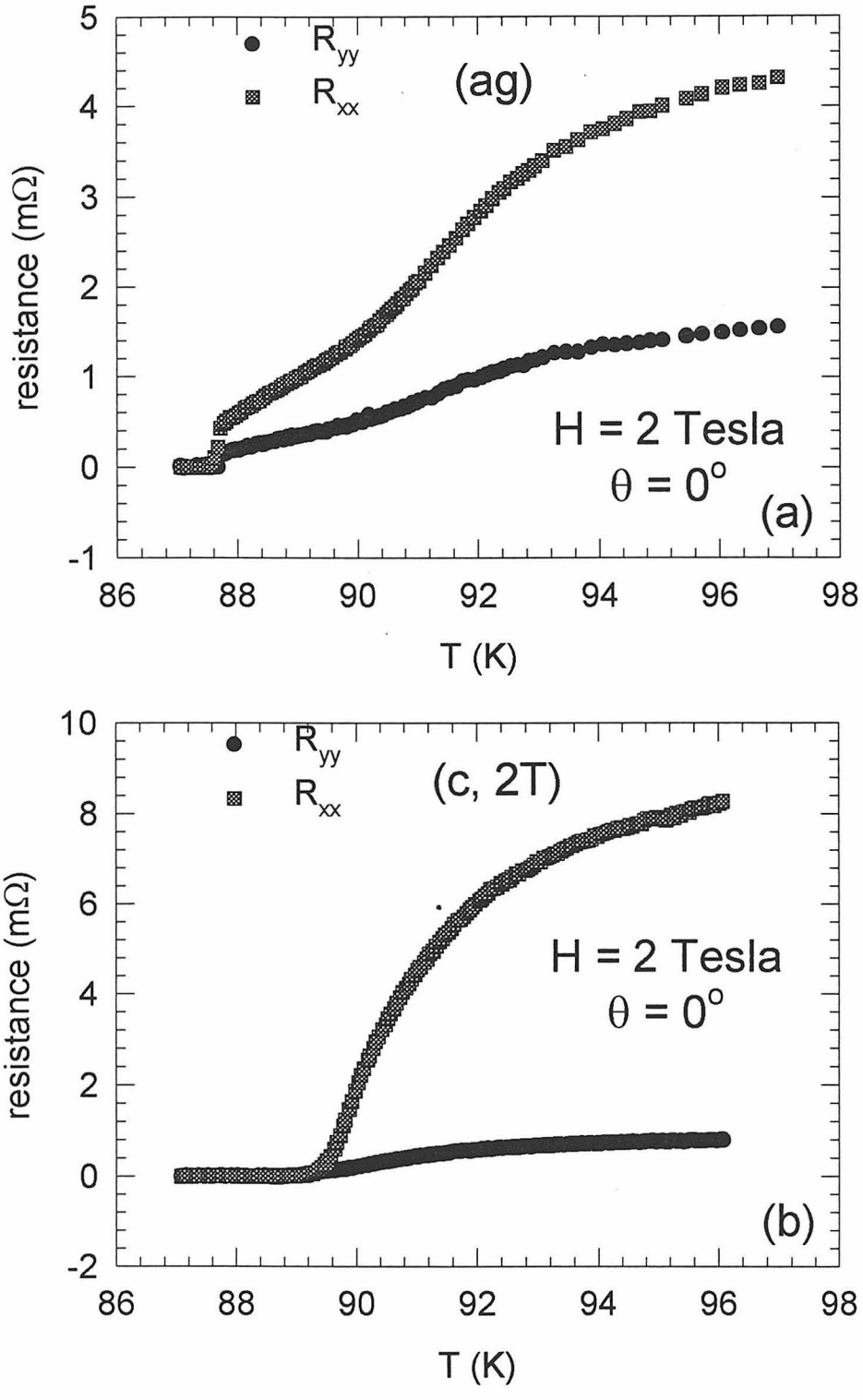

Figure 3-5 R_{xx} and R_{yy} versus temperature for (ag) and (c, 2T). A comparison of the loss of resolvable signal versus temperature for H // c-axis.

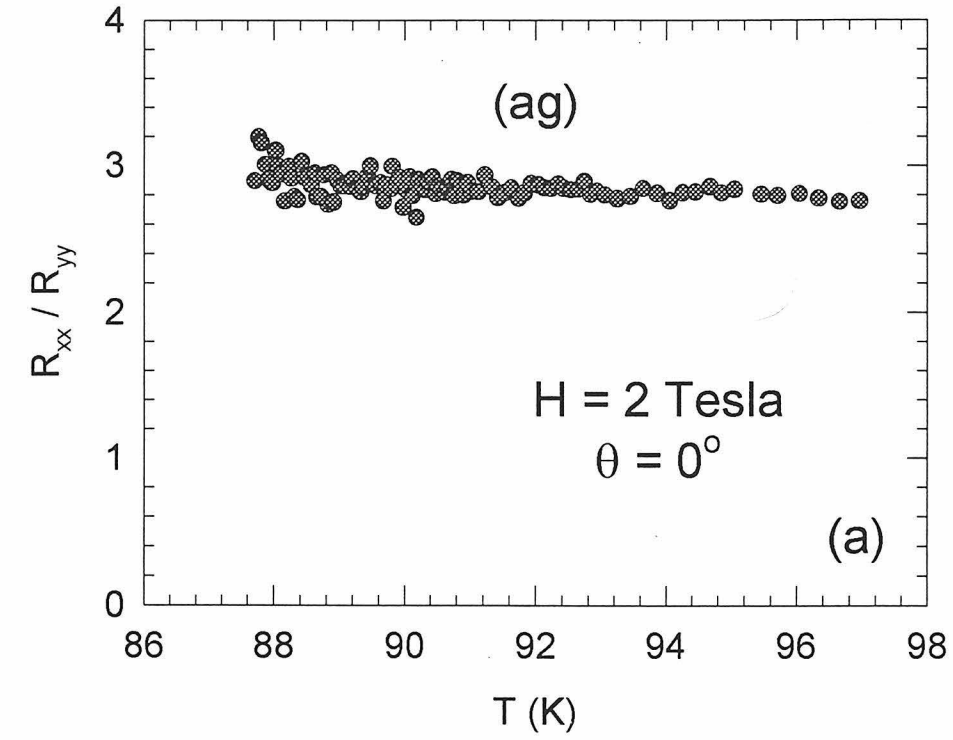

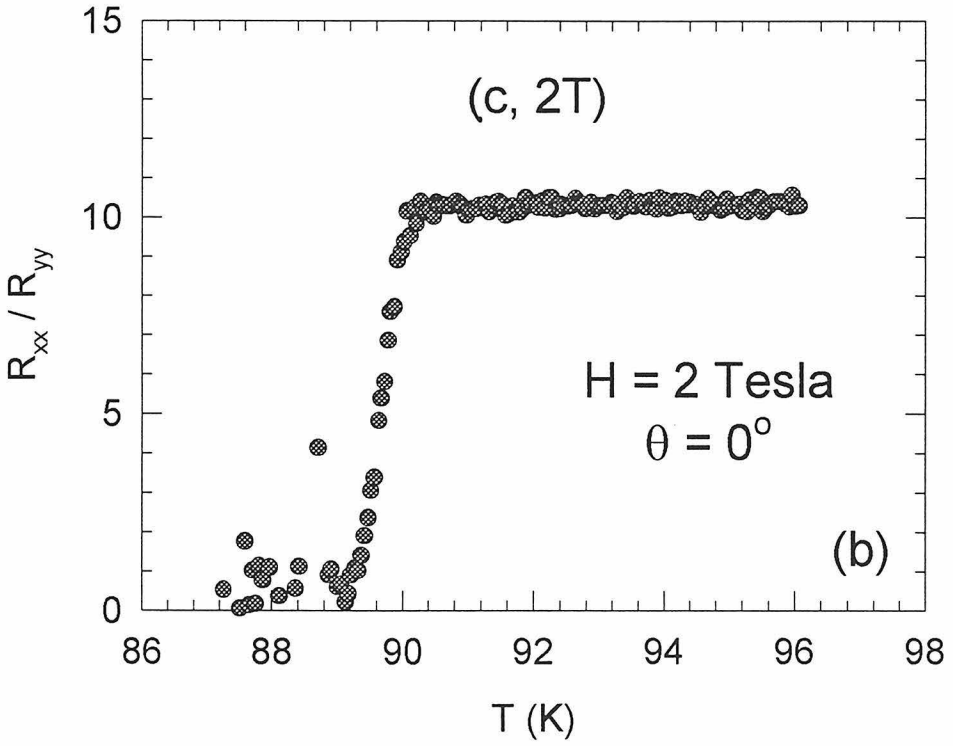

Figure 3-6 R_{xx} / R_{yy} vs temperature for (ag) and (c, 2T)

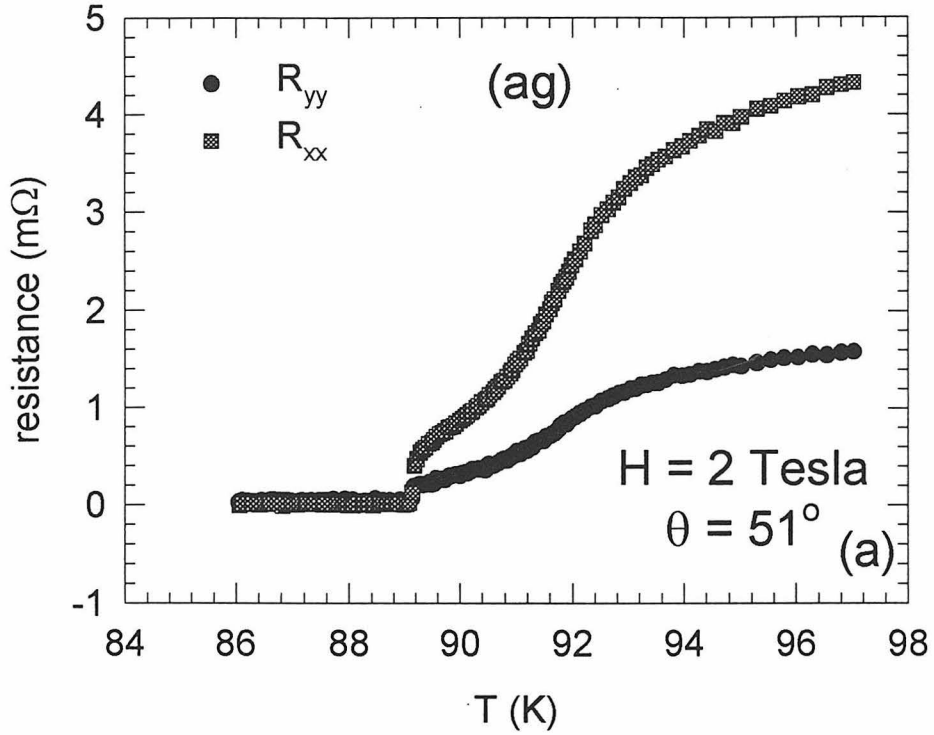

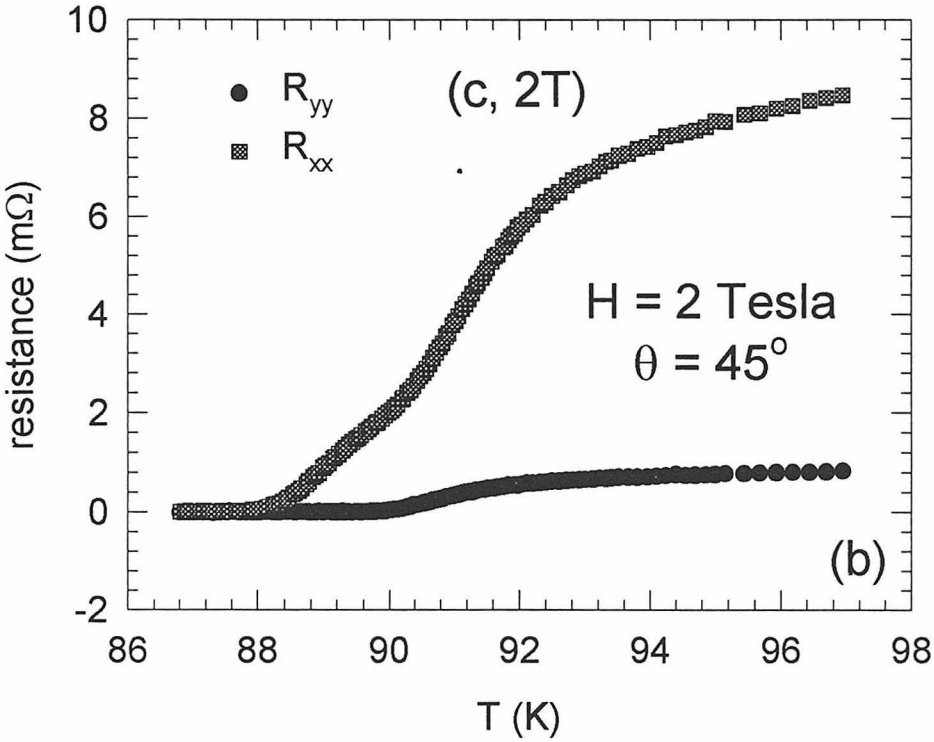

Figure 3-7 R_{xx} and R_{yy} versus temperature for (ag) and (c, 2T)

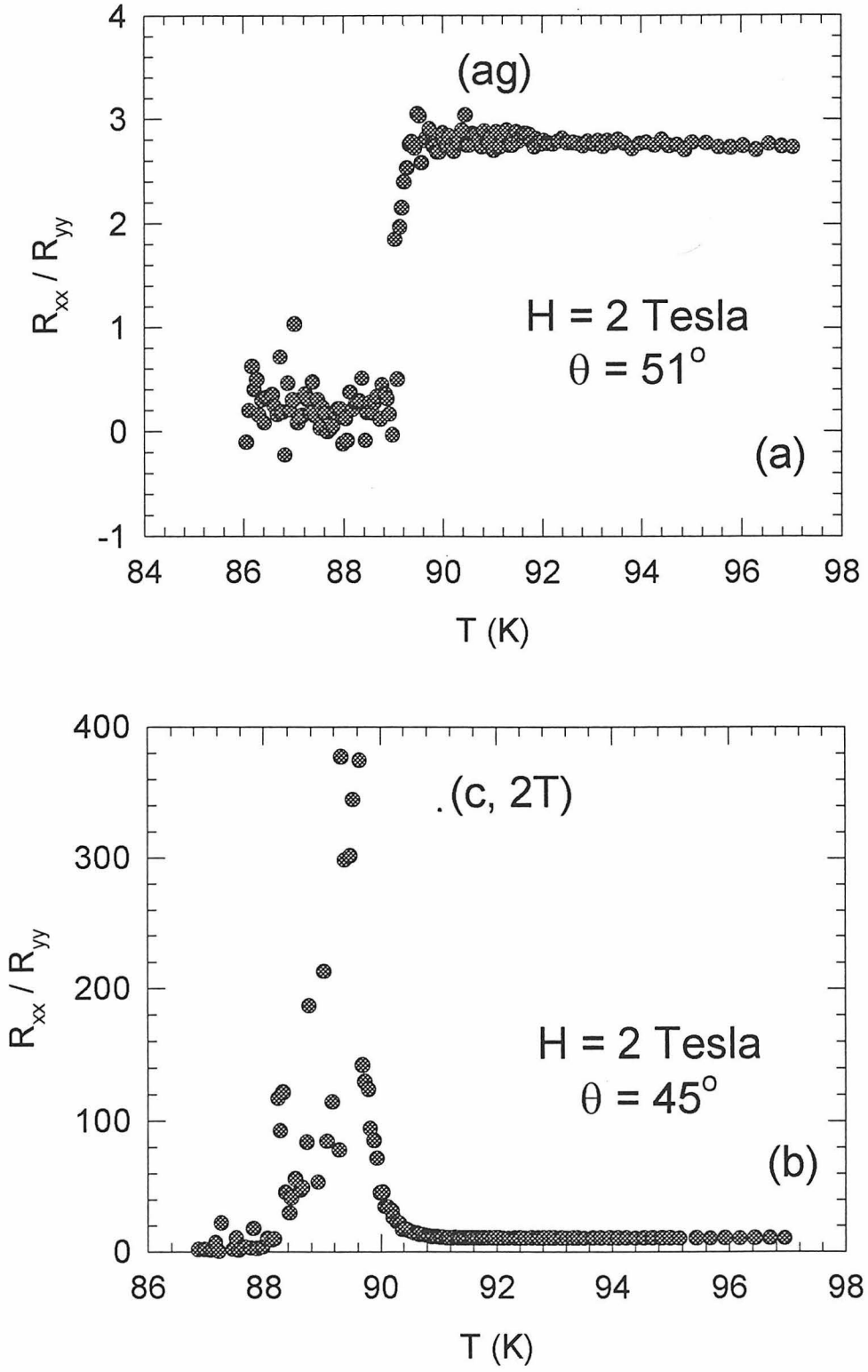

Figure 3-8 R_{xx} / R_{yy} vs temperature for (ag) and (c, 2T)

Chapter Four: Analyses, Results and Discussion of the DC Electrical Transport Measurements

This chapter describes the analyses, results, and discussions of the DC electrical transport measurements. The conversion of the measured data to van der Pauw (1958 and 1961) corrected longitudinal and Hall resistivities was discussed in chapter 3. The work in this chapter takes the van der Pauw data as its working (raw) data. Although the use of computer programs to "smooth" data for a "better presentation" seems to be a common practice by many, no smoothing of data was done in this thesis. Transition temperatures and widths will be determined. A comparison of the zero-field longitudinal resistivities will be made for the five $YBa_2Cu_3O_7$ single crystals. The effects of the columnar defects on longitudinal resistivities and Hall resistivities will be examined. That the measurements are conducted in the linear response regime will also be verified. The longitudinal and Hall resistivity data will be converted to Hall conductivity data. Aspects of the universal Hall conductivity will be examined and discussed. Transport scattering times will be derived from the Hall conductivity data using the model describing the origin of the sign reversal in the vortex state Hall conductivity by Feigel'man et al.(1995), and compared with those derived from other measurements.

To make meaningful comparisons among samples with different degrees of disorder, it is important to determine T_c accurately. However, the empirical T_c determination varies throughout literature. Most use the resistive transition versus temperature. Some use the $0.1\rho_{xx}^n$ temperature, and others the $0.9\rho_{xx}^n$ temperature of the resistive transition. (ρ_{xx}^n is the normal state resistivity, often chosen as the resistivity at the

point where the resistivity versus temperature curve first varies (decreases) from normal behavior, also called , T_c onset,T_{co}.) Others use the midpoint of the resistive transition, even though the transition is asymmetric. Of course, there are differences as to at what temperature one considers the superconductor to be normal. Others quote the peak change in resistivity with respect to temperature as the T_c. The most stringent way of determining T_c is to analyze the paraconductivity above T_c according to the Aslamosov-Larkin theory (Aslamasov and Larkin, 1968). The fluctuations above T_c contribute additional conductivity, beyond the normal DC conductivity in the absence of superconducting fluctuations. This excess conductivity, $\Delta\sigma$, has a temperature dependence $\Delta\sigma \propto (T - T_c)^{-(4-d)/2}$, where d(=1,2,3) is the dimensionality of the system (see Tinkham, section 7-6, 1975). In this work, an empirical approximation, which involves a geometric construction attempting to consider the effects of fluctuations near the transition, will be used to determine T_c of the samples.

Well above the superconducting to normal transition, the longitudinal resistivity versus temperature is known to be linear in optimally-doped high-temperature superconductors (e.g., Rice et al., 1991; Samoilov, 1994). From this, one line is obtained, collinear with the well above transition temperature resistivity data. Below the transition, but above the onset of dissipation, there is a small temperature interval where the resistivity rises rapidly with increasing temperature. Taking the maximum slope through the temperature at which the maximum of $d\rho / dT$ occurs, a second line is obtained. The temperature at which these two lines intersect is considered to be the superconducting

transition temperature, T_c. This construction is as shown in figure 4-1 for the as-grown sample.

The effects of the columnar defects on the longitudinal resistivity, $\rho_{xx}(T)$, versus temperature, T/T_c are as shown in figure 4-2. In this figure, it is evident that the columnar defects cause a decrease in the transition temperature of a maximum of 0.15K.

The difference between the actual T_c's, for example the extremes of (45,2T) at 92.96K and (c, 0.5T) at 92.57K does not consider the changes in the setup of the measurement system, the setup of the probe, nor changes in the temperature controller, that occurred in the one year interval between measuring these two samples. Changes in the system setup include improved shielding of the coaxial cables and improved grounding of various instruments. Changes in the setup of the probe include rewiring of the temperature sensor, removing and replacing the coaxial cables (with a different type), changing the heat sinking of the cables, more firmly fixing the position of the temperature sensor for better thermal contact. Changes in the temperature controller, include upgrading the temperature controller software, changing its eeproms, improving its grounding, and shipping it to the factory for upgrades and calibrations. The drift of the temperature sensor calibration, with approximately one year of almost continuous use during other experiments, between measuring these two samples, must also be considered. This is in agreement with the work of Samoilov et al., (1995), where it was observed the shift if transition temperature to not change by more than ~ 0.3K. Kang et al. claimed a difference in the T_c of 0.7K between that of the as-grown sample and the irradiated sample used in their work. This large temperature shift may be an indication of severe damage to

the sample quality. Additionally, the temperature calibration of Kang et al. is brought into question, since they reported a $YBa_2Cu_3O_7$ single crystal $T_c = 93.8$ K, approximately 0.5 K higher than typically reported for fully oxygenated $YBa_2Cu_3O_7$ single crystals.

Columnar defects affect the longitudinal resistivity of the samples in a fixed applied magnetic field. The longitudinal resistivity versus temperature curves for the five samples in a fixed applied magnetic field of 2 Tesla at angles relative to the samples' c-axes of 0° and 45°, are shown in figure 4-3(a) and (b) respectively. It is evident that the columnar defects affect the longitudinal resistivity. First, there is a significant reduction in the mixed-state longitudinal resistivity, ρ_{xx}. Secondly, the onset of dissipation varies with alignment of the applied magnetic field with the columnar defects. The (ag) sample has resistivity at the lowest temperatures among the samples for all conditions. This is an indication that the vortices are least pinned in this sample. From this, it can also be inferred that it has the lowest vortex-solid to vortex-liquid transition temperature, as dissipation in superconductors is associated with vortex motion. The (ag) sample appears to be the most heavily twinned, yet it shows a significantly smaller effect of pinning due to the presence of twin boundaries relative to that due to columnar defects when the applied magnetic field is aligned with the twins. This result is not surprising, considering that the areal density of the twin boundaries is much smaller than that of the columnar defects in the samples used for this study. In addition, the dimension of the columnar defects provides more efficient pinning due to its comparable size to the superconducting coherence length. Hence the samples with columnar defects have the onset of dissipation

shifted to higher temperatures. The shift increases with increased columnar defect density and when the magnetic field is aligned with the columnar defects.

It is obvious that defects would affect dissipation in the creep and thermally assisted flux flow regimes. The suppression of the longitudinal resistivity in the flux flow regime, where pinning is supposed to be irrelevant, is due to the enhancement of the vortex-solid to vortex-liquid transition temperature incurred by columnar defects if the magnetic field is aligned with the columns, as stated in chapter 2. When the magnetic field is not aligned with the columns, in addition to the enhancement of the vortex-solid to vortex-liquid transition temperature, there is a difference in the vortex-solid to vortex-liquid transition temperatures in the xx and yy directions , as discussed in chapter 3. The flux flow regime is the linear current-voltage response vortex-state regime. An example a of linear current-voltage response is shown in figure 4-4 for (45°, 2T) measured at a fixed applied magnetic field of 1 Tesla at $\theta = 45°$. The current-voltage response was confirmed for all samples in all regimes reported in this investigation.

Summarizing the above results, columnar defects cause a significant reduction in the mixed-state longitudinal resistivity. The columnar defects also cause the onset of dissipation to move to higher temperatures for given fields, and to higher fields for given temperatures, when the applied magnetic field is aligned with the columnar defects (or aligned within a field, temperature and current density dependent accommodation (depinning) angle relative to the columnar defects (Fleshler et al., 1993)). Additionally, effects of the columnar defects are observed in the region above, in temperature or field, the onset of dissipation.

Two effects from the presence of columnar defects are evident in the Hall resistivity, ρ_{xy}, versus temperature data. When the applied magnetic field is aligned with the columnar defects, the ρ_{xy} data shows a shifting of the minimum of the ρ_{xy} curve towards higher temperatures. Another effect is that the magnitude of ρ_{xy} is decreased by the presence of the columns as compared to the data of the as-grown sample, for all angles. Hall resistivity data versus temperature at a fixed field of 2 Tesla with $\theta = 0^\circ$ is shown in figure 4-5 for all five samples.

Resistivities, longitudinal and Hall, are strongly affected by the presence of columnar defects. The shape of the resistive transition has only a few markers, such as the occasional "kink" or shoulder, the loss of resolution and the onset of transition from normal to superconducting, and the Hall resistive minimum and zero crossing. When columnar defects are induced in the sample, these markers, and even the shape of the resistive curves, change dramatically. The microscopic understanding is challenging. Additionally, Hall resistivity is considered separately from longitudinal resistivity, even though the two are intuitively coupled. Consequently, it is challenging to derive an understanding of the electrical transport mechanism in the vortex-state from the resistive data.

Hall Conductivity

The electrical transport mechanisms in the vortex-state are more easily understood when the mixed state Hall conductivity is examined. Numerous authors have described

the mixed state Hall using two terms. The approach is to divide mixed state Hall conductivity into a normal part and a superconducting part. This makes sense intuitively, as for $0 < T < T_c$, there are quasiparticle excitations (broken Cooper pairs) within the Bose condensate. Using two terms to describe a normal and a superconducting part is reasonable, particularly in the presence of vortices, because quasiparticle excitations exist within the approximately normal vortex core, and pairing dominates outside far away from the core. Additionally, the Hall conductivity may be described using only one relaxation time, τ.

The transformation from longitudinal and Hall resistivities to Hall conductivity is obtained by inverting the resistivity matrix such that,

$$\sigma_{xy} = \rho_{xy} / (\rho_{xx}^2 + \rho_{xy}^2),$$

where $\rho_{xy}(\mathbf{H}) = -\rho_{yx}(\mathbf{H})$ through the Onsager relations (Onsager, 1931) and $\rho_{xx} = \rho_{yy}$ as measured after the van der Pauw corrections (van der Pauw, 1958). Possible large errors in the low temperature σ_{xy} data due to rapidly vanishing ρ_{xx} and ρ_{xy} can occur. The analyses of the vortex-state Hall conductivity data are therefore restricted to temperatures above a lowest T*, where $T^* < T_{min}$ and $\rho_{xy}(T^*) = 0.25\rho_{xy}(T_{min})$, and T_{min} is the temperature at which ρ_{xy} is a minimum. The analyses of the σ_{xy} data are also restricted to this temperature range because the van der Pauw corrections are valid in the linear response limit, and this restriction assures that the analyses are done in the linear response

regime of the samples. As mentioned above, the linear response regime is verified by measuring a linear current-voltage relation of each sample.

The Hall conductivity is then broken into two terms,

$$\sigma_{xy} = \sigma_{xy}^{s} + \sigma_{xy}^{n},$$

where σ_{xy}^{s} is the superconducting part (involving Cooper pairs and vortex motion) of the Hall conductivity in the mixed state, and σ_{xy}^{n} is the normal part (involving quasiparticles) of the Hall conductivity.

Typically, it has been assumed that the quasiparticle excitation contribution to the Hall conductivity in the mixed state is equivalent to that from the normal area within the cylindrical vortex cores of the model. The success of early models (Bardeen and Stephens, 1965; Nosiéres and Vinen, 1966) relative to the typical (non-anomalous) Hall effect of many conventional type II superconductors has entrenched this belief. The models of Khomskii and Freimuth (1995) and Feigel'man et al. (1995) require a redistribution of quasiparticles to allow for quasiparticle excitations external to the vortex cores. To verify the validity of both approaches requires experiments that measure the changes in the chemical potential to independently validate the quantitative δn relations. Khomskii and Freimuth relate δn to changes in the chemical potential and to changes in density of states with respect to the change in energy near the Fermi level. Feigel'man et al. relate δn to the change in $\ln(T_c - T)$ with respect to the change in the chemical

potential. It is believed that the redistribution of quasiparticles in the vortex-state results in the anomalous sign reversal in σ_{xy}.

In what follows, the universality of Hall conductivity in the vortex-liquid state of $YBa_2Cu_3O_7$ single crystals will be demonstrated. First, the Hall conductivity versus temperature for the various samples at an applied magnetic field of 2 Tesla parallel to the samples' c-axes will be used to demonstrate the defect independence of the Hall conductivity versus reduced temperature. Next, for the first time, anisotropic scaling of the Hall conductivity will be shown versus temperature and versus applied magnetic field. The current independence of the Hall conductivity will also be shown. Finally, an examination of the Feigel'man et al.(1995) equations for the Hall conductivity will be presented, and the carrier transport time will be extracted and compared with other relevant time scales in the mixed state.

The Hall conductivity versus reduced temperature at an applied magnetic field of 2 Tesla and $\theta = 0^\circ$ and 45° is shown for the five samples in figure 4-6(a) and (b) respectively. As is evident in figures 4-8(a) and (b), the complex state Hall conductivity, σ_{xy}, is universal for all samples for the given applied magnetic field strength (H) and orientation(θ) relative to the crystalline c-axis. It is clear from the data in figures 4-6(a) and (b) that the angular dependence of the vortex state σ_{xy} is also universal among the five $YBa_2Cu_3O_7$ single crystals. The shift in temperature upward for each curve with increasing angle of the applied magnetic field indicates the presence of anisotropy. That all samples show the same shift with applied magnetic field, independent of alignment of

the field with the columnar defects implies that the columnar defects do not change the anisotropy within the resolution of this data.

Extending the anisotropic scaling relations of the Hall conductivity [Blatter et al. (1992) and Geshkenbein and Larkin (1994)] to this expression,

$$\sigma_{ik}(T,H,\theta) = \sigma_{xy}(T,\varepsilon_\theta H,\theta = 0)\varepsilon_{ikl}H_l/\varepsilon_\theta H,$$

where $\varepsilon_\theta = (\cos^2\theta + \varepsilon^2\sin^2\theta)^{1/2}$, and $\varepsilon^2 = m_{ab} / M_c$ is the mass anisotropy ratio. Equation (4-1) then becomes,

$$\sigma_{xy}(T,H,\theta) = \sigma_{xy}(T,\varepsilon_\theta H,\theta = 0)\varepsilon_{xyz}H_z/\varepsilon_\theta H.$$

where $\varepsilon_{xyz} = 1$. For z along the c-axis, and θ the angle of the applied magnetic field relative to the sample c-axis, σ_{xy} scaling become,

$$\sigma_{xy}(T,H,\theta) = \sigma_{xy}(T,\varepsilon_\theta H,\theta = 0)\cos\theta/\varepsilon_\theta.$$

The predominant anisotropy is that between the ab planes and the c-axis, as defined by the mass anisotropy ratio. Note that the anisotropy between the a and b axes is not a factor since all samples used in this experiment are twinned. The vortex-state σ_{xy} versus T/T_c data, with H = 2 Tesla and oriented at various angles (θ) relative to the sample c-axis, is plotted in figure 4-7(a) for (c, 0.5T). The angular dependence is

entirely determined by the mass anisotropy. According to the anisotropic-to-isotropic scaling transformation relations of the anisotropic Ginzburg-Landau theory (Blatter et al., 1992), the scaled Hall conductivity, $\widetilde{\sigma}_{xy}(\equiv \sigma_{xy}\sqrt{1 + \varepsilon^2 \tan^2\theta})$ is uniquely determined by the reduced temperature ($\widetilde{T} / \widetilde{T}_c = T / T_c$) and the scaled field $\widetilde{H} = H\sqrt{\cos^2\theta + \varepsilon^2 \sin^2\theta}$, where $\varepsilon^{-2} \equiv (m_c/m_{ab}) \approx 60$ (this work, and Blatter et al., 1994) is the effective mass ratio for $YBa_2Cu_3O_7$. Scaled $\widetilde{\sigma}_{xy}$ versus T/T_c data for a scaled field of $\widetilde{H}$ = 2 Tesla at $\theta = 0°$, 45°, and 60° is plotted in figure 4-7(b) for (c, 0.5T). To be precise, to scale with fields different by a factor of two, the angle should be approximately 60.8 degrees for scaling with fields and an angle of zero degrees. This discrepancy is not apparent in the data as the difference is within the angular error and overall system resolution. Scaled $\widetilde{\sigma}_{xy}$ versus T/T_c for scaled fields $\widetilde{H}$ = 2 Tesla and $\widetilde{H}$ = 1 Tesla is shown in figure 4-8 for the four $YBa_2Cu_3O_7$ single crystals with columnar defects, for the magnetic field oriented at 0°, and 60^0. Similarly, σ_{xy} versus H data at $T/T_c \approx 0.97$ is shown in figure 4-9(a) for the as-grown $YBa_2Cu_3O_7$ single crystal. This data scaled as $\widetilde{\sigma}_{xy}$ versus $\widetilde{H}$, for $T/T_c \approx 0.97$ is shown in figure 4-9(b).

The defect-independence of the Hall conductivity, originally derived by Vinokur et al.(1993) for random point defects, appears to hold even for correlated disorder, at least in the flux-flow regime of the vortex state. This universal behavior in σ_{xy} is in sharp contrast

to the significant reduction in the mixed-state longitudinal resistivity, ρ_{xx}, and in the magnitude of the sign reversed Hall resistivity, ρ_{xy} due to the presence of columnar defects. (See figures 4-3(a) and (b).) In the linear response regime, the reduction of ρ_{xx} below T_c for samples with columnar defects is not due to pinning of vortices. The major effect in the vortex-state associated with the presence of columnar defects is the increase of the vortex transition temperature (between the "Bose-glass" vortex-solid state and the vortex-liquid state) relative to that in the absence of columnar defects.

The current independence of the Hall conductivity is examined in figures 4-10(a) and (b). The Hall conductivity versus applied magnetic field at a reduced temperature $T = 0.98T_c$ is shown in figure 4-10(a) for the as-grown sample at three current densities, $2.8\text{x}10^3$ A/m^2, $1.4\text{x}10^4$ A/m^2, and $1.4\text{x}10^5$ A/m^2, and the Hall conductivity versus reduced temperature is shown in figure 4-10(b) for (c, 2T) at the current densities, $1.3\text{x}10^4$ A/m^2 and $7.5\text{x}10^4$ A/m^2. Two main differences occur with increased current density. The measurement noise is reduced by approximately a factor of 3 by increasing the current density an order of magnitude. This is reasonable, as the Hall voltage signal is proportional to the current density, and so the increased signal to noise ratio translates to less noise in the data. The other difference with increased current density is that the range of resolution is extended to lower temperature regions. This is due not only to the increased signal to noise ratio, but that at higher current densities, the crossover from the current dominated vortex response region to the thermally dominated response region is extended to lower temperatures [Yeh (1993)].

The Feigel'man et al. (1995) model describes σ_{xy} as,

$$\sigma_{xy} = \frac{nec}{B}\left[g\frac{(\omega_o\tau)^2}{1+(\omega_o\tau)^2} - \frac{\delta n}{n}\right] + \sigma_{xy}^{n}(1-g), \quad \sigma_{xy}^{n} \equiv \frac{nec}{B}\frac{(\omega_c\tau)^2}{1+(\omega_c\tau)^2},$$

where n is the total carrier density, $\delta n(\equiv n_o - n_\infty)$ satisfies $\delta n \ll n(\approx n_o \approx n_\infty)$, and $\delta n(T\rightarrow 0) \rightarrow$ constant and $\delta n(T\rightarrow T_c^-) \rightarrow 0$. $\omega_o = eB/mcf(B/H_{c2})$, where $f(B/H_{c2}) = 1$ for $B > H_{c2}$, and $f \propto B/H_{c2}$, for $B \ll H_{c2}$. $\omega_o \approx \Delta^2/\hbar\varepsilon_F$ for $B \ll H_{c2}$ in clean materials, and is the level spacing between localized states in the normal core. $\Delta = \Delta(T)$ is the temperature dependent superconducting energy gap, and ε_F is the Fermi energy. σ_{xy}^{n} is the normal state Hall conductivity, and $\omega_c \equiv eB/mc$, is the cyclotron frequency of the normal carriers. $g = g(\Delta/T)$ such that $g(x\rightarrow\infty)\rightarrow 1$, and $g(x\rightarrow 0) \approx x$. $\delta n/n \sim (\Delta/\varepsilon_F)^2$, is for an unscreened superconductor model, and, with screening taken into account, $\delta\tilde{n}/n \approx \text{sign}(\delta\tilde{n})(\Delta/\varepsilon_F)^2$ (Feigel'man et al. (1995) for all definitions and relations).

Using the approximations above for $\delta n/n$, ω_o, and g, an approximate carrier transport time, τ, can be determined. Caution is advised that although this procedure will produce a temperature dependence of τ, neither meaning nor validity of the temperature dependence should be inferred. At best, τ derived using the approximations gives insight into the order of magnitude of τ. For $\delta n/n \approx (\Delta/\varepsilon_F)^2$ (Feigel'man et al. (1995)), where $\varepsilon_F =$ 1210 K (Rietvald et al., 1992) and $\Delta(T) \approx \Delta_o \left| 1-(T/T_c) \right|^{\alpha}$, and $\Delta_o \approx 5.2k_BT_c$ is the zero-temperature superconducting energy gap, empirically determined from low-temperature scanning tunneling spectroscopy (Wei et al., 1997) and corrected for d-wave pairing. The

exponent on the temperature dependent energy gap, α, equal 1/2 for the BCS gap function, and $\alpha = 2/3$ for the three-dimensional XY model (Salamon et al., 1993; and Jeandupeux et al., 1996). Clearly, since for a given angle, the Hall conductivity versus reduced temperature is universal among all of the samples, the τ will be the same for all samples. (In fact, the only difference among the samples is the small variation in T_c.) The transport time, τ, versus reduced temperature, $t = (T/T_c)$, for the applied magnetic field at 1, 2, and 4 Tesla, for $\alpha = 2/3$ is shown in figure 4-11(a). The transport time, τ, versus reduced temperature, $t = (T/T_c)$, for the applied magnetic field at 1, 2, and 4 Tesla, for $\alpha = 1/2$ is shown in figure 4-11(b). The magnitude of the range of $\tau \sim 10^{-13}$ seconds below T_c, to $\sim 10^{-14}$ seconds above T_c is consistent with quasiparticle scattering times derived from thermal conductivity (Krishana et al., 1995) microwave surface resistance (Bonn et al., 1993; Bonn et al., 1994), and optical transmission (Spielman, 1994) experiments. With this consistency one may consider associating the τ of the Feigel'man et al.(1995) model with the scattering of quasiparticle excitations.

The independence of σ_{xy} on the defect density and defect orientation, and when mass anisotropy is considered, the independence of σ_{xy} on the applied magnetic field orientation relative to the columnar defects, implies that the flux-flow mixed-state Hall conductivity is pinning independent. Again, this universal behavior of defect independent σ_{xy} among the various samples, the as-grown and those with correlated defects, is beyond the original expectation of Vinokur et al.(1993) developed for random point disorder. The defect-independent Hall conductivity appears valid even for correlated disorder in the flux-flow limit of the mixed state.

That τ is also independent of the defect density and defect orientation, a direct result of the independence of σ_{xy} on the same factors, and when mass anisotropy is considered, τ is independent of the applied magnetic field orientation relative to the columnar defects, and yet τ is clearly associated with the characteristic time of quasiparticles, implies that the quasiparticle scattering mechanism is independent of the static disorder. This can be examined theoretically by considering the relations among the vortex-column interaction time (equivalently considered as t_{pin}, the pinning interaction time), t_{col}, the vortex plastic deformation time, t_{pl}, the thermal fluctuation time, t_{th}, and the carrier transport time, τ.

Inhomogeneity in the vortex structure is required for pinning. Therefore, the inhomogeneity duration time, t_{pl}, must be longer than the pinning interaction time, t_{pin}, for pinning to be effective. In other works, vortices cannot be pinned if the following condition holds,

$$t_{pin} \gg t_{pl}.$$

Therefore, to pin the system, there must be an inhomogeneity duration time, t_{pl}, sufficiently longer than the vortex-pin interaction time, t_{pin},

$$t_{pl} \gg t_{pin}.$$

In a conventional liquid, the only inhomogeneity duration time, t_{pl}, is that due to thermal fluctuations. Therefore the conventional liquid cannot be pinned when

$$t_{pin} \gg t_{pl} \approx t_{th}.$$

In a highly viscous liquid, where pinning is effective, the inhomogeneity duration time, t_{pl}, is associated with its plastic deformation. The inhomogeneity caused by the plastic deformation of vortices in a viscous vortex-liquid cannot be relaxed thermally. That is,

$$t_{pl} \gg t_{th},$$

due to the large plastic energy barrier, U_{pl}, resulting in a long relaxation time, t_{pl}. Hence, for $U_{pl} \gg k_B T$ in a viscous liquid, pinning will occur for,

$$t_{pl} \gg t_{pin},$$

quite independently of t_{th}.

The vortex-column interaction time can be estimated by considering, $t_{col} \approx r_p/v_c$, where r_p is the pinning range of a columnar defect, given by $r_p \sim [\xi^2 + \langle u^2 \rangle_{th}]^{1/2}$, where $\langle u^2 \rangle_{th}^{1/2}$ is the root-mean-square of the thermal displacement of vortices, v_c is the vortex critical velocity, where $v_c = j_c \Phi_o/\eta$, and j_c is the critical current density, η is the viscosity, and Φ_o is the flux quantum. The temperature range of the experiments is above the

estimated "delocalization temperature", T_{dl}, which is estimated as 85 K for $YBa_2Cu_3O_7$, where the delocalization temperature corresponds to the temperature above which the root-mean-square of the thermal displacement of vortices, $\langle u^2 \rangle_{th}^{1/2}$, becomes comparable to the average separation of the columnar defects, d_{col} (Blatter et al., 1994). $\varepsilon^{-2} \equiv M_c/m_{ab}$, $\varepsilon_o \equiv [\Phi_o/4\pi\lambda]^2$, λ is the magnetic penetration depth, r_{col} is the radius of the columnar defects, k_B is the Boltzmann constant, j_o is the depairing current density, and $\eta = \Phi_o H_{c2}/\rho_n c,$. ρ_n is the normal state resistivity at T_c, and the upper critical field is $H_{c2} = \Phi_o/2\pi\xi^2$.

Estimating the various characteristic times for the mixed state Hall effect in the presence of columnar defects (Beam et al., 1997), following the development of Blatter et al. (1994),

$$t_{col} \approx \frac{r_p}{v_c} = \frac{r_p H_{c2}}{j_c \rho_n} = \frac{r_p \Phi_o / (2\pi\xi^2)}{j_c \rho_n}, \quad \text{where}$$

$$r_p \sim \left[\xi^2 + \left\langle u^2 \right\rangle_{th}\right]^{1/2}, \quad \left\langle u^2 \right\rangle_{th}^{1/2} \approx d_{col}\left[\frac{k_B T}{\varepsilon\varepsilon_o r_{col} / \pi \ln(d_r^2 / 2\xi^2)}\right]^2, \text{ and}$$

$$j_c(T > T_{dl}) \approx \left(\frac{\xi r_{col}^2}{2d_{col}^3}\right)^3 \left[\frac{\varepsilon\varepsilon_o r_{col} / \pi \ln(d_r^2 / 2\xi^2)}{k_B T}\right]^4 j_o, \quad \text{with} \quad j_o \equiv 4\varepsilon_o / (3\sqrt{3}\xi\Phi_o).$$

Using the experimental parameters of $B = B_\phi = 2$ Tesla and $T/T_c = 0.98$, and the material parameters for $YBa_2Cu_3O_7$ single crystals: $\xi(0) = 1.2$ nm, $\lambda(0) = 140$ nm, $T_c \approx$ 93 K, $r_{col} = 35$ nm, $\rho_n = 6\text{x}10^{-7}\ \Omega$ m, and $\varepsilon^{-2} = 60$ (Beck et al., 1992; Blatter et al., 1994), we obtain (Beam et al., 1997)

$j_c \approx 5 \times 10^3$ A/m^2 ,

and

$t_{col} \approx 5 \times 10^{-5}$ seconds.

$t_{th} \approx 2 \times 10^{-11}$ seconds, from $t_{th} = 8\kappa^2 a_o^2/\rho_n$ where $\kappa \equiv \lambda/\xi$ is the Ginzburg-Landau parameter, and $a_o \equiv 1.075(\phi_o/B)^{1/2}$ is the Abrikosov lattice constant, and H = 2 Tesla.

$t_{pl} \sim 4 \times 10^{-11}$ seconds, from $t_{pl} \approx t_{th}\exp[U_{pl}/k_B T]$, where $U_{pl} \approx (r_{col}/2\xi)^2 \varepsilon_o a_o$ is the plastic barrier for vortices in the presence of columnar defects and for applied magnetic fields aligned with the columnar defects, and $U_{pl} \sim 30$ K at T = 0.98T

and

$\tau \sim 10^{-13}$ seconds.

From the above, it is clear that the system is in a conventional liquid state (flux flow), and defect independence should be observed, as

$t_{pin} = t_{col} \gg t_{pl}$.

Furthermore, it is evident that the mechanism which gives rise to quasiparticle scattering in the vortex-liquid state cannot be relaxed by thermal effects, since,

$$t_{th} \gg \tau.$$

Finally, the above estimates of different characteristic times suggest that the quasiparticle scattering mechanism of the mixed-state Hall conductivity is not directly related to either the thermal fluctuations of vortices or the vortex-column interaction, since

$$t_{pin} = t_{col} \gg t_{pl} \approx t_{th} \gg \tau.$$

These estimates are therefore consistent with our experimental observations.

Summary of DC Hall Effect Experiment

In summary, this investigation of the vortex-state Hall conductivity leads to the following conclusions. The vortex-state Hall conductivity of $YBa_2Cu_3O_7$ single crystals is universal, independent of the density and orientation of correlated disorder for a given reduced temperature, magnetic field strength and orientation of the magnetic field relative to the sample c-axis. Additionally, the angular dependence of the vortex-state Hall conductivity is entirely determined by the mass anisotropy.

It can be inferred that the transport scattering time, τ, derived using the Feigel'man et al. (1995) model of Hall conductivity is related to quasiparticle scattering time since the

magnitude of τ is comparable with the magnitudes of quasiparticle scattering times derived from other experimental techniques.

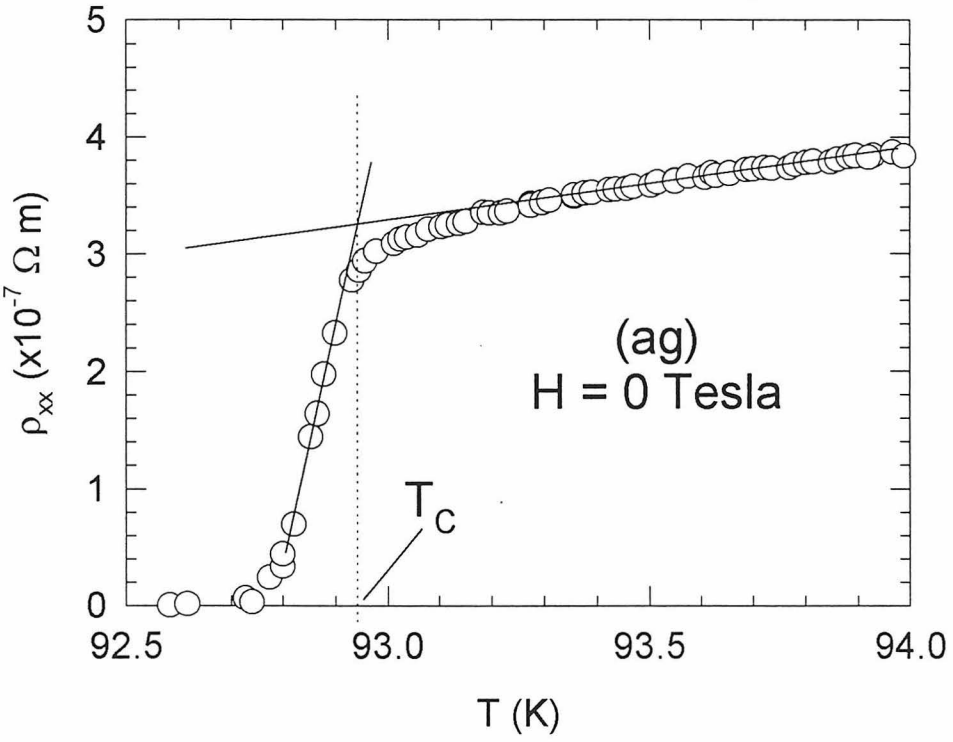

Figure 4-1 Geometric construction for the determination of T_c

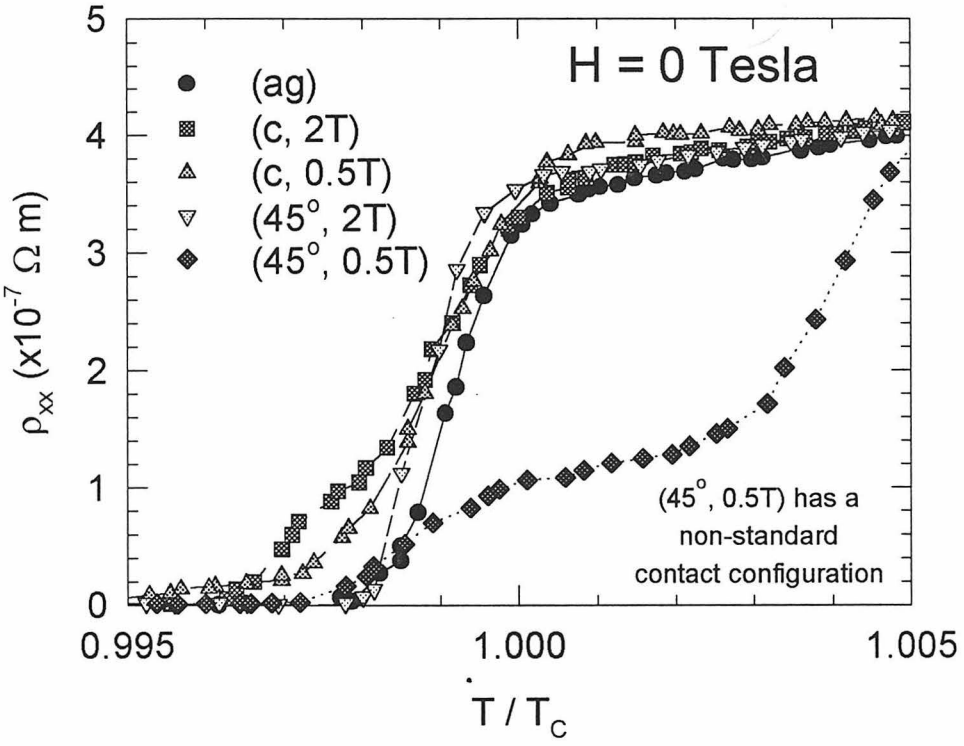

Figure 4-2 Comparison of zero-field resistive transitions

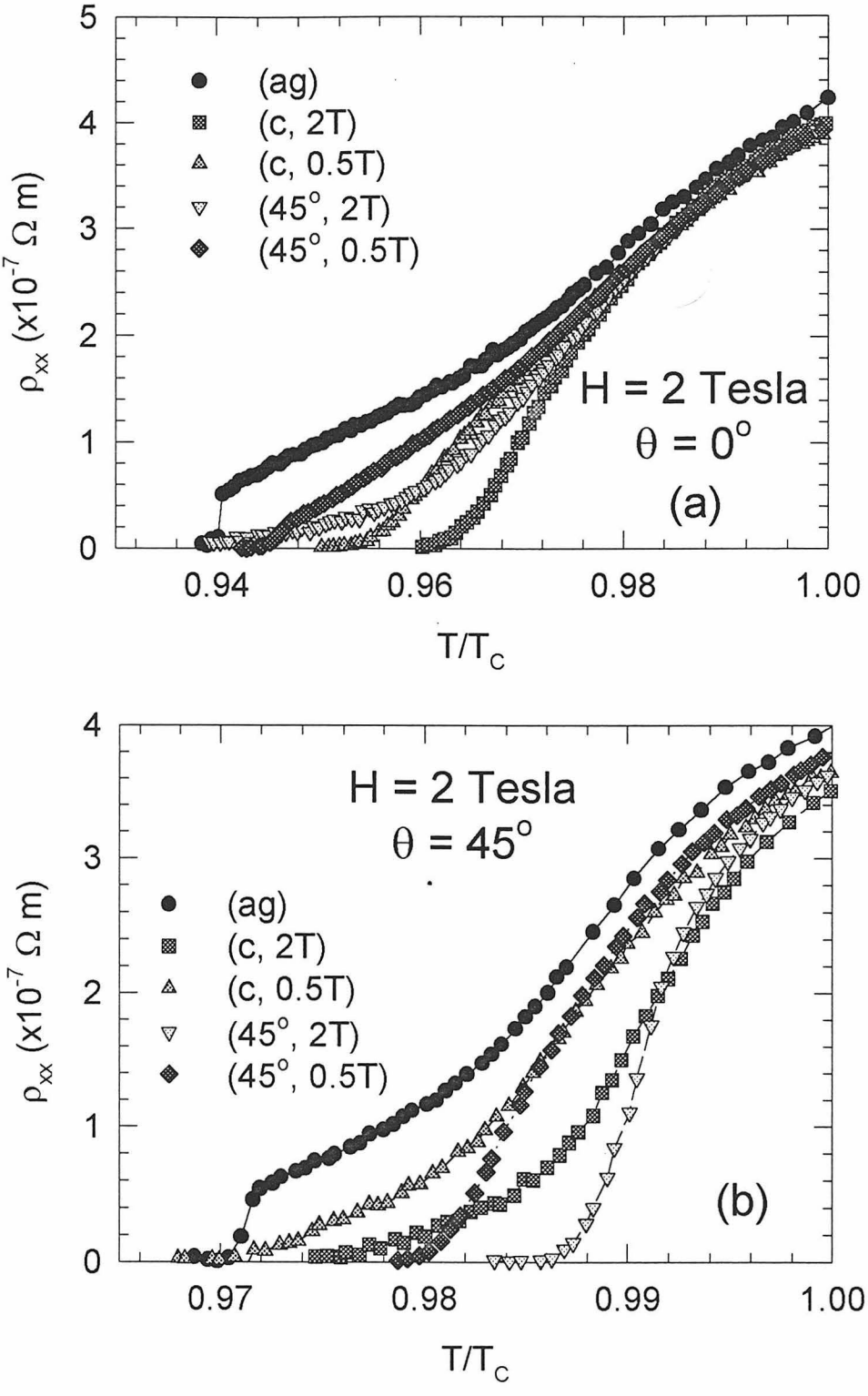

Figure 4-3 Effect of field alignment with columnar defects on the longitudinal resistivity of five $YBa_2Cu_3O_7$ single crystals

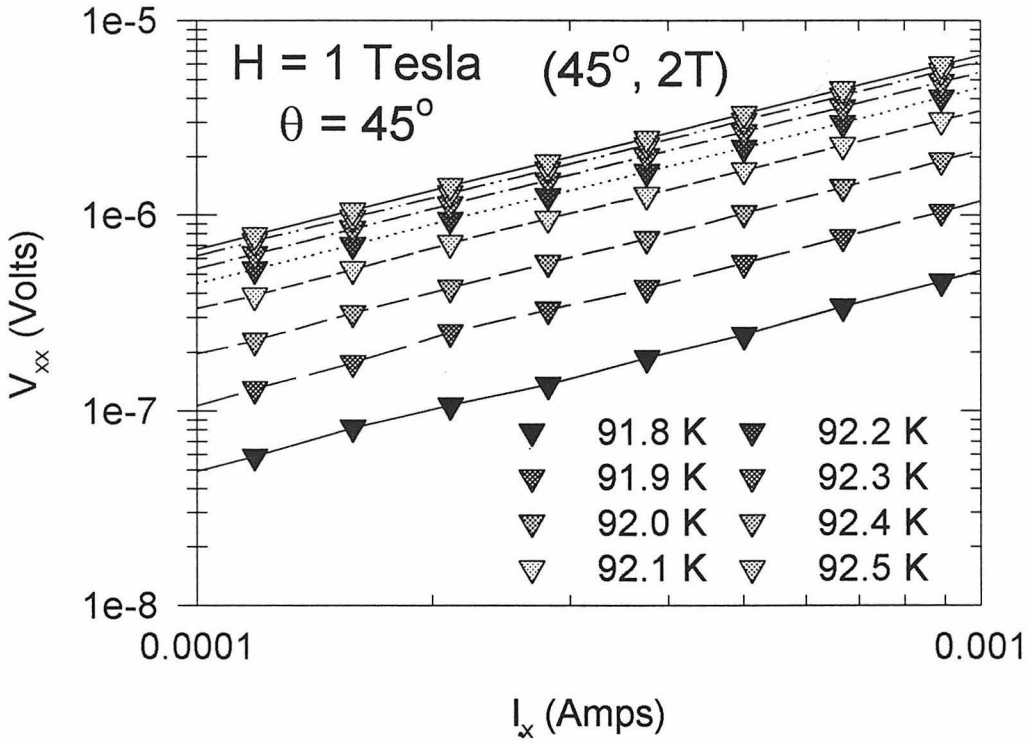

Figure 4-4 Current - voltage isotherms for (45°, 2T) at H = 1 Tesla, θ = 45°

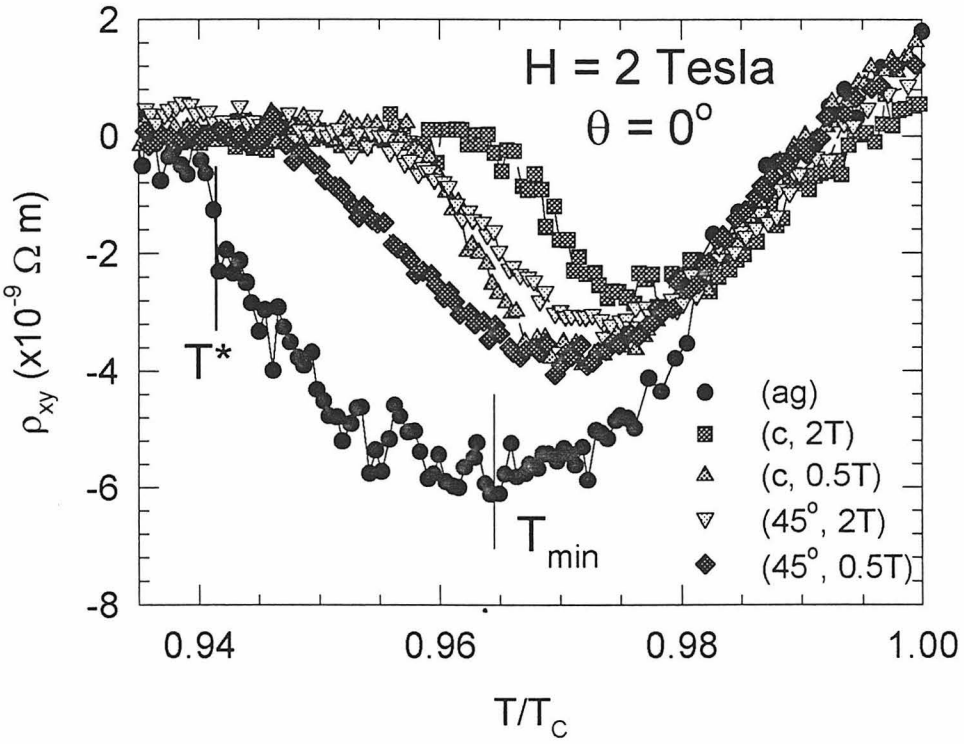

Figure 4-5 Effect of columnar defects on Hall resistivity for five $YBa_2Cu_3O_7$ single crystals. H = 2 Tesla, $\theta = 0^o$

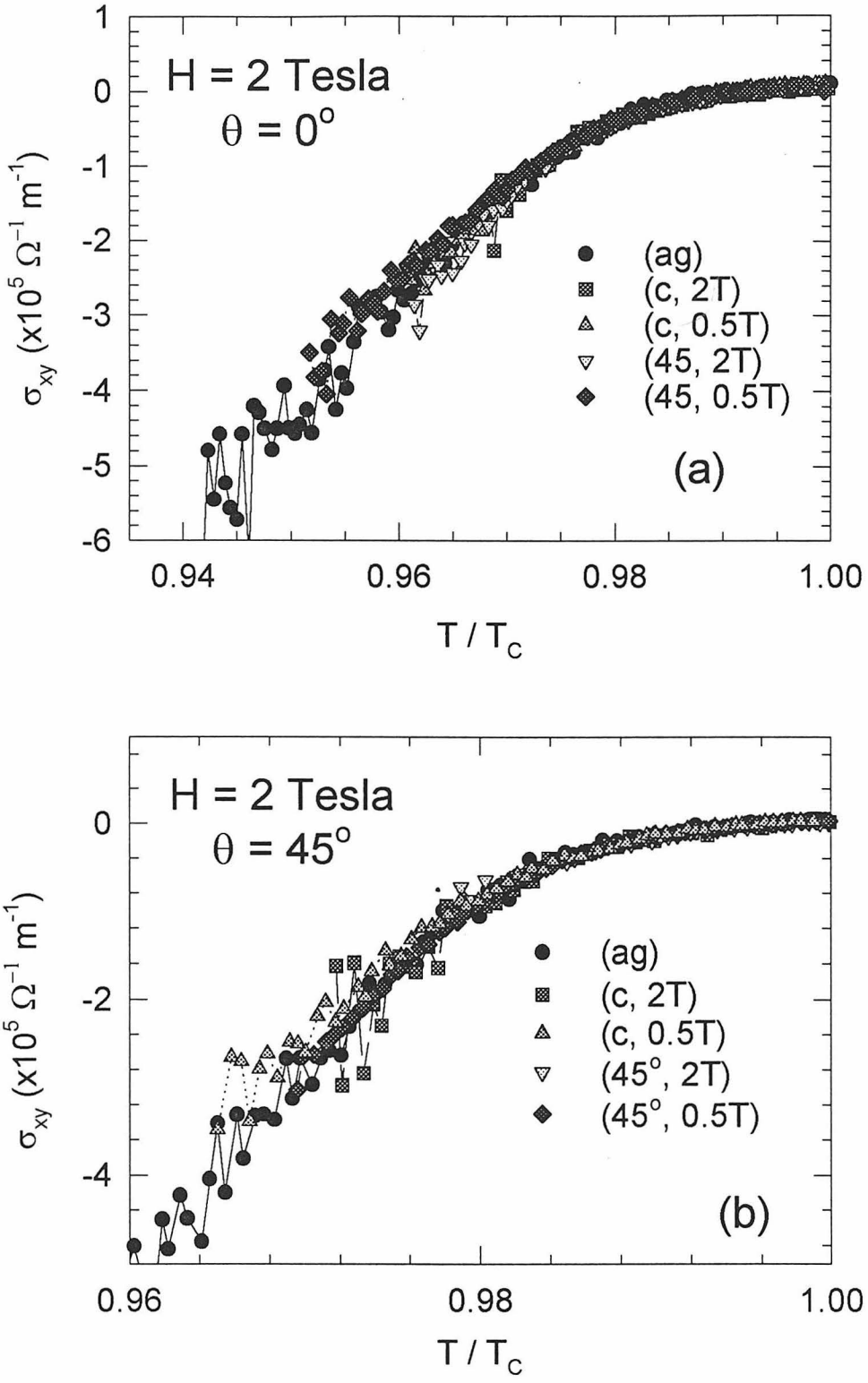

Figure 4-6 Universality of Hall conductivity for five $YBa_2Cu_3O_7$ single crystals

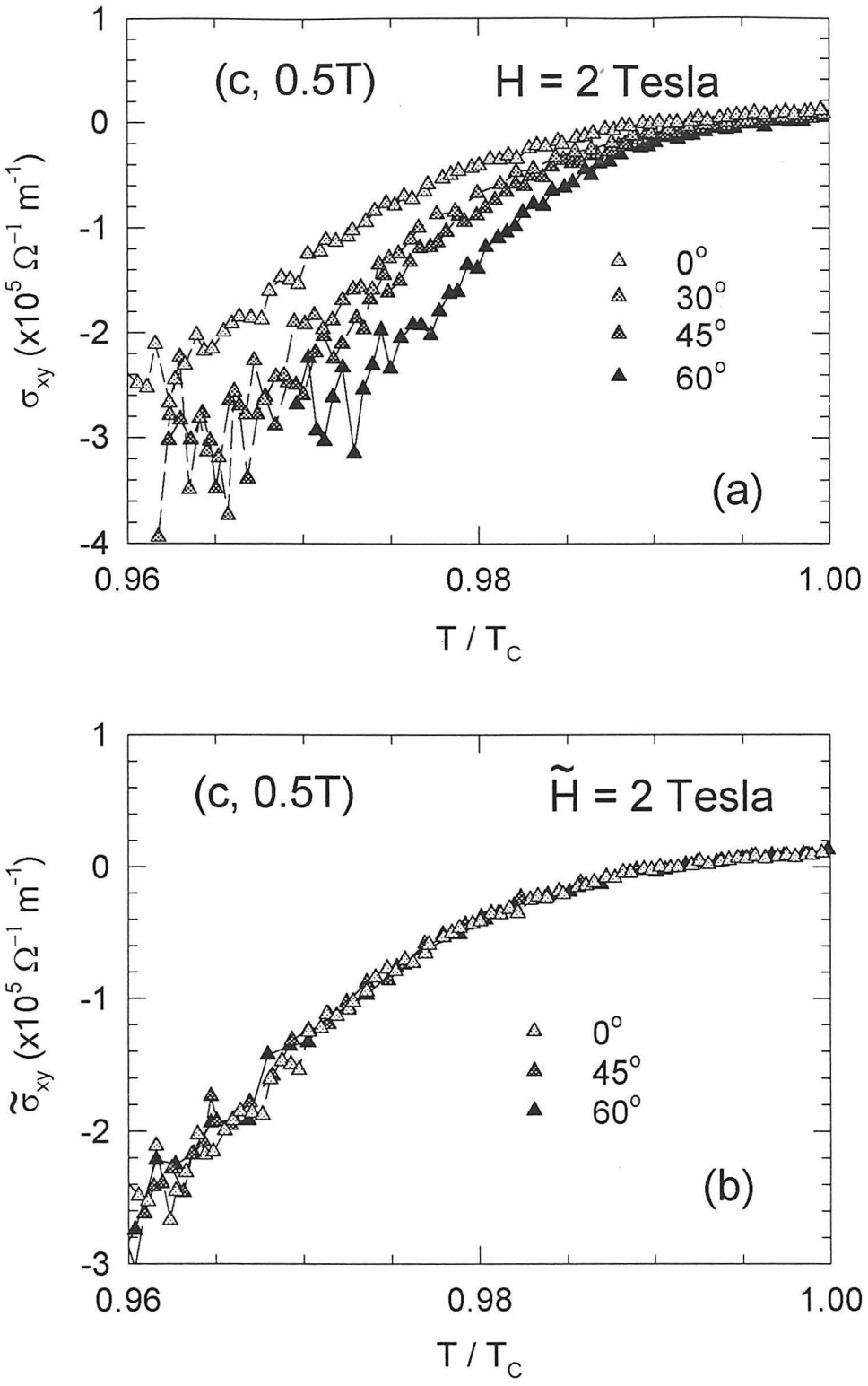

Figure 4-7 Hall conductivity vs T / TC of (c, 0.5T) at various angles and (a) H = 2 Tesla, (b) $\tilde{H}$ = 2 Tesla

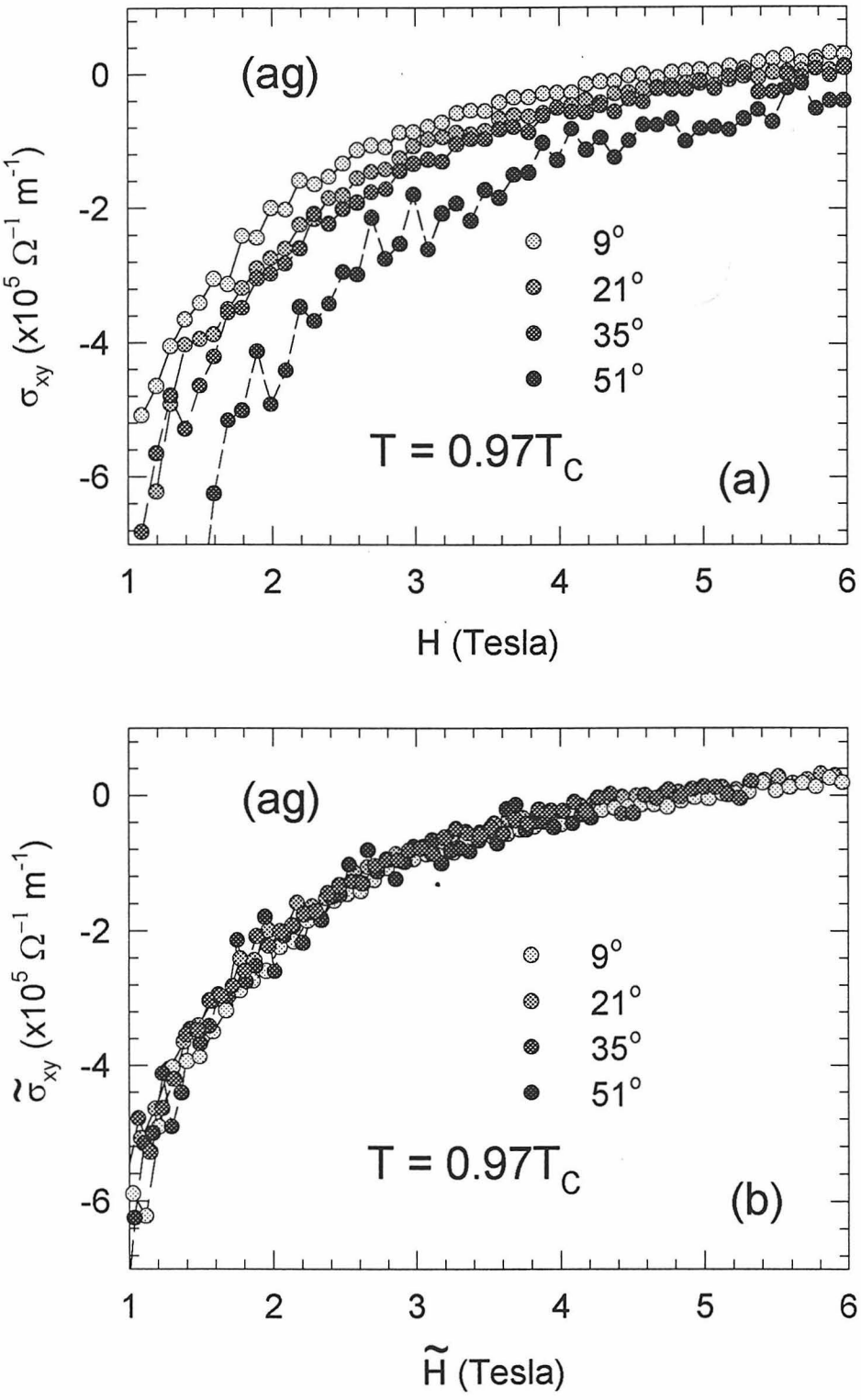

Figure 4-8 Hall conductivity of (ag) at various angles (a) versus H, (b) versus $\tilde{H}$

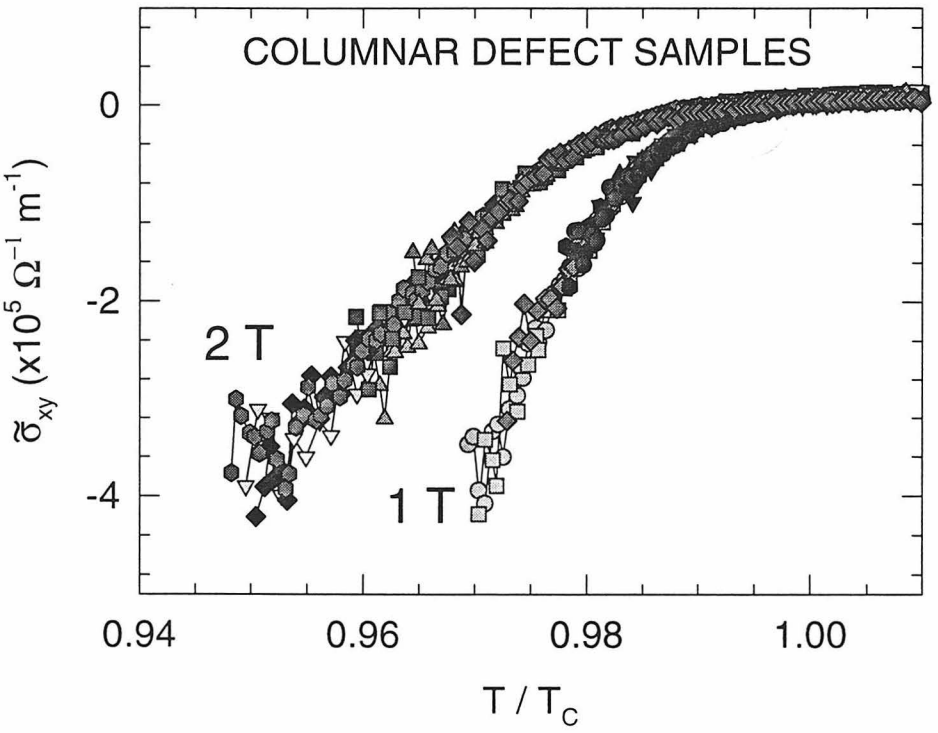

Figure 4-9 Universal scaled Hall conductivity of columnar defect samples at (H, θ) = (4T, 60°) and (2T, 0°), leftmost curves, and (H, θ) = (2T, 60°) and (1T, 0°), rightmost curves

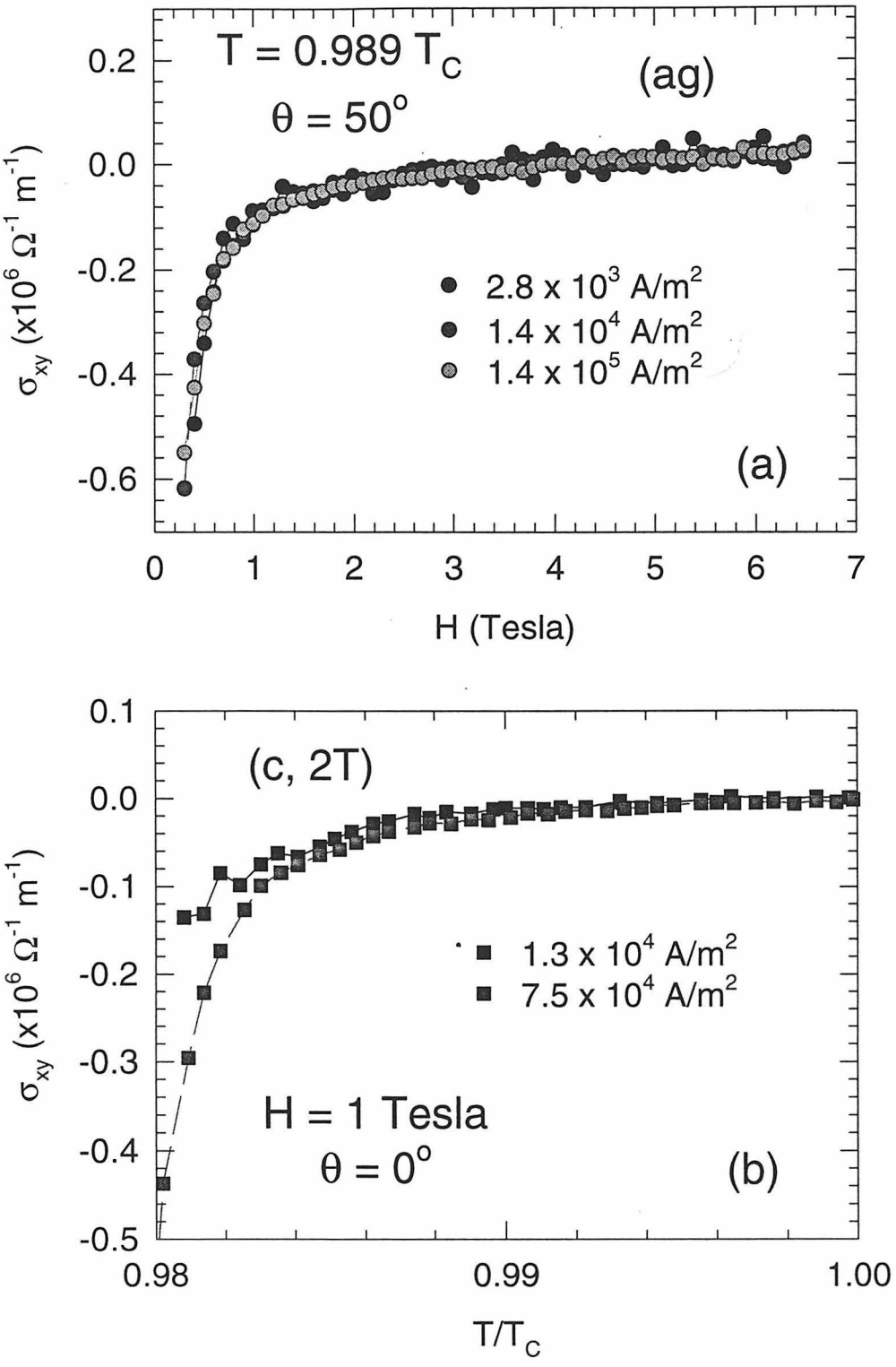

Figure 4-10 Current density independence of Hall conductivity (a) versus field for (ag), (b) versus T/T_C for (c, 2T)

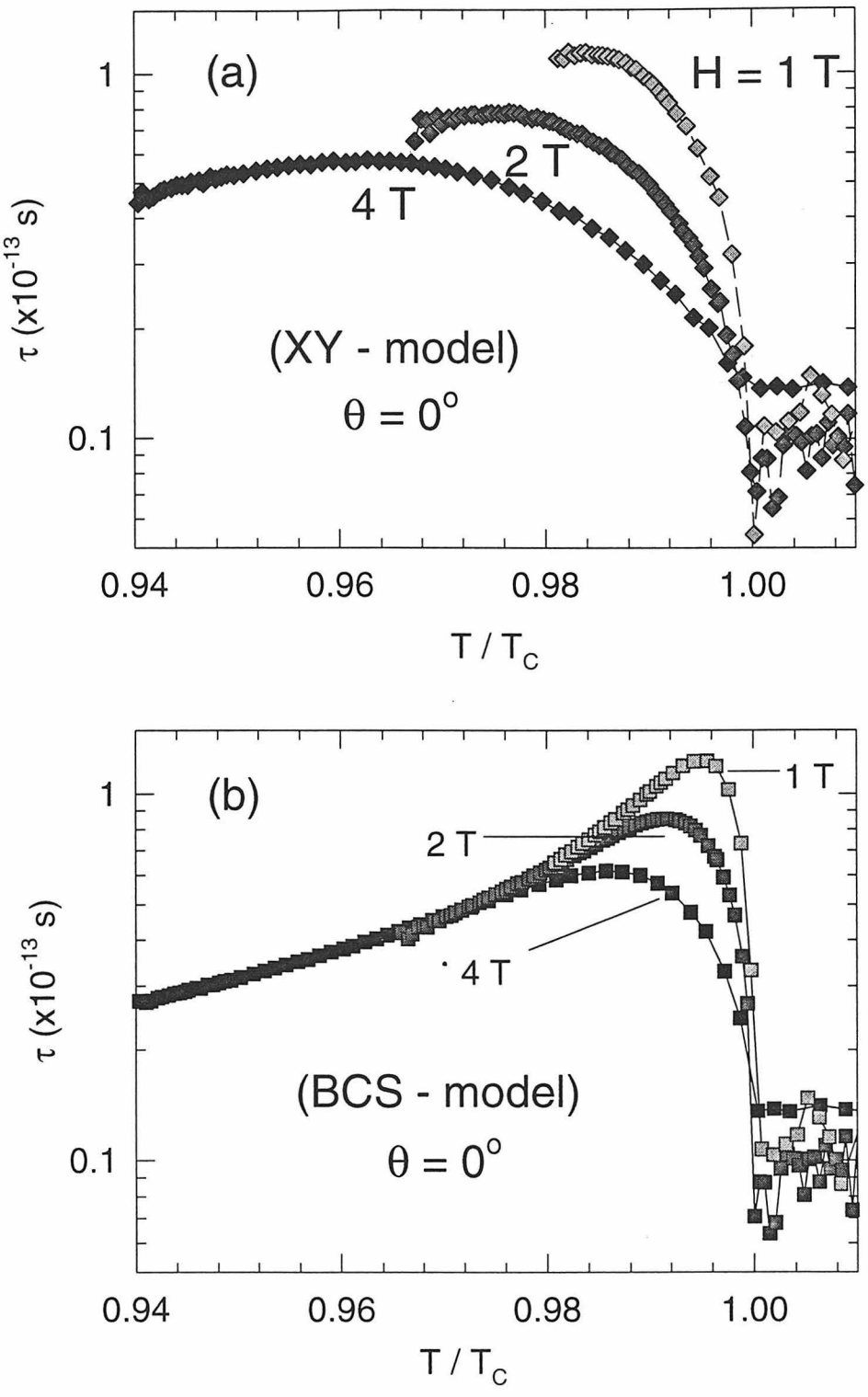

Figure 4-11 τ versus T/T_C data of $YBa_2Cu_3O_7$ single crystals for H = 1, 2, and 4 Tesla, $\theta = 0^\circ$ using (a) the XY - model, and (b) the BCS - model

Chapter Five: AC (Alternating Current) Transport Measurements

This chapter references a new technique used to measure the voltages on the order of 10^{-6} to 10^{-9} Volts, in order to resolve the longitudinal and Hall resistivities of a $YBa_2Cu_3O_7$ thin film from the onset of dissipation below T_c, into the normal state above T_c.

Background

There have been few alternating current (AC) transport measurement studies of superconductors in the frequency range of 100 to 10^7 Hz, and to this author's knowledge, there have been no AC Hall effect transport measurement experiments conducted in this frequency range. This is due in part to the difficulties in conducting the measurements, as noises and losses are high, equipment is not commercially available, and calibrations are difficult. Works at other frequencies, for example optical and microwave, do not directly relate to work in this frequency range and have been discussed in Chapter 2.

There are several AC longitudinal impedance measurements reported in the literature (Yeh et al., 1992; Yeh et al., 1993; Reed et al., 1993; Jiang et al., 1994; and Olsson et al., 1991). These experiments focused on critical analysis of the phase transition between the vortex-solid phase and the vortex-liquid phase. The work of Olsson et al.(1991) evaluated critical exponents, but only at one magnetic

field and over a narrow range of frequencies. The other works considered the critical exponents over a larger range of frequencies, and over a broad range of magnetic fields, orientations of the magnetic field, and verified the universality of critical scaling by comparing the AC result with DC E-versus-J measurements (Yeh et al., 1993; Reed et al., 1993). The technique was also applied to validate that columnar defects in single crystals resulted in a different universality class of the vortex phase transition (Jiang et al., 1994). Additional work in this frequency range used a differential susceptibility probe and obtained critical scaling of the magnetic susceptibility near the vortex-solid to vortex-liquid phase transition with exponents in agreement with the AC and DC transport results (Reed et al., 1994).

The AC longitudinal impedance technique used above is best described in the thesis by Reed (1995). As the AC Hall experiment uses some of the equipment and setup used in the AC longitudinal impedance measurements, reference will be made below to the applicable parts of the thesis of Reed (1995). Directly applicable is that the AC longitudinal impedance showed no frequency dependence far from the vortex-solid to vortex-liquid phase transition.

System Setup

Two components, the longitudinal impedance and Hall impedance, are necessary to obtain the Hall conductivity. Although these components are straightforwardly obtained in DC measurements, by simply switching among the

electrical contacts to the given sample, obtaining the AC longitudinal and Hall resistivities over a broad frequency range is challenging. The desired components are nested within other system noises and losses, and different approaches are required to obtain each component, as the desired components, longitudinal impedance and Hall impedance, respond differently to the reversal of magnetic field direction.

AC Longitudinal Impedance

The longitudinal component of impedance is independent of the reversal of the applied magnetic field, as long as the applied magnetic field is always perpendicular to the direction of the applied current. Furthermore, with careful calibration, all background noises, phase shifts and gains can be taken into account. Only instrument measurement errors are not correctable by calibration, but if the errors are constant, such as the range resistor step errors discussed by Reed (1995), independent of whether the samples voltage contacts are high or low, the errors can be eliminated by, reversing the polarity of the electrical contact, using a switch.

The system schematic for the AC longitudinal impedance experiment is shown in figure 5-1 (compare with figure 5-2 of Reed (1995)). Changes to the setup by Reed include an improved differential amplifier with lower noise and higher gain, connecting the low potential (L_p) input of the HP 4194A directly to

the sample and to the low side of the differential amplifier, reducing the effective cable length, and improved cabling (QMI - Quality Microwave Interconnects, Inc., Workhorse, and PSelect Pen-Flex 0.141 cables) which yielded smaller losses and reduced noise. The measurement limitation in the setup used by Reed was the preamplifier. (Reed claimed linearity of the preamplifier to approximately 2 MHz.) The limitation of the setup used in the present work is the HP 4194A and its use of an auto balancing bridge, combined with the necessity to have system cable length (between the HP 4194A and the DUT - device under test) greater than zero. Each of these aspects will be discussed in detail below.

AC Hall Impedance

As mentioned above, the challenge of determining the AC Hall conductivity is that of obtaining the AC Hall impedance. The Hall electric field is a vector component which reverses direction upon reversal of the applied magnetic field, with all else remaining the same. All other background, phase shifts, and gains are independent of field reversal, and constant instrument errors (again, such as the range resistor step mentioned by Reed (1995)) are also field direction independent. Therefore, no switch for reversing the polarity of the contacts is necessary in the AC Hall impedance setup, as the field reversal effectively provides the same function as the switch used in the longitudinal impedance setup. A system schematic of the AC Hall impedance experiment is shown in figure 5-2.

The measuring equipment needs a large dynamic voltage range accurately covering 5 or 6 orders of magnitude, and resolution to one part in 10^3 to 10^4 of the input signal. This is required, as it is necessary to resolve signals accurately from inputs signal strengths two to four orders of magnitude higher, and over a range of two to four orders of magnitude. Furthermore, the ideal equipment setup allows for true four-point measurements, with input currents and current contacts independent of input voltages and voltage contacts. The only coupling between current and voltage should be via phase locking. Any other arrangements, such as four-terminal pairs and auto balancing bridges will at best require excessive calibrations, and at higher frequencies may simply be invalid. Furthermore, the auto balancing bridge is limited by cable length compensation. Equipment with auto balancing bridges allow for some compensation of cable length (0 meters and 1 meter on most, and 2 meters of cable length on some), for precisely measured distances between measuring box and device under test. If the cable lengths are not precise, or are longer than the compensation setting, the equipment will produce measured values that are compensated for an incorrect length, resulting in errors at high frequencies. The compensation for the errors resulting from the use of an auto balancing bridge at high frequencies and at cable lengths longer than the instrument available compensation length is newly developed in this work. Clearly, there is no calibration for an unbalanced bridge.

HP 4194A

The HP 4194A Impedance/Gain-Phase Analyzer does not have the desired characteristics of measuring equipment for this experiment. It uses an auto balancing bridge, is designed for four-point measurements from devices with two ports (that is, two electrical contacts), provides cable length compensation for cables of zero meters or one meters in length, and is easily overdriven as it has a maximum input of one volt. Any input potential greater than one volt between the high and low potentials of the HP 4194A yielded erroneous output values of the impedance (empirically verified using a noninductive resistor). (The HP 4194A derives impedance from measured voltage and current). Furthermore, the impedance range has a minimum of 10^{-4} Ω.

The longitudinal (and diagonal) voltage (as defined in chapter 3) of the large thin film used in the AC Hall experiment was on the order of 10^{-3} Volts for currents in the range of 1 mA, near T_c and above, corresponding in a resistance on the order of 1 Ω, when measured using the DC setup (see chapter 3). Below T_c, using the same DC setup, the longitudinal (and diagonal) voltage of the same thin film varied on the order of 10^{-6} Volts to 10^{-3} Volts, corresponding to a resistance on the order of 10^{-3} Ohms to 1 Ohm. To obtain the Hall signal from the measured diagonal voltage, resolution of two to three orders of magnitudes better than the measured diagonal voltage is required. Using the HP 4194A to measure the impedance of the thin film requires the use of preamplification, as the actual Hall signal is often only on the order of the 10^{-4} Ohms minimum of the impedance measurement range of the HP 4194A.

To stay away from the one volt input signal limit, the maximum gain possible for use in the AC setup was 40-47 dB. This combined with a minimum sensitivity of 10^{-4} Ω for the HP meant that in order to resolve the Hall signal, the minimum gain needed to be about 40 dB. The Hall voltage varied linearly with applied current, over the temperature and applied magnetic field regime examined in this work. Furthermore, the noise increased as the applied current decreased. Consequently, the optimum applied current for the AC Hall effect measurements, based on the above considerations, was 1 mA. This resulted in resolved AC Hall measurements signal levels on the order of 10^{-3} Volts (~ 10^{-5} Volts before amplification).

Some other specifications of the HP 4194A Impedance/Gain-Phase Analyzer are as follows.

Output Signal Frequency:	100 Hz to 40 MHz, depending on cable length and compensation setting, 1 mHz resolution
Output Signal Level:	10 mV to 1 Vrms
Impedance Measurement Range:	0.1 mΩ to 1.6 MΩ

Measurement Accuracy: 0.17% of reading

The HP 4194A uses an auto balancing bridge (see Auto balancing Bridge below) to maintain zero potential at the low potential terminal (L_p). Effectively, range resistors are used such that the range resistor current is balanced with the DUT current to obtain the zero potential. The use of the auto balancing bridge results in a decrease in the usable frequency range with increasing cabling length (see Cable Length and Compensation below).

Preamplification

Longitudinal measurements were made by Reed (1995) using 62 dB of preamplification in two stages. Reed's first stage was an originally designed low noise differential amplifier (of about a 22 dB gain and a linear gain bandwidth of about DC to 2 MHz). The 22 dB differential amplifier was connected with its output in series with a commercially obtained (Analog Modules 322-10-B-200) low noise linear amplifier (of 40 dB gain and a bandwidth of 100 Hz to 100 MHz). The end-to-end bandwidth of the preamplifier was limited by the Linear Technologies 1028 ultra-low noise op amps which are linear in output up to ~ 2 MHz.

Although Linear Technologies 1028 ultra-low noise op amps were used in the differential amplifier, the differential amplifier design by Reed (1995) was not optimized for low noise. Two major drawbacks of the differential amplifier design were that variable resistors were used, and that they were placed at the early stages of the differential amplifier. Possibly more significant problems in the end to end design is that the output of the differential amplifier was not impedance matched to the 50Ω connecting cable, nor was the input of the Analog Modules linear amplifier, with a 150 to 250Ω input impedance matched to the connecting cable. These inefficiencies contributed significantly to noise and harmonic distortion of the end-to-end system.

The present setup uses an originally designed 42 dB gain differential amplifier for the total preamplification. The schematic and the printed circuit board layout are shown in figures 5-3(a) and (b), respectively. Note that the 50 Ohm resistors to ground at the inputs of the differential amplifier, available for impedance matching, were not used because we wanted to take advantage of the high input impedance (6 kΩ) of the CLC-425 operational amplifiers. As discussed by Reed (1995), minimizing the effects of the impedance of the sample contacts (~ 1 Ohm),

$$V_{MEASURED} = V_{ACTUAL}/(1+(Z_{CONTACT}/Z_{AMPLIFIER}),$$

and

$V_{MEASURED} \approx V_{ACTUAL}$ if $Z_{CONTACT} \ll Z_{AMPLIFIER}$.

The end-to-end noise level of the 42 dB differential amplifier was significantly less (by a factor of 2-4) than that of the 22 dB initial stage amplifier used by Reed (1995). (The noise levels were compared using the gain-phase side of the HP 4194A from 10 Hz to 100 MHz. The noise levels were obtained using either input channel with the other input terminated. The noise level of the 42 dB gain amplifier was comparable with the noise level of the commercially obtained Analog Modules 322-10-B-200.) Additionally, the gain of the 42 dB differential amplifier is linear constant to within a dB from 10 Hz to about 30 MHz, with a 3 dB bandwidth of 110 MHz, and shows no distortion across the entire bandwidth at output signal levels up to three orders of magnitude above those necessary for this experiment. (The gain of the 22 dB differential amplifier by Reed (1995) was approximately constant to about 2 MHz.) The 42 dB differential amplifier uses Comlinear Corporation CLC-425 ultra-low-noise op amps, with a gain-bandwidth product of 1.9 GHz, 1.05 nV/$\sqrt{\text{Hz}}$ equivalent input voltage noise, and an input impedance of 6 kΩ. All other inputs and outputs were impedance matched to capitalize on the low noise properties of the op amps. Additionally, batteries were used to power the CLC-425 op amps, further reducing the noise. (Reed (1995) used a rectified power supply in close proximity to the 22 dB differential amplifier

and the Analog Modules linear amplifier, allowing the possibility of additional noise.)

Load Resistor

A non-inductive load resistor, R_L, was used to provide a nearly constant current amplitude for the measurements, since, for sample impedance, $Z_{DUT} \ll R_L$, the output current, $I_{AC} = V_{AC} / (Z_{DUT} + R_L) \approx V_{AC} / R_L$. (Additionally, the load resistor constrains the measurement current to be in the linear response regime. Both the current and voltage are continuously measured by the HP 4194A, from which the impedance is determined. Constant current is not a requirement of the impedance determination, but is required to ensure that the measurements are made in the linear current-voltage response regime.) The HP 4194A outputs the test signal as a voltage through the high current port, H_C.

A resistance of $R_L = 1\ k\Omega$ was selected to maintain a constant current of 1 mA for an HP 4194A output test signal voltage of 1V. The current-voltage relationship was measured to determine that the sample was in the linear response regime when the applied current was on the order of 1 mA.

Wiring

The four-terminal pair (4TP) configuration (Honda, 1989) was used to isolate voltage sensing cables for the input current cables. This configuration used with the HP 4194A allows for measurement down to the 10^{-4} - 10^{-3} V range before preamplification. It is crucial to connect this correctly, as improper connection reduces the sensitivity, and the available frequency range. For example, if the outer conductors of the coaxial cables are not shorted together near the sample, the available measurement range for this setup is reduced to 2 MHz (empirically determined for this setup). Beyond 2 MHz , the auto balancing bridge is unlocked, and large measurement errors are produced. The 2 MHz limit was observed upon separating the outer conductors of the input current cables from the outer conductors of the voltage sensing cables. Although the latter seems logically correct for reduced noise on the voltage sensing cables, it is incorrect for the HP 4194A. The HP 4194A is not designed to make four point measurements as in the DC setup. Rather, the HP 4194A is designed to make-four point measurements of devices under test (DUTs) that have only two electrical contacts, using separate current and voltage paths for each contact as is shown below in Fig 5-3. Consequently, using the HP 4194A where the sample has four contacts (four ports) requires careful calibrations discussed below. Even then, the results may have reduced accuracy and resolution.

Auto Balancing Bridge

Auto Balancing Bridges are used to provide high accuracy over broad ranges of impedances and frequency. The limitation of the use of the auto balancing bridge is the time required for signal propagation, which thereby results in a limitation of the usable upper frequency. A simplified functional diagram of the auto balancing bridge is shown in figure 2-4 of Honda (1989) and reproduced in figure 5-4. The auto balancing bridge detects with detector D the potential at the low terminal (L_P) and balances, with D controlling the amplitude and phase of oscillator 2 (OSC2), the current through the DUT with the current through the range resistor (R_r), such that the potential at the low terminal (L_p) is zero. This operation works automatically as long as the feedback between the detector D and the OSC2 can be accomplished within one period.

Cable Length Limitations

Although the 4TP is the best configuration for the HP 4194A, the length of cables between the HP and the DUT used in the system setup limits the upper frequency available for measurement. The system provides automatic compensation for HP test set cables of lengths of zero meters and one meters. The cable length of zero meters allows the full range of the impedance analyzer to be used (100 Hz to 40 MHz). The cable length of one meter limits the maximum usable frequency to 15 MHz. This is because the increased cable length requires

additional propagation time, and the auto balancing bridge will not be able to detect low potential signal in sufficient time at the higher frequencies. The rule of thumb for using HP supplied coaxial cables is

$$f \times L \leq 15,$$

where f is the frequency in MHz, and L is the cable length in meters (Honda, 1989). The setup used in this experiment has an average cable length of approximately 3 meters, and consequently should be limited to an upper frequency of 5 MHz. During measurement, it was observed that the bridge would temporarily unbalance at 7 MHz for a small range in increasing frequency and continuously from beyond 11 MHz. That the bridge first unbalanced at 7 MHz, instead of 5 MHz as expected by the rule of thumb, can be accounted for by variances in internal cable lengths of the HP 4194A and because an approximate average cable length was used in the rule of thumb calculation (predicted for setups with equal cable lengths), whereas the present setups have different cable lengths for each port. (Upon examining the measured data, the data at about 5 MHz for all measurement conditions appears erroneous, even though the bridge did not indicate unbalance during the measurements, and the data at frequencies just above and below the 5 MHz point in frequency appear valid.) The majority of the data beyond about 7 MHz was unusable.

Cable Length Compensation

As mentioned above, the HP 4194A offers compensation for cable lengths of zero meters and one meter (one meter cable length compensation corresponding the a calibrated closed path cable length of two meters in addition to the extent of the device under test). Cable lengths longer than one meter (closed paths greater than two meters) will cause phase errors, as the uncompensated cable length (additional closed path length beyond two meters) requires additional travel time. Active devices, such as differential amplifiers, add frequency-dependent phase delay, which can be equated to an effective additional path length. The phase change will be

$$\Delta\phi = 2\pi\Delta lf/v,$$

where Δl is the total uncompensated (additional) closed path length including phase delay or equivalent path length due to active devices, f is the frequency at which the measurement is taken, and v is the speed of wave propagation (on the average, that through the coaxial cables).

The total closed path length at issue is that of the voltage loop. The total path length for the voltage loop, including the effective length of the differential amplifier, 0.88 meters, is 5.92 meters for the AC longitudinal setup, and 5.62 meters for the AC Hall setup. Compensation for two meters of the total path length occurs when the cable length setting is at one meter. This leaves 3.92

meters of uncompensated cable length for the AC longitudinal setup, and 3.62 meters of uncompensated cable length for the AC Hall setup. The effective length of the differential amplifier was determined from S_{21} measurements of the differential amplifier (measured at Comlinear Corporation, Ft Collins, Colorado). The measured phase shift of the differential amplifier as a function of frequency is 1.5° phase delay per megahertz. Substituting this phase shift into the phase shift equation and setting the wave propagation speed to be equal to that in the coaxial cables yields the 0.88 meters effective length.

The speed of wave propagation, v, is related to the permittivity of free space, ε_o, the permeability of free space, μ_o, the relative effective dielectric constant, K, and the speed of light in a vacuum, c, such that,

$$v = (\varepsilon_o \mu_o K)^{-1/2} = K^{-1/2} c.$$

Teflon (polytetrafluoroethylene) is typically used as the dielectric in coaxial cables, and has a relative effective dielectric constant, K = 2.1 (Nayfeh and Brussel, page 140, 1985). Polyethylene is often otherwise used, with a relative effective dielectric constant, K = 2.25. Of concern in a calculation of phase delay is the frequency dependence of the relative effective dielectric constant. Von Hipple reported no frequency dependence of the relative effective dielectric constant measured at various points between 100 Hz and 3 GHz (von Hipple, page 332, 1954). Similarly, von Hipple reported no frequency dependence for polyethylene

(frequency independent to 10 MHz, and a datum at 3 GHz of the same frequency independent value) (von Hipple, page 327, 1954). For a given real impedance value, Z_{REAL}, the HP 4194A will erroneously output phase shifted values of Z_{REAL} * $\cos(\Delta\phi)$ for Z_{REAL}, and Z_{IMAG} * $\sin(\Delta\phi)$ for Z_{IMAG}. Although this is of concern, it is easily compensated by a rotation of the impedance complex plane.

Of greater concern is the effect of propagation delays on the operation of the auto balancing bridge. Errors in the measured impedance may be introduced by the auto balancing bridge if the feedback between the detector detecting the potential of the low potential terminal (L_P) and the oscillator the detector controls takes longer than one period to accomplish. At best, this will cause a bridge unbalanced condition, in which case it is obvious to disregard the data. More insidious is the indication of valid data, but improperly compensated. For this latter case, assumptions must be made as to the validity of the data and the possible magnitude of errors. The possible errors will be most evident at frequencies near and greater than 5 MHz.

Experiment

The AC Hall conductivity studies were conducted using a fully oxygenated $YBa_2Cu_3O_7$ thin film grown on $LaAlO_3$ substrate, prepared by Dr. R Vasquez using laser ablation. The sample dimensions were a 6.35mm x 6.35mm with a film thickness of 260nm. The zero-field transition temperature and width were

measured using the DC setup discussed in detail in chapter 3. The resistive transition temperature was, $T_c = 87.98K$ and transition width was observed to be, $\Delta T_c = 0.6K$.

The thin film sample preparation for electrical transport measurement included cleaning, masking, sputtering, and connecting electrically and thermally to the probe. Cleaning followed the procedure as for single crystals, rinsed in pure ethanol, rinsed in pure acetone, washed in pure toluene, followed by a rinse in pure ethanol. The duration of the toluene wash was reduced to about 20 seconds. A gold sputtered mask was prepared by sputtering 120 nm of gold on commercially purchased (Reynolds) aluminum foil. The mask was cut to size and shape to mask the surface and sides of the thin film, leaving only the corners exposed. The cutting procedure left edges of aluminum exposed. As aluminum can diffuse into $YBa_2Cu_3O_7$ thin films (to a depth of about 3 nm) and thereby affect the measurements, care was taken to not allow the exposed edges to contact the film. About 100 nm of gold (.9995 purity) was sputtered onto the four corners and expose edges of the film. The sputtering occurred at 20 Watts (to ensure little sample heating during sputtering) for 3 minutes with the sample about 3 cm away from the gold target at a pressure of 1 mTorr of Argon gas. The chamber was dynamically pumped during sputtering. The sample was then placed on a sapphire substrate to ensure good thermal contact with the probe while simultaneously keeping the sample clean. Indium, of purity .995, was rolled between two clean glass slides to reduce its diameter, and then pressed onto the sputtered gold

contacts and along the sapphire substrate, making electrical contact with the sample, and improving the thermal contact of the sample with the substrate. Copper wires were then pressed into the indium on the substrate, and soldered onto the sample probe posts. The total length of indium and copper wire, from the sputtered gold contact to the probe post was less than 7.5 mm (see figure 5-1).

AC longitudinal and Hall resistivities measurements were made for the following conditions.

H = 0, 1, 2, 3, 4, 5 Tesla, oriented along the sample c-axis

T = 80, 82, 84, 86, 87.5, 88, 89, 100K

$j \sim 6.1 \times 10^5$ A/m^2

Linearity of response at the above current density for both the longitudinal and Hall resistivity was verified using the DC setup to measure the current-voltage relationship of the sample over the range of 6.1×10^4 A/m$^2 \leq j \leq 6.1 \times 10^7$ A/m^2. The current density was chosen after trading the advantages of reduced noise with increased current density, noise reduction with increased measurement averaging, increased resolution and accuracy with increased HP 4194A measurement integration time, with the disadvantages of possible increased thermal gradients due to sample heating by the current and the increased time necessary to make the measurement requiring improved thermal stability. A different current density, j ~

$2x10^5$ A/m^2 was also used at 86K to check the current independence of the AC Hall resistivity.

Four-Point Measurements

Measurements were made using a van der Pauw four-point technique. The required van der Pauw corrections were determined using the DC setup. Fortunately, due to the extreme squareness of the sample, $R_{xx}/R_{yy} = 1$ to within about 1%. Consequently, for the AC measurements, only R_{xx} or R_{yy} were needed to be able to do the van der Pauw corrections. Additionally, following the van der Pauw approach, and since the longitudinal component of resistivity is invariant under field reversal while the Hall component of resistivity reverses its sign under field reversal, measurement in only one diagonal direction was necessary to determine the Hall resistivity. These observations eliminated the need for the additional switching of the current-voltage pairs required in the DC setup.

Calibrations

All impedances measured with the AC setup, using the HP 4194A and having uncompensated cable length, must be corrected for the uncompensated cable length before being applied in the following calibrations. The phase shift due to extended cable length must be accounted for by using the phase correction,

$$\Delta\phi = 2\pi\Delta lf/v,$$

as defined above in the Cable Length Compensation section of this chapter.

The HP 4194A measures the complex impedance, and reports the results as either amplitude and phase, or as real, $Z_{MEAS, REL}$, and imaginary, $Z_{MEAS, IMG}$, components of the complex impedance. For an actual impedance of $Z_{REL} + iZ_{IMG}$, the measured real and imaginary parts of the impedance, as a result of the phase delay $\Delta\phi$ are

$$Z_{REL, MEAS} = Z_{REL} * \cos(\Delta\phi) - Z_{IMG} * \sin(\Delta\phi)$$

and

$$Z_{IMG,MEAS} = Z_{IMG} * \cos(\Delta\phi) + Z_{REL} * \sin(\Delta\phi).$$

The phase shift is easily corrected by a rotation of the complex plane such that

$$Z_{MEAS, REL, CORR} = Z_{MEAS, REL} * \cos(\Delta\phi) + Z_{MEAS, IMG, CORR} * \sin(\Delta\phi),$$

and

$$Z_{MEAS, IMG, CORR} = Z_{MEAS, IMG} * \cos(\Delta\phi) - Z_{MEAS, REL} * \sin(\Delta\phi),$$

Note that this phase correction is the only required phase correction for this setup, as this directly considers all the phase delays in the system. This is verified for T »

T_c, where the actual impedance, $Z_{DUT} = Z_{REL}$. At 100 K, this calculated phase delay accounts for all the phase delay to within ± 0.5 degrees. (Note, the accuracy of the closed potential path is to within about ± 1 %.) The temperature independence of the phase delay due to uncompensated path length was verified using the AC longitudinal setup for zero field measurements between 70 K and 87K. (The AC Hall setup measures zero signal in zero field, as is seen from the calibration procedures below) The field independence of the uncompensated path length was verified using both the AC longitudinal and Hall setups at 100 K for fields at 0, 1, 2, 3, 4 and 5 Tesla. Therefore, any changes in phase in the various experimental conditions will be the result of the $YBa_2Cu_3O_7$ thin film.

Reed (1995) compensated for phase shift by performing a coordinate system rotation after all other calibrations. This approach was acceptable, as all the measured values had the same phase shift, and the data was reported as amplitude and phase.

AC Longitudinal Impedance Calibration

The measured impedance, Z_{MEAS}, includes the sample impedance, Z_{DUT}, any background impedance, Z_{BACK}, amplifier gain and system losses, G(f), and phase shifts, θ(f). This is represented as

$$Z_{MEAS} = (Z_{DUT} + Z_{BACK})G(f)e^{i\theta(f)},$$

where,

Z_{DUT} is the sample impedance, DUT (device under test) refers to the sample,

Z_{BACK}, is the parasitic impedances, capacitances and inductances, and is purely imaginary,

G(f) is the frequency dependent amplifier gain, and includes end-to-end losses, impedance mismatches, and contact resistances, and is considered to be purely real,

$\theta(f)$ is the frequency dependent phase shift due to the uncompensated cable length, including that due to the differential amplifier.

The desired $YBa_2Cu_3O_7$ thin film sample signal is denoted Z_{DUT}. To obtain Z_{DUT},

(1) Apply the above phase correction to all measured values. Therefore,

$$Z_{MEAS,\,CORR} = (Z_{DUT} + Z_{BACK})G(f).$$

(2) Assume G(f) and Z_{BACK} are each independent of the temperature of the sample. Therefore

$$Z_{MEAS,\,CORR} = (Z_{DUT} + Z_{BACK})G(f), \text{ for all T near } T_c. \quad (A)$$

(3) Assume that $Z_{DUT} \approx 0$, if DUT is pure gold foil of the approximate size, but much thicker, and of the same shape as the thin film sample. (Note that the resistivity of gold ~ 10^{-8} Ωm at T = 293K.) Therefore, to determine Z_{BACK}, gold is used, and

$$Z_{MEAS,\,BACK,\,CORR} = Z_{BACK}G(f). \quad (B)$$

(4) Assume that Z_{DUT} is frequency independent and real, for $T \gg T_c$ up to 10 MHz, and therefore,

$$Z_{DUT}(f) = |Z_{DUT}| = Z_{DUT}(f = 0), \text{ for } T \gg T_c. \quad (C)$$

(5) Assume that $|Z_{DUT}| \gg |Z_{BACK}|$, for $T \gg T_c$. Therefore,

$$Z_{MEAS,\,CORR} \approx Z_{DUT}G(f), \text{ for } T \gg T_c.$$

This implies that

$$| Z_{MEAS,\,CORR} | = | Z_{DUT} | G(f), \text{ for } T \gg T_c. \qquad (D)$$

(6) Combining (C) with (D), the frequency dependent gain is determined by

$$G(f) = | Z_{MEAS,\,CORR} | \; / \; | Z_{DUT}(f = 0) |, \qquad (E)$$

where $| Z_{DUT}(f = 0) |$ has been determined using the DC setup.

All parameters have been determined, within the ability to resolve random errors in Z_{MEAS}. Again, it is important to apply the corrections for the uncompensated cable length to all measured impedances before using the results. This would complete the calibration, except that the range resistors step error, discussed above, and in the thesis by Reed (1995) and by Reed et al. (1994).

(7) Assume the steps are caused by range resistor switching, that its errors occur within the HP 4194A, and that the errors are therefore invariant under switching the voltage leads, and invariant under magnetic field reversal. Therefore, for the forward switch direction,

$$Z_{MEAS+} = Z_{MEAS} + Z_{STEP},$$

and in the reverse switch direction,

$$Z_{MEAS\,-} = -Z_{MEAS} + Z_{STEP}.$$

Therefore,

$$Z_{MEAS} = (Z_{MEAS\,+} - Z_{MEAS\,-})/2.$$

AC Hall Impedance Calibration

The AC Hall impedance calibration is more straightforward than the AC longitudinal impedance calibration, as most unwanted signals are invariant under field reversal. Therefore, the measuring and removing of the background, as in the AC longitudinal impedance calibration, is not only unnecessary, but cannot be done, as under field reversal, the background cannot be measured. The AC Hall impedance has the same general form as for the AC longitudinal impedance measurement,

$$Z_{MEAS} = (Z_{DUT,\,HALL} + Z_{BACK})G(f)e^{i\theta(f)}.$$

(1) Assume G(f) and Z_{BACK} are each independent of the temperature of the sample, and recall that the temperature independence of $\theta(f)$ has been measured. Therefore

$$Z_{MEAS} = (Z_{DUT} + Z_{BACK})G(f)e^{i\theta(f)}, \text{ for all T near } T_c. \quad (A)$$

Here, Z_{BACK} is considered complex, as it not only includes parasitic impedances, capacitances and inductances, but also includes possible contributions from the longitudinal impedance, due to the misalignment of contacts (caused by placement of contacts on the sample, and by non-symmetry of the sample dimensions). The longitudinal contribution can be significant for Hall impedance measurements, as the longitudinal impedance is typically more than two orders of magnitude greater than the Hall impedance.

(2) Assume that the background impedance is invariant under field reversal. Denoting the applied magnetic field in the forward direction with a subscript +, and the applied magnetic field in the reverse direction with a subscript -,

$$Z_{BACK,+} = Z_{BACK,-} = Z_{BACK},$$

and in the forward direction,

$$Z_{MEAS,+} = (Z_{DUT,HALL} + Z_{BACK})G(f)e^{i\theta(f)},$$

while in the reverse field direction,

$$Z_{MEAS,-} = (-Z_{DUT,HALL} + Z_{BACK})G(f)e^{i\theta(f)}.$$

The background impedance is easily removed by the averaged difference of the measured impedance in the two field directions,

$$Z_{MEAS,HALL} = (Z_{MEAS,+} - Z_{MEAS,-})/2 = Z_{DUT,HALL}G(f)e^{i\theta(f)}.$$

Also note that the range resistor step is removed by the averaged difference, as the step is also invariant under reversal of the direction of the magnetic field.

(3) Apply the coordinate system rotation to all measured values, as discussed in the AC longitudinal impedance calibration section. Therefore,

$$Z_{MEAS,HALL,CORR} = Z_{DUT,HALL}G(\dot{f}).$$

(4) Assume that $Z_{DUT,HALL}$ is frequency independent and real, for $T \gg T_c$, and therefore,

$$Z_{DUT,HALL}(f) = |Z_{DUT,HALL}| = Z_{DUT,HALL}(f = 0), \text{ for } T \gg T_c.$$

(5) Assume that $|Z_{DUT,HALL}| \gg |Z_{BACK}|$, for $T \gg T_c$. Therefore,

$$Z_{MEAS,\,CORR} \approx Z_{DUT,\,HALL}G(f), \text{ for } T \gg T_c.$$

This implies that

$$|\,Z_{MEAS,\,CORR,}\,| \;=\; |\,Z_{DUT,\,HALL}\,|\,G(f), \text{ for } T \gg T_c.$$

and

$$G(f) = |\,Z_{MEAS,CORR}\,| \;/\; |\,Z_{DUT,\,HALL}(f=0)\,|,$$

where $|\,Z_{DUT,\,HALL}(f=0)\,|$ has been determined using the DC setup.

Temperature Stability

The above longitudinal and Hall impedance calibrations assume no temperature change for both directions (forward and reversed field or forward and reversed switch) of a given measurement condition. If a temperature difference, ΔT, between a given measurement condition in the forward direction and the reverse direction exists, such that (for an AC Hall measurement, for example) H_+ is measured at T, and H_- is measured at $T + \Delta T$, and separating out the contribution from the longitudinal impedance, $\eta Z_{DUT,\,LONG}$, where $\eta \sim 0$ - 1, from Z_{BACK},

$$Z_{MEAS,\,+}(T) = [Z_{MEAS,\,HALL}(T) + \alpha Z_{MEAS,\,LONG}(T) + Z_{BACK}]G(f)e^{i\theta(f)}, \text{ and}$$

$$Z_{MEAS,-}(T + \Delta T) = [-Z_{MEAS,HALL}(T + \Delta T) + \alpha Z_{MEAS,LONG}(T + \Delta T) + Z_{BACK}]G(f)e^{i\theta(f)}.$$

Assuming that $Z_{MEAS,XXXX}(T + \Delta T) = Z_{MEAS,XXXX}(T) + (\delta Z_{MEAS,XXXX}/\delta T) * \Delta T$, and $(\delta Z_{MEAS,XXXX}/\delta T) * \Delta T \ll Z_{MEAS,XXXX}(T)$, the difference between $Z_{MEAS,+}(T)$, and $Z_{MEAS,-}(T + \Delta T)$, ΔZ, is

$$\Delta Z \approx [2Z_{MEAS,HALL}(T) + \alpha(\delta Z_{MEAS,LONG}/\delta T) * \Delta T]G(f)e^{i\theta(f)}.$$

Therefore, temperature stability requirements are such that

$$\alpha(\delta Z_{MEAS,LONG}/\delta T) * \Delta T \ll 2Z_{MEAS,HALL}(T).$$

The adjustable parameters are α, based on contact alignment, size of contacts, and squareness of the sample (for contacts placed in the corner of the sample), and ΔT. Fortunately, for type II high temperature superconductors in magnetic fields, $\delta Z_{MEAS,LONG}/\delta T$ is rather small (has a broad transition width), so that the condition

$$\alpha(\delta Z_{MEAS,LONG}/\delta T) * \Delta T \ll 2Z_{MEAS,HALL}(T)$$

is easily met for $\Delta T \sim 10$ mK.

Theoretical Extensions

Although the following extensions were described (and developed where new) by Yeh (1997) after the data for this experiment were analyzed and the results discussed, the extensions are presented here in advance of the Data, Analyses and Results section of this work to allow the reader to develop an intuition of the results to be presented.

Following the development of the private communication with Yeh (1997):

Consider a frequency-dependent complex longitudinal conductivity, $\sigma_{xx} = \sigma_{xx}' + i\sigma_{xx}''$, and a frequency-dependent Hall conductivity, $\sigma_{xy} = \sigma_{xy}' + i\sigma_{xy}''$. One may assume that the conductivities can be divided into two components, a superconducting component, s, associated with the Cooper pairs and vortices, and a quasiparticle component, q. Taking the Drude approximation, the complex conductivity of a a superconductor normalized to the normal-state DC conductivity, $\sigma_o = ne^2\tau/m^*$, is given by:

$$\frac{\sigma_{xx}(\omega)}{\sigma_o} = \frac{\sigma_{xx}^s + \sigma_{xx}^q}{\sigma_o} = ig\frac{1}{\omega\tau} + (1-g)\frac{1+i\omega\tau}{1+\omega^2\tau^2}. \qquad (1)$$

where g may be considered to represent the superfluid fraction, such that $g \to 1$ for $T \ll T_c$, and $g \to 0$ for $T \to T_c$. Equation (1) is consistent with the Mattis-Bardeen theory (Mattis and Bardeen, 1958), which asserts that $\sigma_{xx}'' \propto \omega^{-1}$ and $\sigma_{xx}'' \gg \sigma_{xx}'$ as $T \to 0$. Therefore,

$$\frac{\sigma_{xx}'(\omega)}{\sigma_o} = \frac{(1-g)}{1+\omega^2\tau^2}$$

$$\frac{\sigma_{xx}''(\omega)}{\sigma_o} = \frac{g}{\omega\tau} + (1-g)\frac{\omega\tau}{1+\omega^2\tau^2}$$

(2)

In the limit of $\omega\tau \ll 1$, consistent with the AC experiment conducted, $\sigma_{xx}' \approx (1\text{-}g)\sigma_o$, is nearly frequency-independent for all temperatures. The frequency dependence of σ_{xx}'' is temperature dependent. For $T \ll T_c$, $g \rightarrow 1$ and $\sigma_{xx}''(\omega) \propto \omega^{-1}$. For $T \gg T_c$, $g \rightarrow 0$ and $\sigma_{xx}''(\omega) \propto \omega$. Therefore considering the conmplex resistivity, ρ_{xx}, and taking $\rho_o \equiv 1/\sigma_o$,

$$\frac{\rho_{xx}'}{\rho_o} = \frac{\sigma_{xx}'/\sigma_o}{(\sigma_{xx}'/\sigma_o)^2+(\sigma_{xx}''/\sigma_o)^2} \approx 0 \ , \ T \ll T_C$$

$$\approx 1 \ , \ T \gg T_C$$

$$\frac{\rho_{xx}''}{\rho_o} = \frac{\sigma_{xx}''/\sigma_o}{(\sigma_{xx}'/\sigma_o)^2+(\sigma_{xx}''/\sigma_o)^2} \approx -\omega\tau \ , \ T \ll T_C \text{ and } T \gg T_C$$

(3)

The results predicted by the simple model in equation (3) will be used to test the validity of the AC setup in this work.

The complex Hall conductivity, σ_{xy}, is described by extending the theory by Feigel'man et al. (1995) to finite frequencies and using the Drude appoximation (Drude, 1900).

$$\frac{\sigma_{xy}(\omega)}{\sigma_o} = \frac{\sigma^s_{xy} + \sigma^q_{xy}}{\sigma_o}$$

$$\approx \frac{1}{\omega_c\tau}\left\{ g\frac{(\omega_o\tau)^2\left[1+(\omega_o\tau)^2+(\omega_o^2-\omega)\tau^2+i(2\omega\tau)\right]}{\left[1+(\omega_o^2-\omega^2)\tau^2\right]^2+4\omega^2\tau^2} - \frac{\delta n}{n}\right\} +$$

$$\left\{ (1-g)\frac{\omega_c\tau}{\left[1+(\omega_c^2-\omega^2)\tau^2\right]^2+4\omega^2\tau^2}\left[1+(\omega_o^2-\omega)\tau^2+i(2\omega\tau)\right]\right.$$

(4)

For $\omega_c\tau \gg \omega\tau$ and $\omega_o\tau \gg \omega\tau$, except for temperatures as close to T_c as $(1 - T/T_c) < 10^{-6}$, the real and imaginary parts can be approximated by the following expressions:

$$\frac{\sigma_{xy}'}{\sigma_o} \approx \frac{1}{\omega_c\tau}\left\{ g\frac{(\omega_o\tau)^2}{1+(\omega_o\tau)^2} - \frac{\delta n}{n} + (1-g)\frac{(\omega_c\tau)^2}{1+\omega_c^2\tau^2}\right\},$$

$$\frac{\sigma_{xy}''}{\sigma_o} \approx \frac{1}{\omega_c\tau}\left\{ g\frac{2\omega\tau(\omega_o\tau)^2}{\left[1+(\omega_o\tau)^2\right]^2} + (1-g)\frac{2\omega\tau(\omega_c\tau)^2}{\left[1+(\omega_o\tau)^2\right]^2}\right\}.$$

(5)

Therefore, in the low frequency limit, $\omega\tau \ll 1$, σ_{xy}' recovers the DC Hall conductivity expression by Feigel'man et al. (1995), and is nearly frequency independent for all temperatures. On the other hand, $\sigma_{xy}'' \propto \omega$ for all temperatures.

The magnetic field dependence of σ_{xy}' and σ_{xy}'' will depend on whether quasiparticles are the sole contributor to the vortex-state Hall conductivity (Spielman et al., 1994), or if there are additional contributions from Cooper pairs and vortices. If quasiparticles are the sole contributor to the vortex-state Hall conductivity, Spielman et al. (1994) assume $\sigma_{xy} =$

σ_{xy}^{q}, and $\sigma_{xy}^{s} = 0$, which would result in $\sigma_{xy}'/\sigma_o \sim (1 - g)\omega_c\tau \propto B$, and $\sigma_{xy}''/\sigma_o \approx 2(1 - g)(\omega_c\omega\tau^2) \propto B$ for $T \ll T_c$. Yeh (1997) considered contributions from Cooper pairs and vortices, in addition to the contribution from quasiparticles, such that for $T \ll T_c$, and $g \rightarrow 1$,

$$\frac{\sigma_{xy}'}{\sigma_o} \approx \frac{1}{\omega_c\tau}\left[1 - \frac{\delta n}{n}\right] \propto \frac{1}{B},$$
$$\frac{\sigma_{xy}''}{\sigma_o} \approx \frac{2\omega}{\omega_c(\omega_o\tau)^2} \propto \frac{1}{B}. \qquad (6)$$

For intermediate temperatures below T_c, the superfluid fraction g decreases with increasing magnetic field. Consequently, both σ_{xy}' and σ_{xy}'' may decrease with increasing B at a lager than inverse linear power. Regardless of the exact B dependence of the superconducting component σ^{s}_{xy}, an unambiguous distinction can be made between the contributions of σ^{s}_{xy} and σ^{q}_{xy}. σ^{s}_{xy} decreases with increasing B, and σ^{q}_{xy} increases with increasing B.

Analysis, Results, and Discussion

The corrected real and imaginary sample impedance data, $Z_{DUT, REL, CORR}$ and $Z_{DUT, IMG, CORR}$, obtained after calibrations of the measured longitudinal and Hall impedance under the various experimental conditions, are first obtained. These data are then converted to amplitude and phase data. The van der Pauw (1958, 1961) corrections are used to convert the amplitudes of the calibrated impedance data to frequency dependent longitudinal and Hall resistivity amplitudes. The resulting calibrated and van der Pauw corrected data is taken to be the raw data, AC Hall and longitudinal resistivity amplitudes and phases, as the calibrations and van der Pauw corrections are considered to be part of the measurement. From these calibrated and van der Pauw corrected data, all physical information is derived.

The zero field resistive transition for the $YBa_2Cu_3O_7$ thin film was obtained using the DC setup (see chapters 3 and 4). The transition temperature was determined to be T_c = 87.98K, by the method described in chapter 4. The transition width was found to be, $\Delta T_c \approx 0.6K$. The DC zero-field resistive transition versus temperature is shown in figure 5-5.

The assumptions of temperature and field independent gain, G(f), were validated by comparing the impedance amplitudes with DC Hall and longitudinal resistivity values of the $YBa_2Cu_3O_7$ thin film at five different applied magnetic field values (1, 2, 3, 4, and 5 Tesla), and at two temperatures (86 K and 100 K) at all frequencies. The resultant gains

were within less than ± 1 % for all conditions for frequencies less than 1 MHz, and within about ± 3 % for frequencies from 1 MHz to 7 MHz.

The assumptions of temperature and field independent background phase, $\theta(f)$, were validated by measuring the $YBa_2Cu_3O_7$ thin film under various temperature and field conditions in which the phase is known precisely. That is , for $T \ll T_c$, the phase of the thin film should be 90°, purely inductive, and for $T \gg T_c$, the phase should be 0°, purely resistive. Therefore, any difference in the measured phase among the various conditions would be attributed to a change in the background phase, $\theta(f)$. The temperature independence of $\theta(f)$ was validated using the AC longitudinal setup with the $YBa_2Cu_3O_7$ thin film in the superconducting state, measured in zero field at six temperatures between 70 K and 87 K. The raw phase, $\phi_{xx,\,raw}$ versus frequency at six temperatures data are shown in figure 5-6(a), and validate the temperature independence of $\theta(f)$, as there are no phase differences beyond noise among the various temperatures. At the temperatures shown, the sample should be almost purely inductive with $\phi_{xx,\,raw} \approx 90°$. The field independence of $\theta(f)$ was validated using both the AC longitudinal and AC Hall setups, with the $YBa_2Cu_3O_7$ thin film in the normal state, where the sample should be nearly purely resistive with $\phi_{xx,\,raw}$ and $\phi_{xy,\,raw}$ each nearly equal to zero, measured at a fixed temperature of 100 K in five applied magnetic fields, (1, 2, 3, 4, and 5 Tesla). $\phi_{xx,\,raw}$ and $\phi_{xy,\,raw}$ are nearly field independent at the various frequency. The $\phi_{xx,\,raw}$ versus frequency measured at six fields and T = 100 K data from the AC longitudinal setup, where the six curves are nearly identical, are shown in figure 5-6(b), with the $\phi_{xy,\,raw}$ versus frequency

data measured at five fields and T = 100 K data from the AC Hall setup shown in the inset, again with five nearly identical curves.

More important than verifying the validity of the temperature and field independence of the systems' gain, G(f), and background phase, θ(f), is validating that the technique properly measures the Hall and longitudinal impedances. One easily verified characteristic of the Hall effect is its field dependence in a normal metal. The Hall resistivity should be linear in field in a normal metal. This characteristic therefore should be evident in a superconductor in the normal state. The Hall resistivity amplitude $|\rho_{xy}|$ versus frequency of the $YBa_2Cu_3O_7$ thin film measured at a temperature of 100 K in zero field and in five applied magnetic fields is shown in figure 5-7(a). The linearity of the change in amplitude with field is evident, verifying the validity of the Hall impedance measurements using the AC Hall setup. An easily verified characteristic of longitudinal resistivity in a normal metal is that it is field independent (excluding magnetoresistance effects). Again, this characteristic should be evident for the $YBa_2Cu_3O_7$ thin film in the normal state. The longitudinal resistivity amplitude $/\rho_{xx}/$ versus frequency of the $YBa_2Cu_3O_7$ thin film measured at a temperature of 100 K in zero field and in five applied magnetic fields is shown in figure 5-7(b). The longitudinal resistivity is field independent to within 0.3 %, verifying the validity of the longitudinal impedance measurement using the AC longitudinal setup. (The small field dependence may be accounted for by the measurement temperature not quite far enough away from the transition temperature. Paraconductivity persists in $YBa_2Cu_3O_7$ up to ~ 150 K. Therefore, the $YBa_2Cu_3O_7$ thin film becomes 'more normal' with increasing field. The small field dependence is not a

result of the 1 % difference from squareness of the $YBa_2Cu_3O_7$ thin film yielding a component of the Hall resistivity.)

The $YBa_2Cu_3O_7$ thin film AC Hall and longitudinal resistivity amplitudes, $|\sigma_{xx}|$ and $|\sigma_{xy}|$, respectively, and phases, $\phi_{xx,\sigma}$ and $\phi_{xy,\sigma}$ respectively, as a function of frequency of the $YBa_2Cu_3O_7$ thin film were measured at eight temperatures (82, 84, 86, 87, 87.5, 88, 89,100K) in five applied magnetic fields (1, 2, 3, 4, and 5 Tesla). Representative data measured at applied magnetic fields of 1 and 2 Tesla are shown in figures *5-8 and 5-9*(a) and (b), respectively. The AC Hall and longitudinal resistivity amplitudes are frequency independent up to 1 MHz, within the accuracy and resolution of the measurements. It was known that the AC longitudinal resistivity amplitudes would be frequency independent up to 10^5 Hz, as previously reported by Reed (1995), Jiang et al. (1994),and Reed et al. (1994), with some results up to 2.5 MHz. There is a small frequency dependence above 3 MHz for all measurements conditions within and near superconducting to normal phase transition. Close enough to the vortex-solid to vortex-liquid phase transition, the AC longitudinal resistivity amplitudes appear frequency independent, but this is in part due to the smallness of the signal under these conditions, as compared with the scale of the plot. On the other hand, it is evident from the phase versus frequency plots, that the frequency dependence of the real and imaginary parts of the longitudinal resistivity amplitudes increase as the measurement conditions approach the vortex-solid to vortex-liquid phase transitions. The frequency dependence of the longitudinal phases appear valid as they follow a consistent pattern of increased phase for a given frequency as the $YBa_2Cu_3O_7$ thin

film becomes 'more superconducting' (in this case, more inductive resulting in increasing phase with decreasing temperature).

The frequency dependence of the AC Hall resistivity amplitudes has not been previously measured or predicted in this frequency range and has only recently been explained by Yeh (1997). Consistent with the longitudinal resistivity observations, as the measurement conditions approach the vortex-solid to vortex-liquid phase transition, the frequency dependence above 1 MHz increases. This is clearly seen in *figure 5-8* where at 84 K, ρ_{xx} vanishes (figure 5-8(b)) in a 1 Tesla magnetic field, and the ρ_{xy} isotherm at 84 K in figure 5-*8*(a) begins to show a frequency dependence at about 2 MHz. At the temperatures above 84 K, little frequency dependence of ρ_{xy} is observed below 5 MHz, except near the minimum (the amplitude maximum, $T \approx 87$ K) of the Hall resistivity. For each field, the Hall resistivity amplitude shows the greatest frequency dependence near the mixed state amplitude maximum. Again the Hall phases appear valid as they follow a consistent pattern of increased phase for a given frequency as the $YBa_2Cu_3O_7$ thin film becomes 'more superconducting'. Note that the highest frequency data of the normal state 100 K isotherms show a decrease in phase beyond 3 or 4 MHz. This is most likely an artifact of the system, as at this temperature and frequency, the HP 4194A appears to be slightly overdriven, even though the input voltage was within limits. Although the input voltage was within design limits of the HP 4194A, the overall AC impedance measurement system design may have been beyond the design limits of the HP 4194A (e.g., samples with four ports instead of the system required two, and cable length beyond the 1 meter compensated length) at the highest frequencies for the largest signals measured at 100 K.

As this is a new experimental technique where a new frequency range is explored, questionable data is shown and, for the convenience of the reader, slashes have been placed through this questionable data.

The frequency dependence of the real part of the AC Hall resistivity (denoted as ρ_{xy}') and the real part of the AC longitudinal resistivity (denoted as ρ_{xx}') are related to the cosine of the frequency-dependent phase, as is shown in figure 5-10(a) and (b), respectively, for an applied magnetic field of 2 Tesla and at various temperatures. ρ_{xy}' is relatively frequency independent at all measurement temperatures, as recently described, see above, by Yeh (1997), and is effectively Drude-like. The real part of the longitudinal resistivity (ρ_{xx}') is relatively frequency-independent at all measurement temperatures above 84 K, as predicted using the Drude approximation.

The temperature and field dependencies of the real parts of the AC longitudinal and Hall resistivities are evident, and follow that which would be expected for DC measurements. The real parts of the AC Hall and longitudinal resistivities were compared with DC Hall and longitudinal resistivities of the $YBa_2Cu_3O_7$ thin film measured at two temperatures, 86 K and 100 K and six fields, 0, 1, 2, 3, 4, and 5 Tesla, using the DC setup, and are consistent in magnitude.

The imaginary parts of the AC Hall resistivity (ρ_{xy}'') and AC longitudinal resistivity (ρ_{xx}'') of the $YBa_2Cu_3O_7$ thin film have a linear dependence on frequency, as is shown in figure 5-*11*(a) and (b), respectively, measured in a field of 2 Tesla and at various temperatures. ρ_{xx}' and ρ_{xx}'' are consistent with the results of the Drude approximations and Mattis and Bardeen (1958) above which assert $\sigma_{xx}'' \propto \omega^{-1}$, where $\rho_{xx}'' = 1/\sigma_{xx}''$ and the

results of Yeh (1997), $\sigma_{xx}' \propto \omega^0$, where $\rho_{xx}' = 1/\sigma_{xx}'$. The frequency, temperature and field dependencies of ρ_{xy}' and ρ_{xy}'' have not been previously observed or predicted and are only recently described above (recently developed by Yeh, 1997) and are effectively Drude-like.

The linear response (current independence) of the AC Hall resistivity of the $YBa_2Cu_3O_7$ thin film as a function of frequency was checked for the $YBa_2Cu_3O_7$ thin film in six different applied magnetic fields at a fixed temperature of 86K. The $YBa_2Cu_3O_7$ thin film Hall resistivity amplitude and phase versus frequency was measured at current densities of $6.1x10^4$ A/m^2 and $6.1x10^5$ A/m^2, and is shown in figure 5-*12*(a) and (b), respectively. The AC Hall phase data appears independent of current density, except for increased noise at the lower current density. The AC Hall resistivity amplitude data has differences of about ± 1 - 3 % between the two current densities. That there is no consistent pattern is at first surprising, but the variation is equivalent in magnitude and direction (smaller or larger) to the variation of the average DC Hall resistivity, for current-voltage data, as compared with the DC Hall resistivity at the current density of $6.1x10^5$ A/m^2.

The $YBa_2Cu_3O_7$ thin film AC Hall and longitudinal resistivity data were converted to Hall conductivity (amplitude), $|\sigma_{xy}|$, data at each frequency, temperature and field, following the description in chapters 3 and 4, but neglecting ρ_{xy}^2 in comparison with ρ_{xx}^2 in the divisor of the resistivities to Hall conductivity transformation. Representative AC Hall conductivity amplitude, $/\sigma_{xy}/$, and phase, $\phi_{xy,\sigma}$ versus frequency data of the $YBa_2Cu_3O_7$ thin film measured in an applied magnetic field of 2 Tesla and at various

temperatures are plotted in figure 5-13(a) and (b) respectively. The AC Hall conductivity amplitude data is frequency independent to 5 MHz, except at 86 K. The AC Hall conductivity amplitude at 86 K decreases with frequency beyond about 1.3 MHz.

The real (σ_{xy}') and imaginary (σ_{xy}'') parts of the Hall conductivity data measured at various temperatures and in a field of 2 Tesla are shown in figure 5-14(a) and (b), respectively. σ_{xy}' data are relatively frequency independent, except at 86 K has a slight frequency dependence (about 1%) beyond 2.5 MHz, as recently developed extending the Feigel'man et al. (1995) model (Yeh, 1997). (The σ_{xy}' data at 84 K is not shown due to its magnitude.) The imaginary part of the Hall conductivity is linear in frequency. (The σ_{xy}'' data at 88 K and 89 K are less than zero, and are therefore shown as $-\sigma_{xy}''$.) The low frequency data of σ_{xy}'' is noise due to the smallness of ρ_{xy}'', since the phase for low frequencies is within the resolvable signal of the AC impedance system. The frequency dependence of σ_{xy}' and σ_{xy}'' are consistent with recent calculations of Yeh (1997) extending the DC model of Feigel'man et al. to finite frequencies, as discussed above.

The real (σ_{xy}') and imaginary (σ_{xy}'') parts of the Hall conductivity data measured in various fields and at a temperature of 86 K are shown in figure 5-15(a) and (b), respectively. Again, the σ_{xy}' data are frequency independent, although the 1 and 2 Tesla data have a slight frequency dependence (about 1%) beyond 2.5 MHz. Again, the imaginary part has a linear frequency dependence for the data shown. (4 and 5 Tesla data are not shown as they are less than zero.) Most important in this figure is the field dependence. Spielman et al.(1994) take the Drude approximation (Drude, 1900) to describe the complex vortex-state Hall conductivity and assumed only a quasiparticle

contribution. This would result in a linear dependence of σ_{xy}' and σ_{xy}'' on field. Extending the model of Feigel'man et al.(1995), where vortex and quasiparticle contribution to the Hall conductivity is asserted, and using the Drude approximation, an approximate 1/B dependence is obtained for $T \ll T_c$ as recently developed by Yeh (1997), as discussed above. However, the experiments presented in this thesis are at temperatures slightly less than T_c, and the σ_{xy}' and σ_{xy}'' data in figure 5-15 have a greater than an inverse dependence on field, and different dependencies on field, i.e.,

$$\sigma_{xy}' \propto 1/B^{\alpha}, \text{ where } \alpha > 1, \text{ for } T < T_c,$$

and

$$\sigma_{xy}'' \propto 1/B^{\beta}, \text{ where } \beta > 1, \text{ for } T < T_c.$$

as is seen in figure 5-16, and expected from the theoretical extensions since $T < T_c$ rather than $<< T_c$.

Summary of the AC Hall Effect Experiment

A new technique for measuring the AC Hall effect in the frequency range of 100 Hz and 7 MHz has been developed and experimentally validated. The useful frequency range is presently limited only by the HP 4194A impedance analyzer. The real parts of the AC Hall and longitudinal resistivities, and the Hall conductivity have values equivalent to those with which compared from DC measurements, and are relatively frequency independent in the measured frequency range. The imaginary part of the complex vortex-state Hall conductivity is observed to have linear frequency dependence, $\sigma_{xy}'' \propto \omega$. Both

the real and imaginary parts of the complex vortex-state Hall conductivity have a greater than (and unequal) inverse field dependence as predicted above for $T < T_c$ and the superfluid fraction $\propto g$ decreasing with increasing field, i.e., $\sigma_{xy}' \propto 1/B^{\alpha}$ and $\sigma_{xy}'' \propto 1/B^{\beta}$, where $\alpha, \beta > 1$, and $\alpha \neq \beta$. σ_{xy} decreasing with increasing field unambiguously implies that vortices are the predominant contribution to the vortex-state Hall effect, and is in direct contradiction with the prediction of linear field dependence if quasiparticles are the predominant contribution to the vortex-state Hall effect.

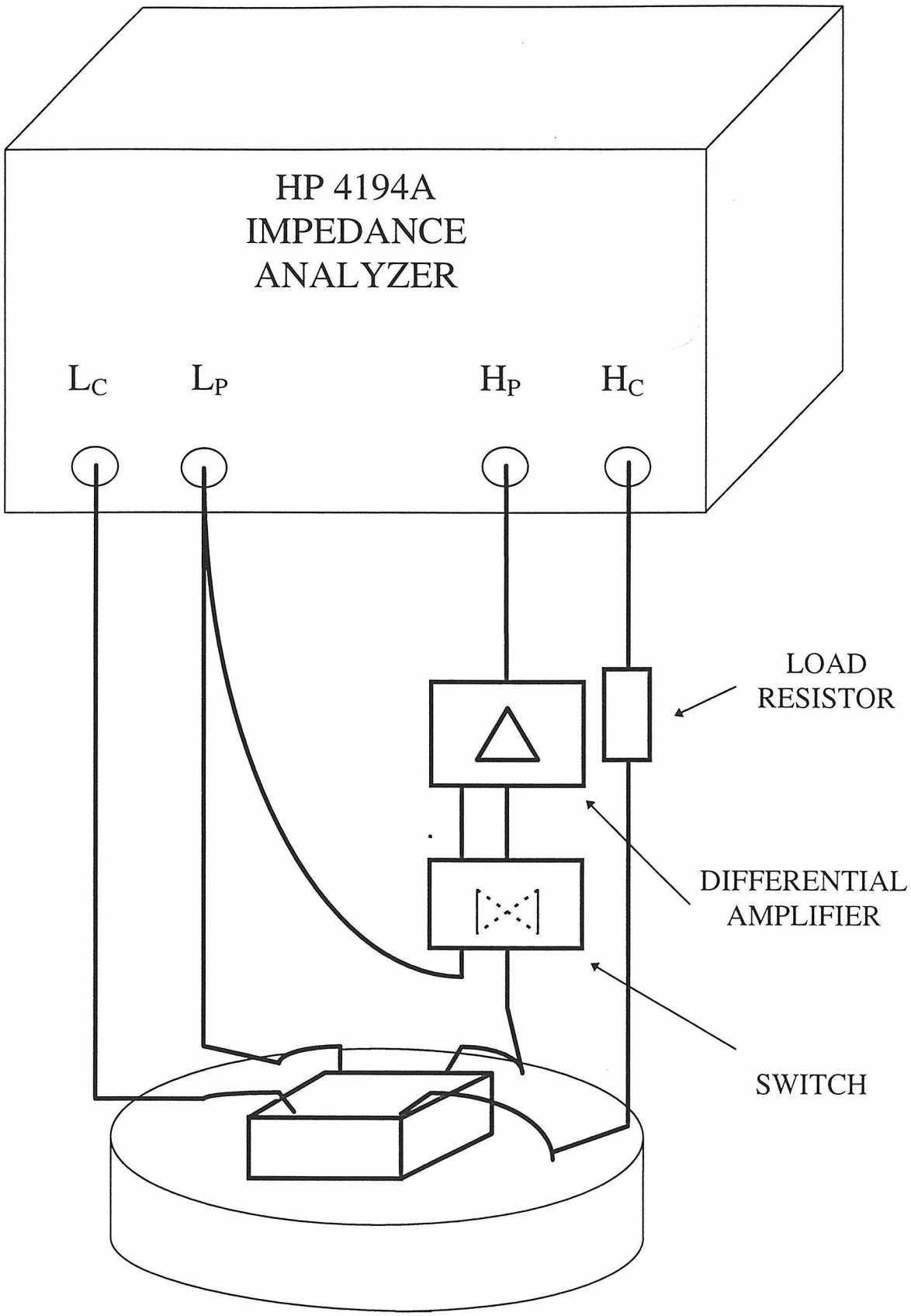

Figure 5-1 AC longitudinal impedance setup

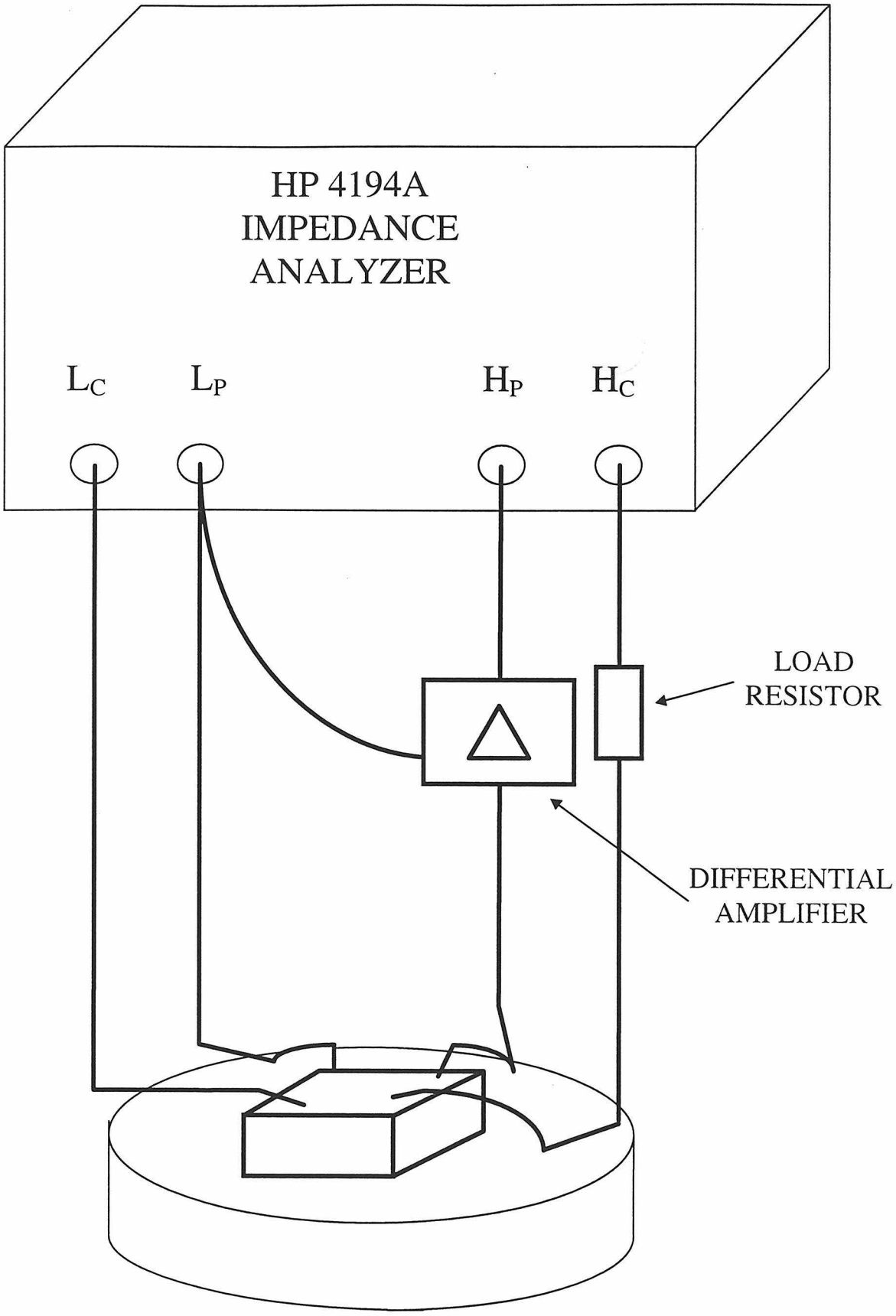

Figure 5-2 AC Hall impedance setup

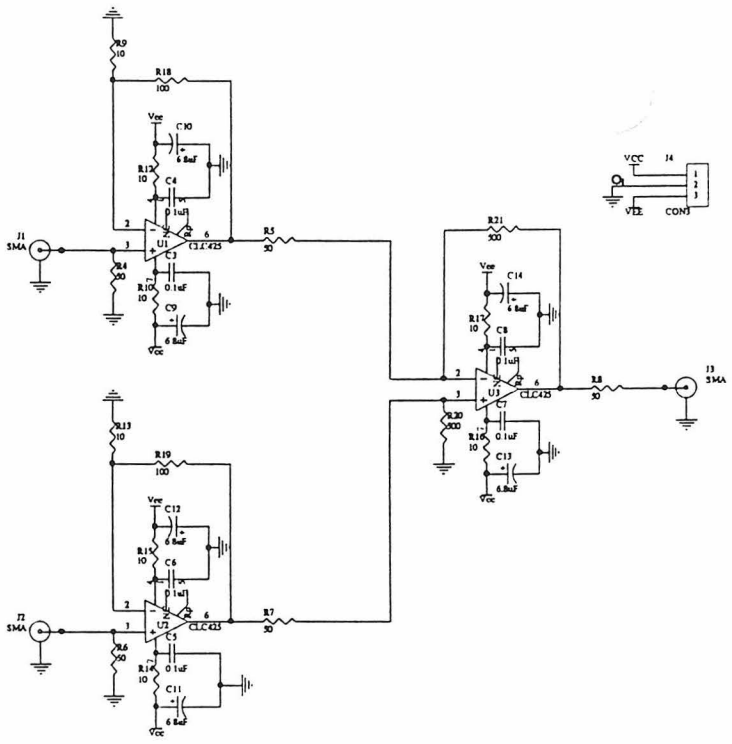

Figure 5-3(a) Schematic of 42 dB differential amplifier

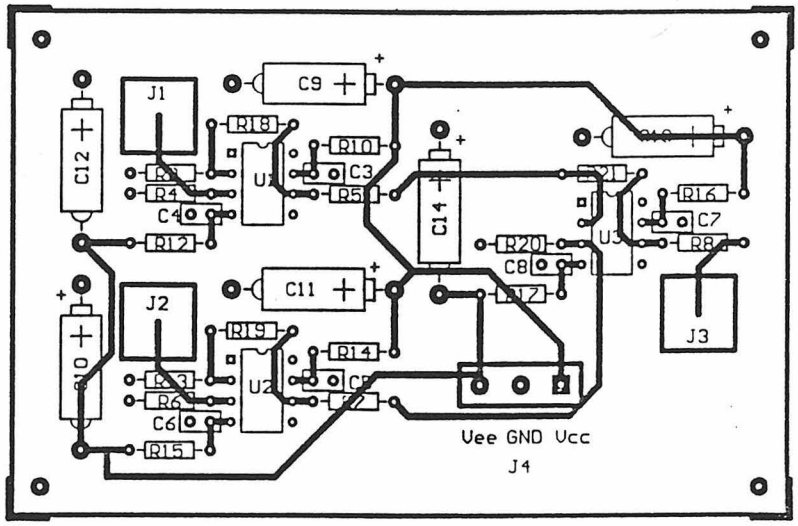

Figure 5-3(b) Layout of 42 dB differential amplifier

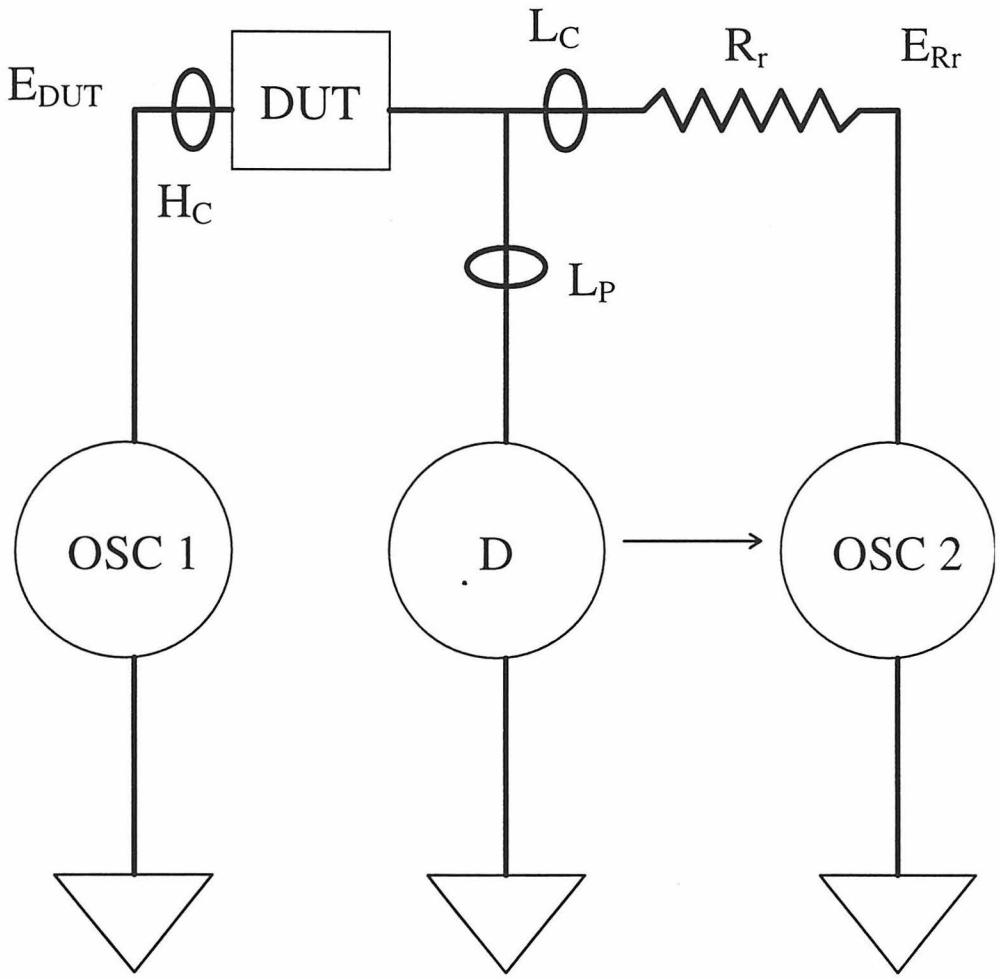

Figure 5-4 Functional diagram of auto balancing bridge

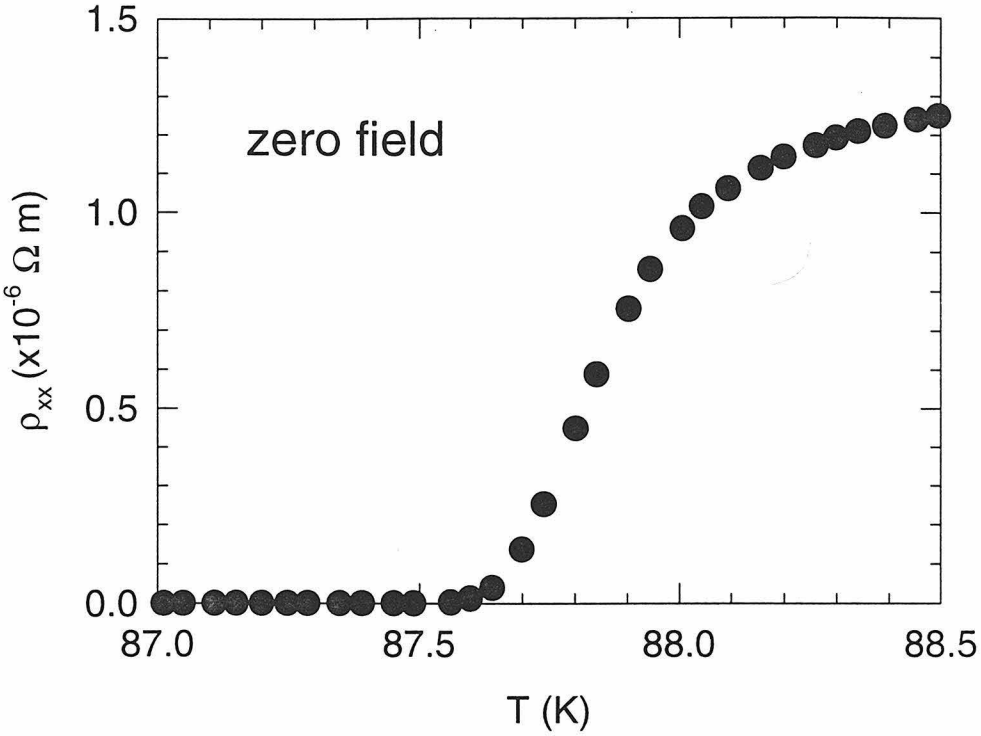

Figure 5-5 Resistive transition of $YBa_2Cu_3O_7$ thin film in zero field

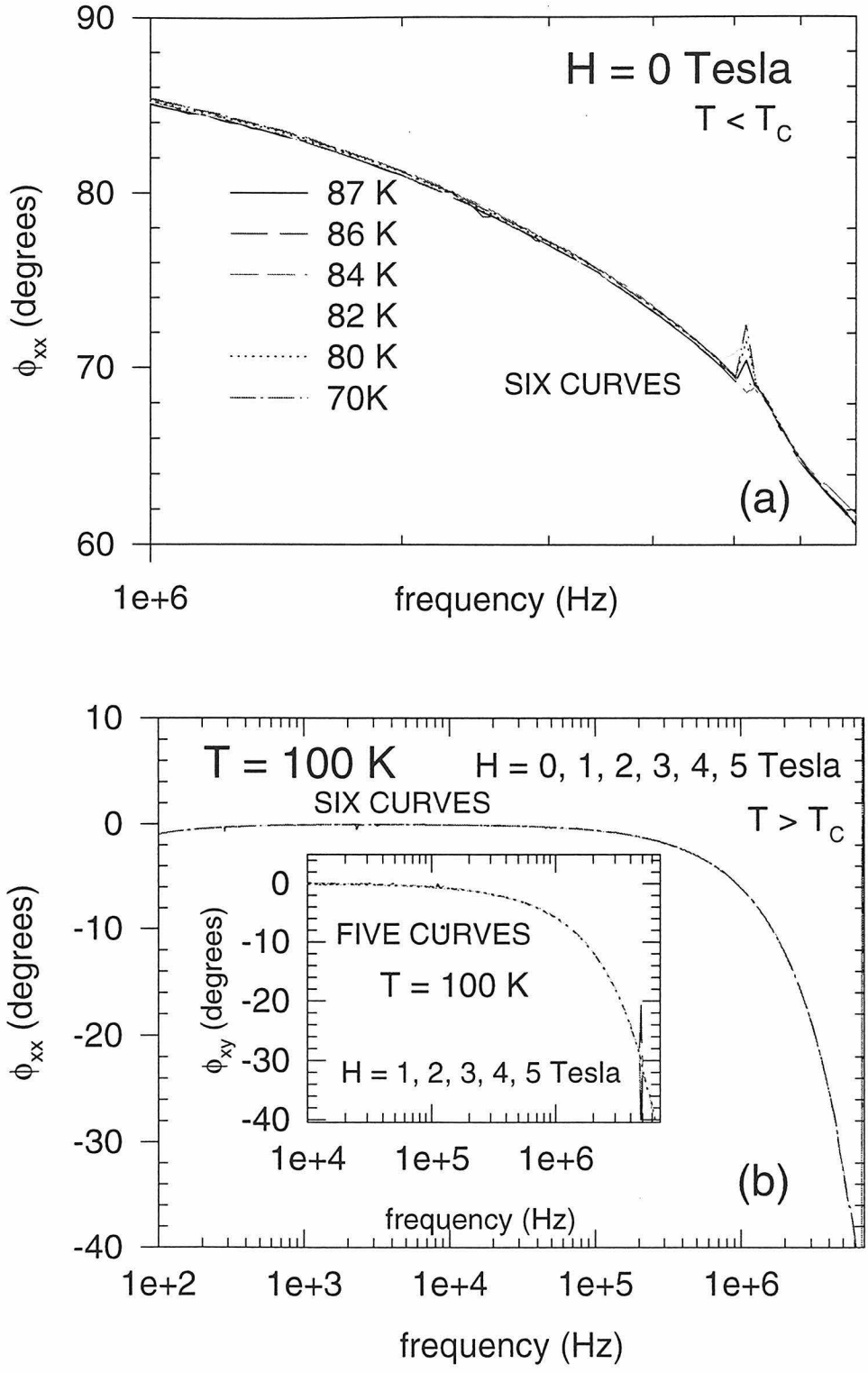

Figure 5-6 Comparison of ϕ_{xx} and ϕ_{xy} at various temperatures or fields

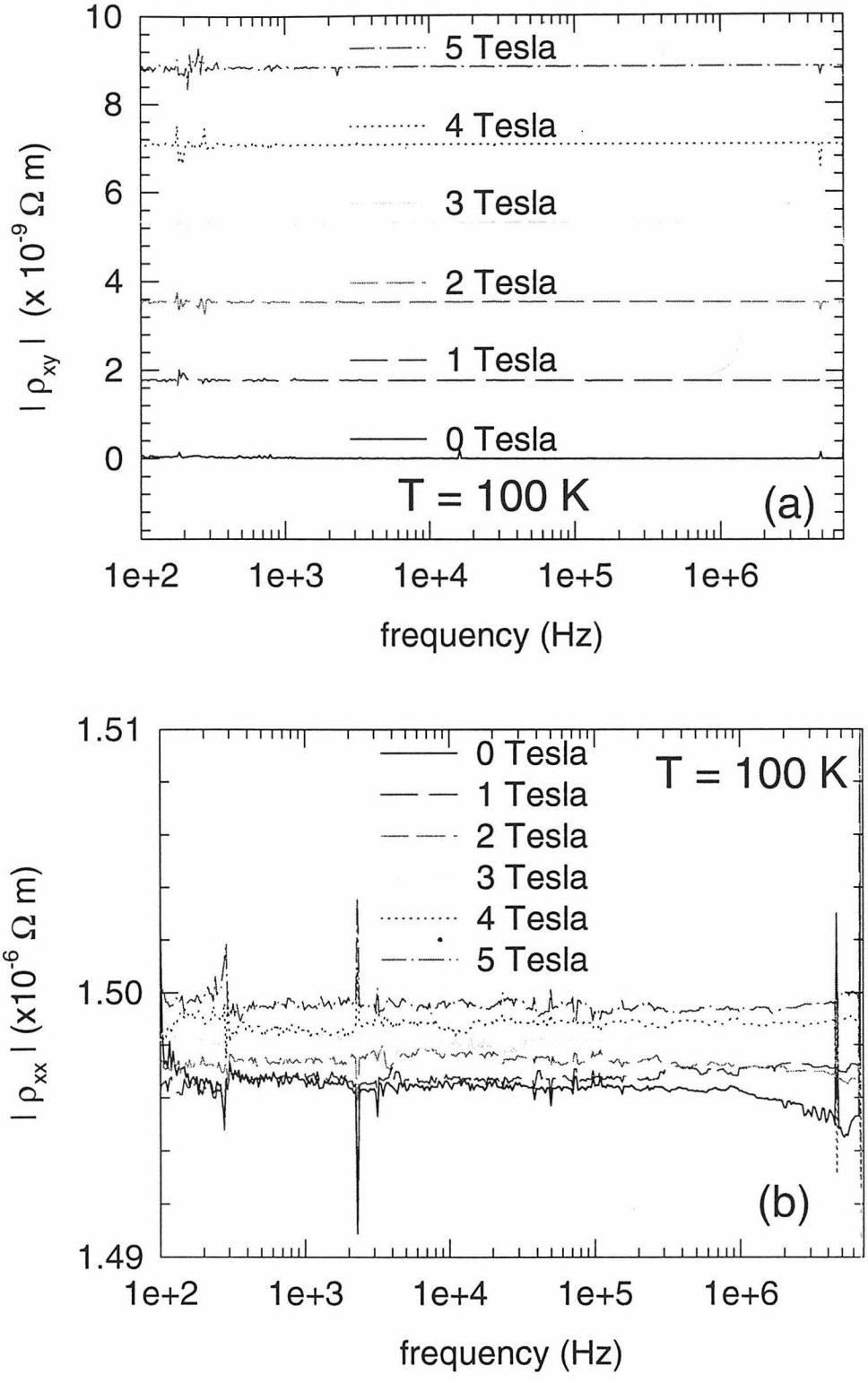

Figure 5-7 Validation of AC impedance technique at $T > T_C$

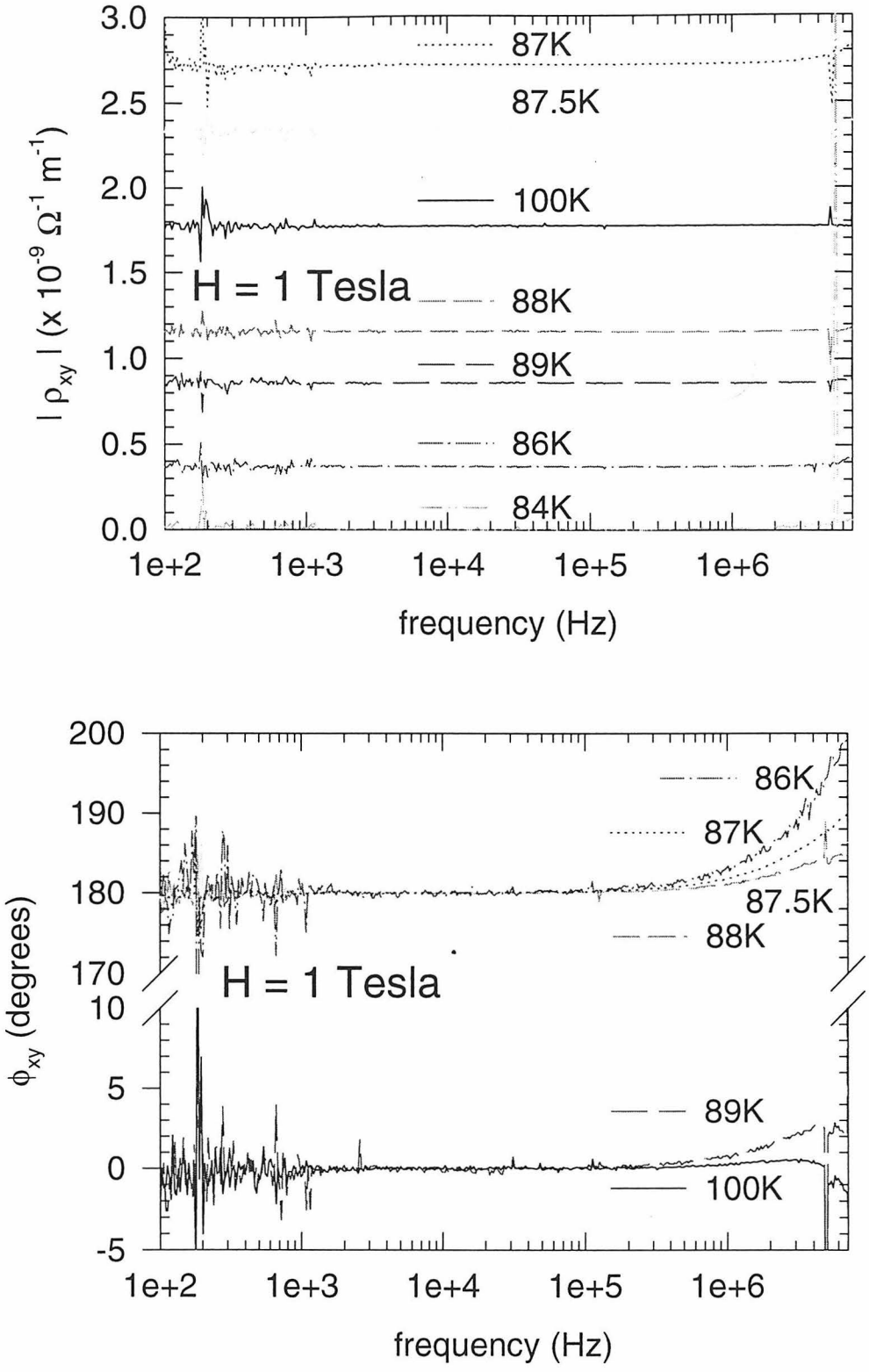

Figure 5-8(a) $|\rho_{xy}|$ and ϕ_{xy} versus frequency at various temperatures and a field of 1 Tesla

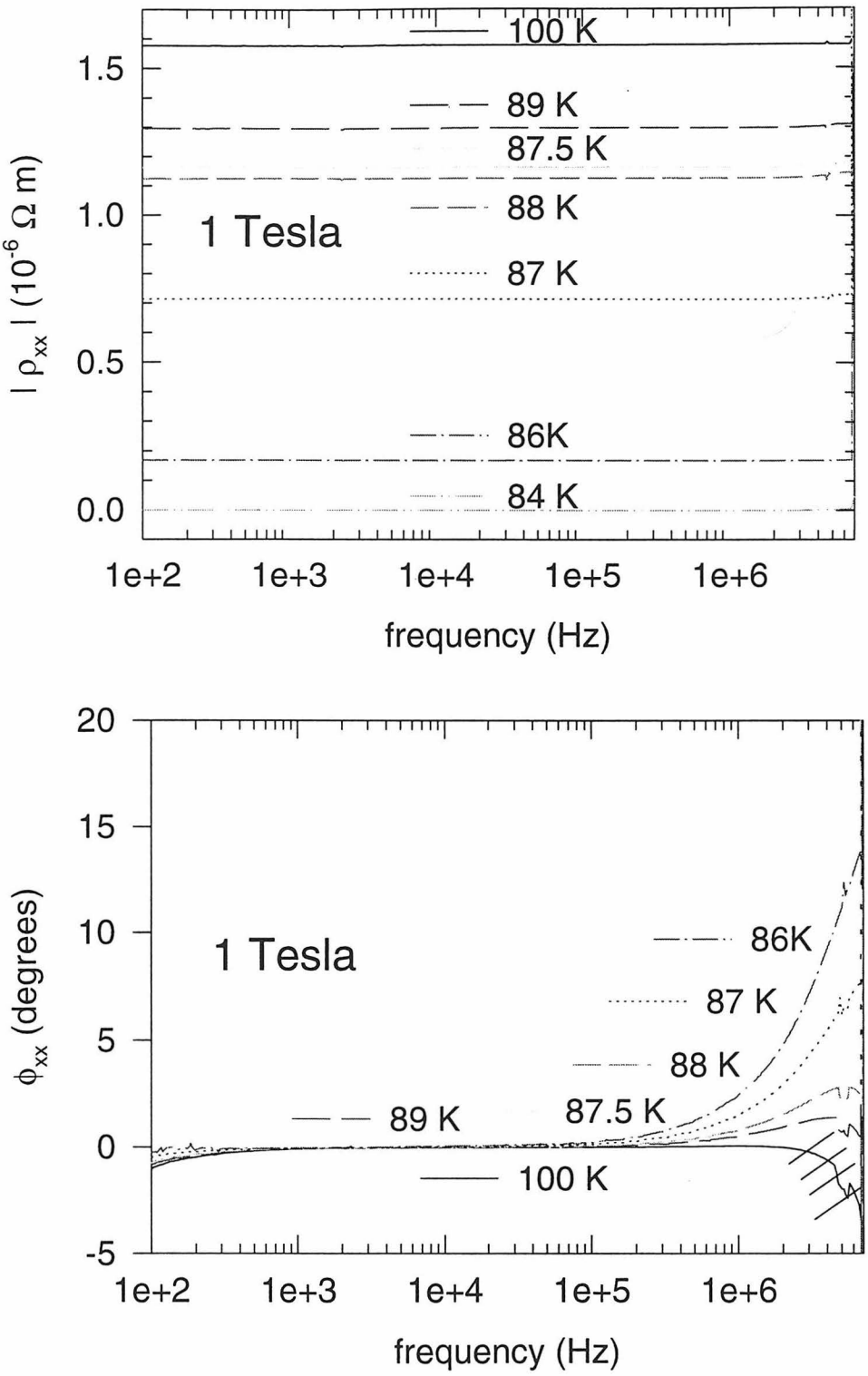

Figure 5-8(b) | ρ_{xx} | and ϕ_{xx} versus frequency at various temperatures and a field of 1 Tesla. Slashes denote region where validity of data is questionable.

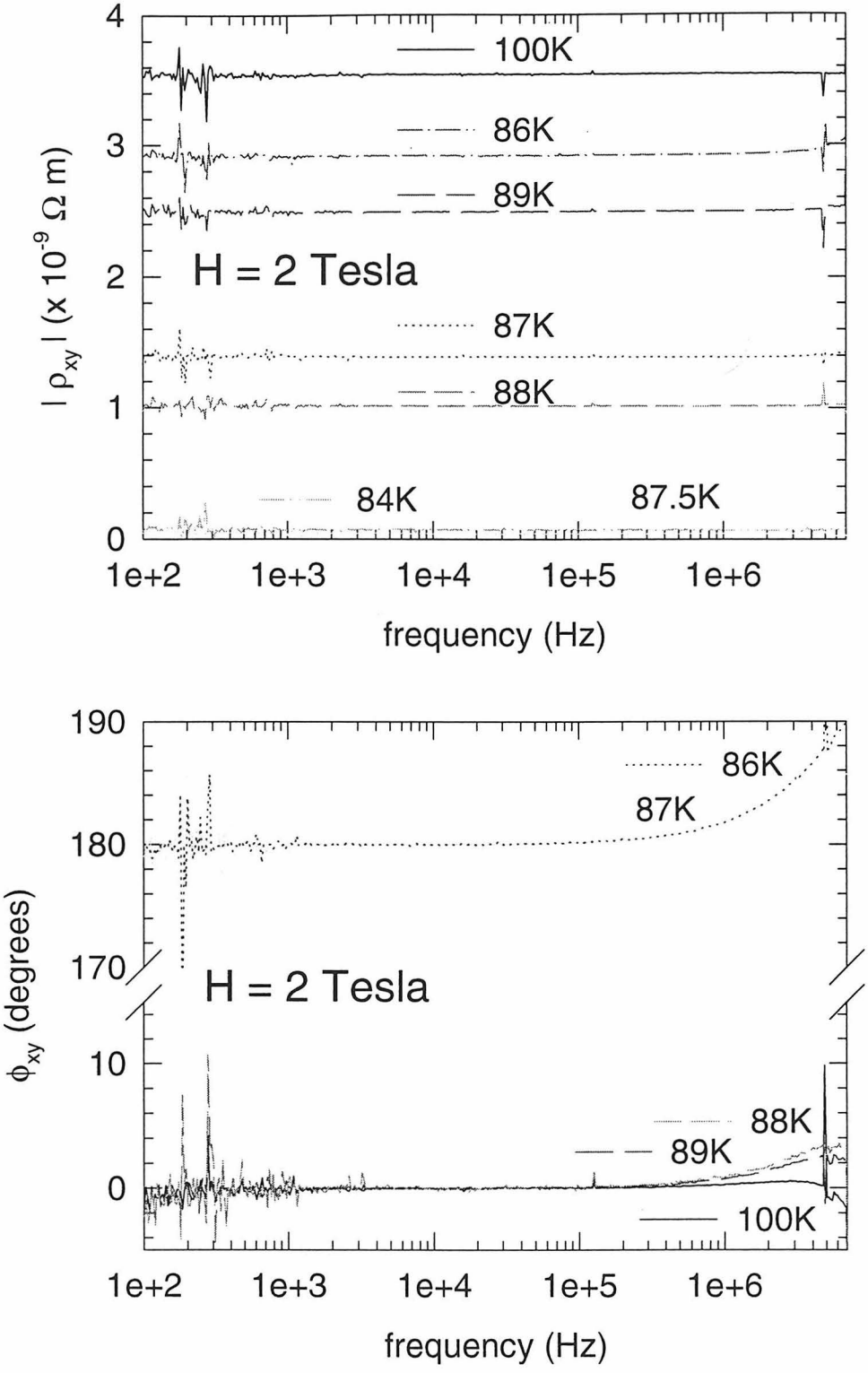

Figure 5-9(a) $|\rho_{xy}|$ and ϕ_{xy} versus frequency at various temperatures and a field of 2 Tesla

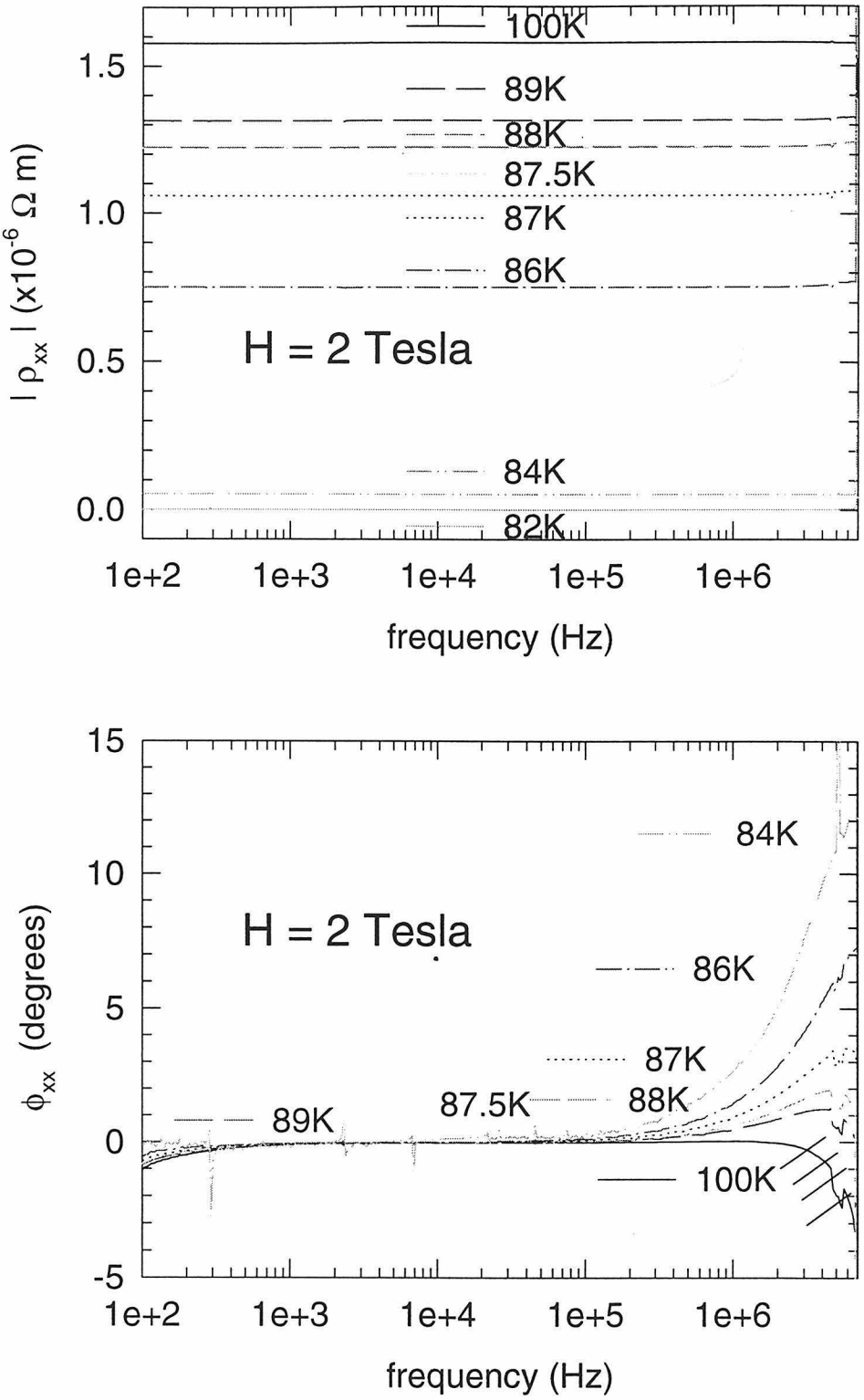

Figure 5-9(b) $|\rho_{xx}|$ and ϕ_{xx} versus frequency at various temperatures and a field of 2 Tesla. Slashes denote region where validity of data is questionable.

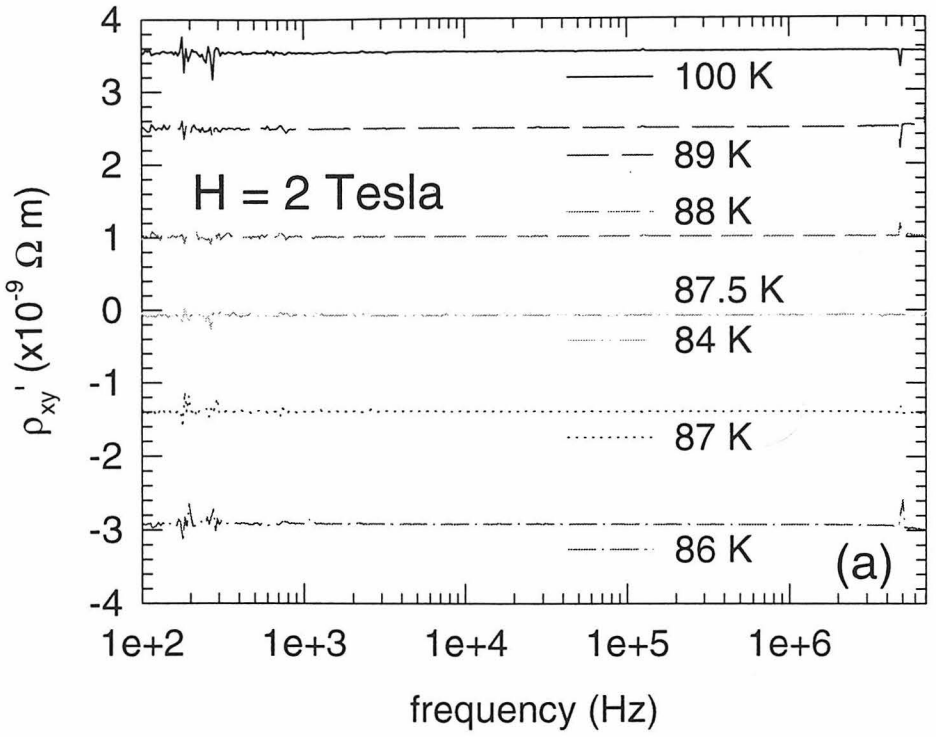

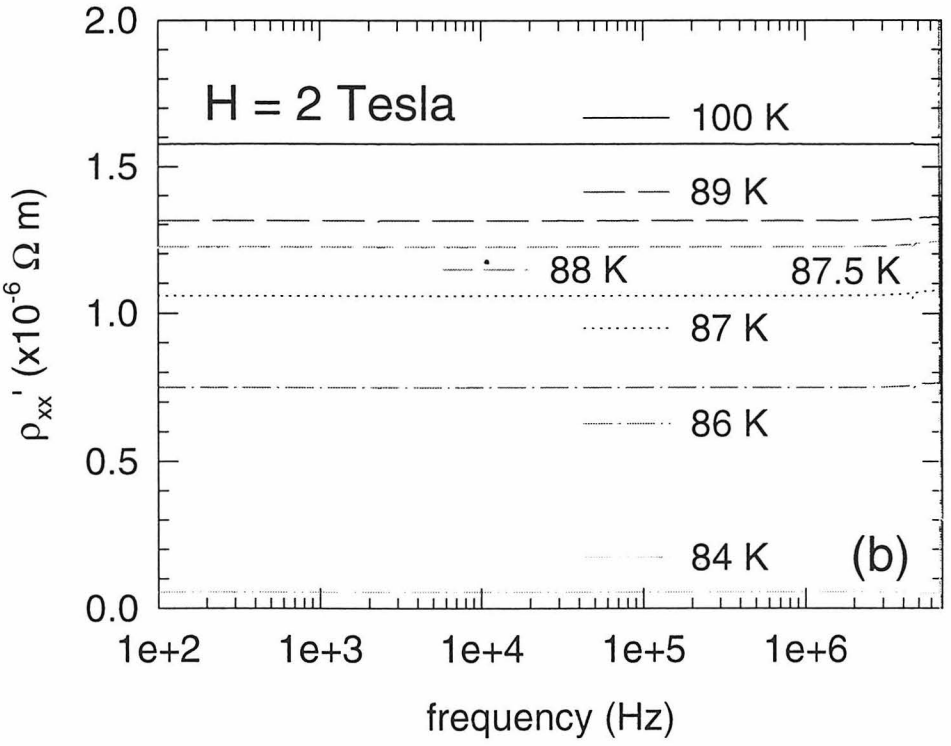

Figure 5-10 ρ_{xy}' and ρ_{xx}' at various temperatures and H = 2 Tesla

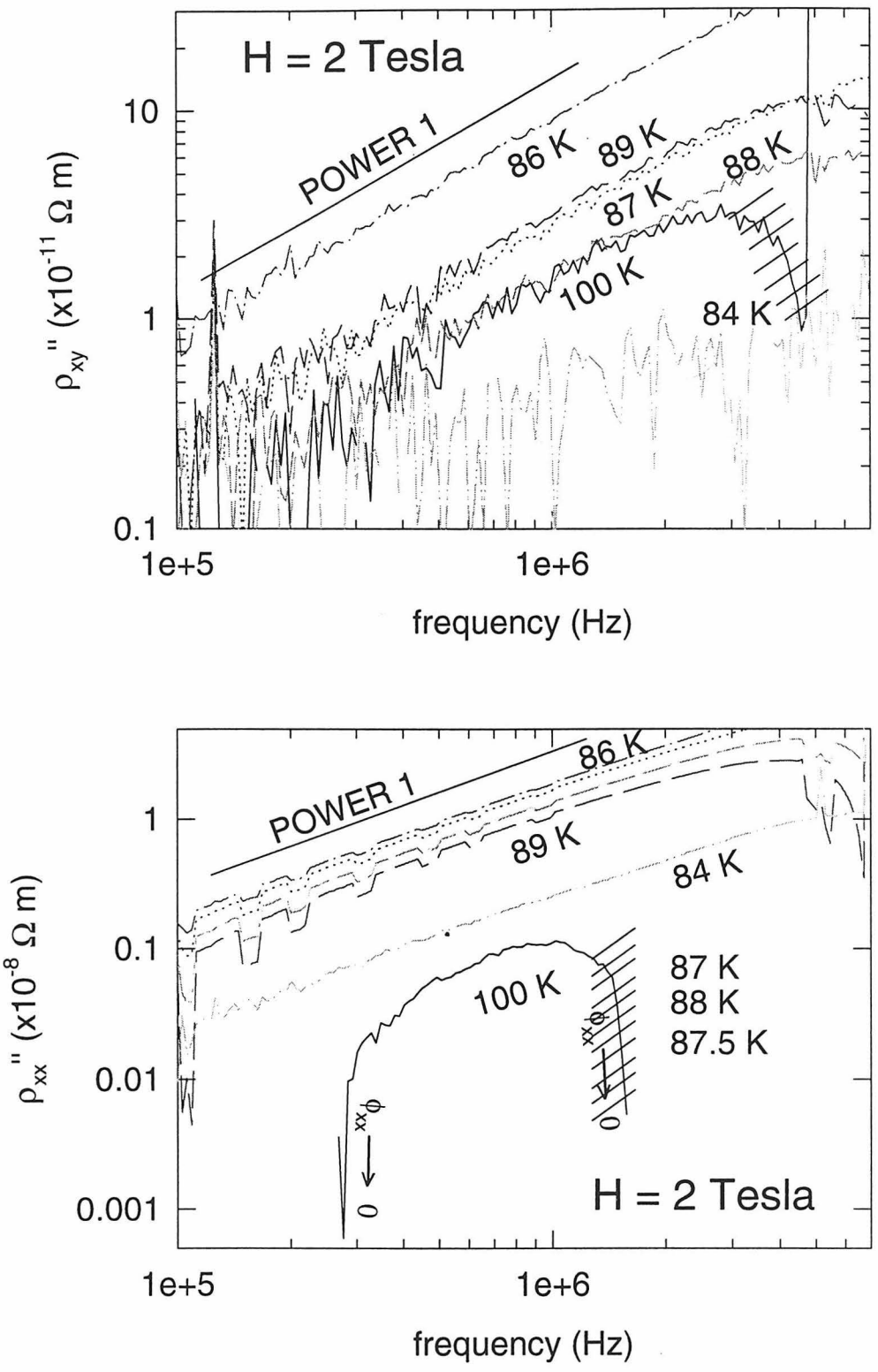

Figure 5-11 ρ_{xy} " and ρ_{xx} " at various temperatures and H = 2 Tesla.
Slashes denote region where validity of data is questionable.

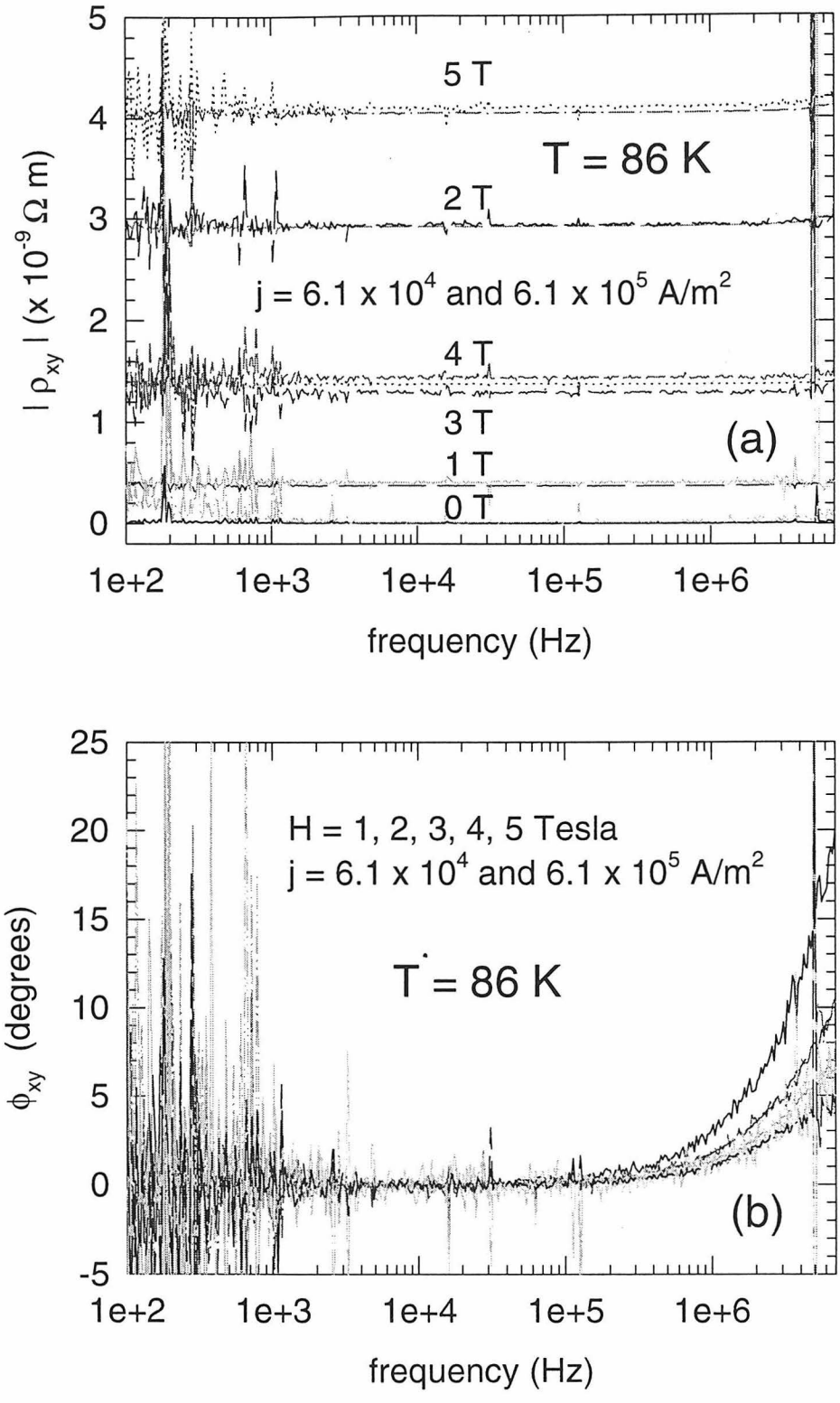

Figure 5-12 Current independence of ρ_{xy} at T = 86 K

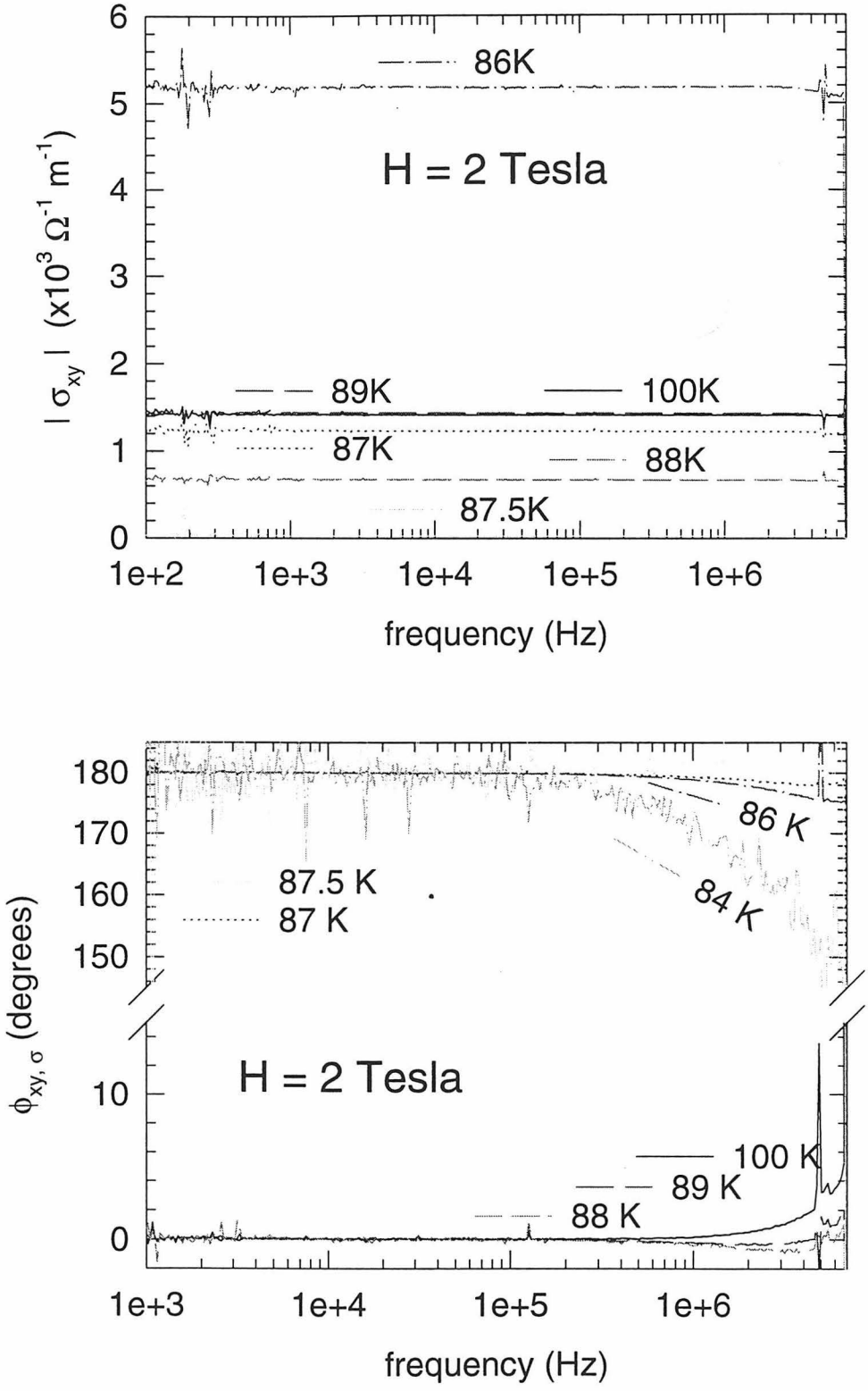

Figure 5-13 $|\sigma_{xy}|$ and $\phi_{xy,\sigma}$ at various temperatures and a field of 2 Tesla

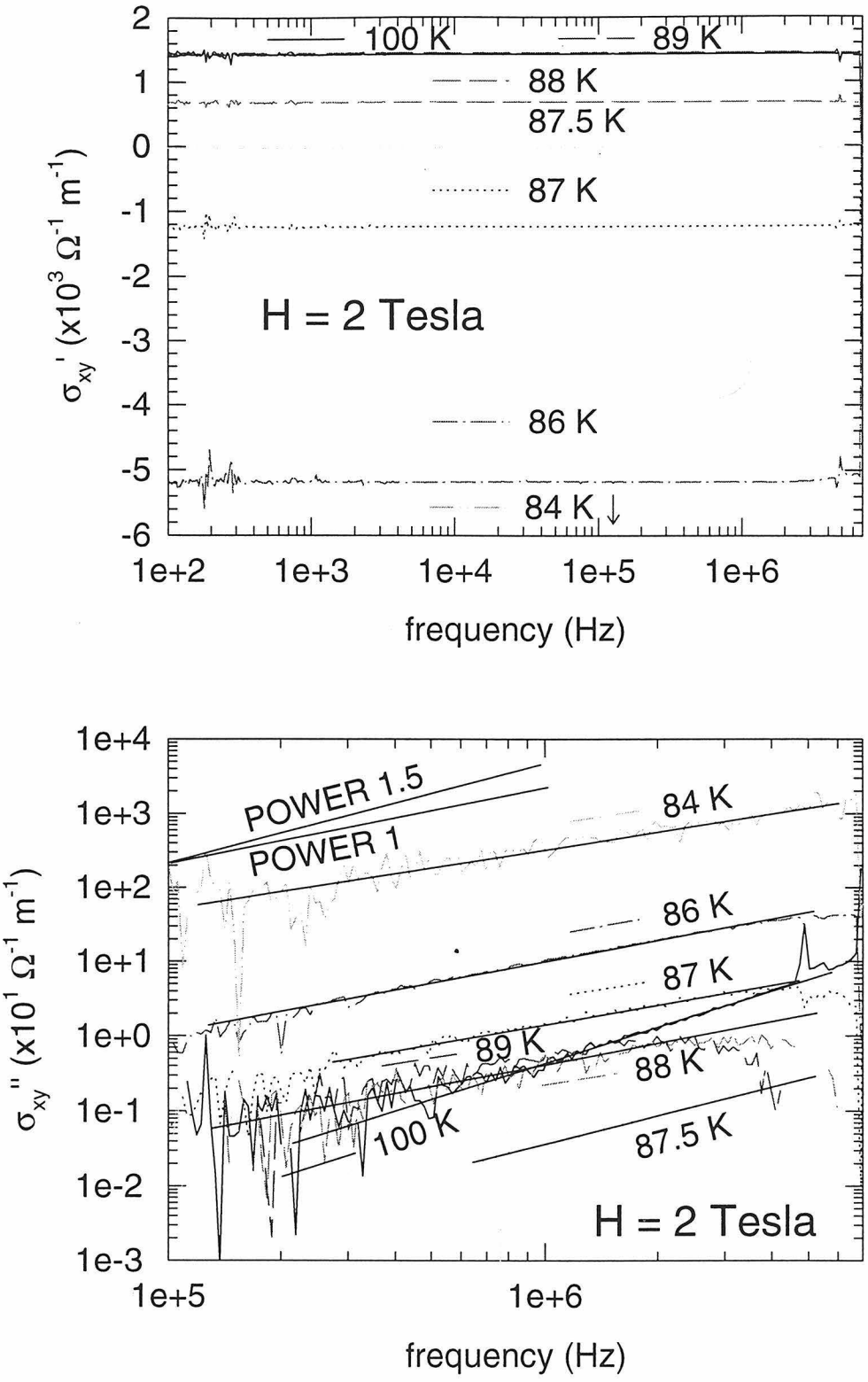

Figure 5-14 σ_{xy}' and σ_{xy}'' at various temperatures and H = 2 Tesla. (a) 84K data at -24 x 10^1 Ω^{-1} m^{-1}, (b) 88 K and 89 K data are plotted as $-\sigma_{xy}''$

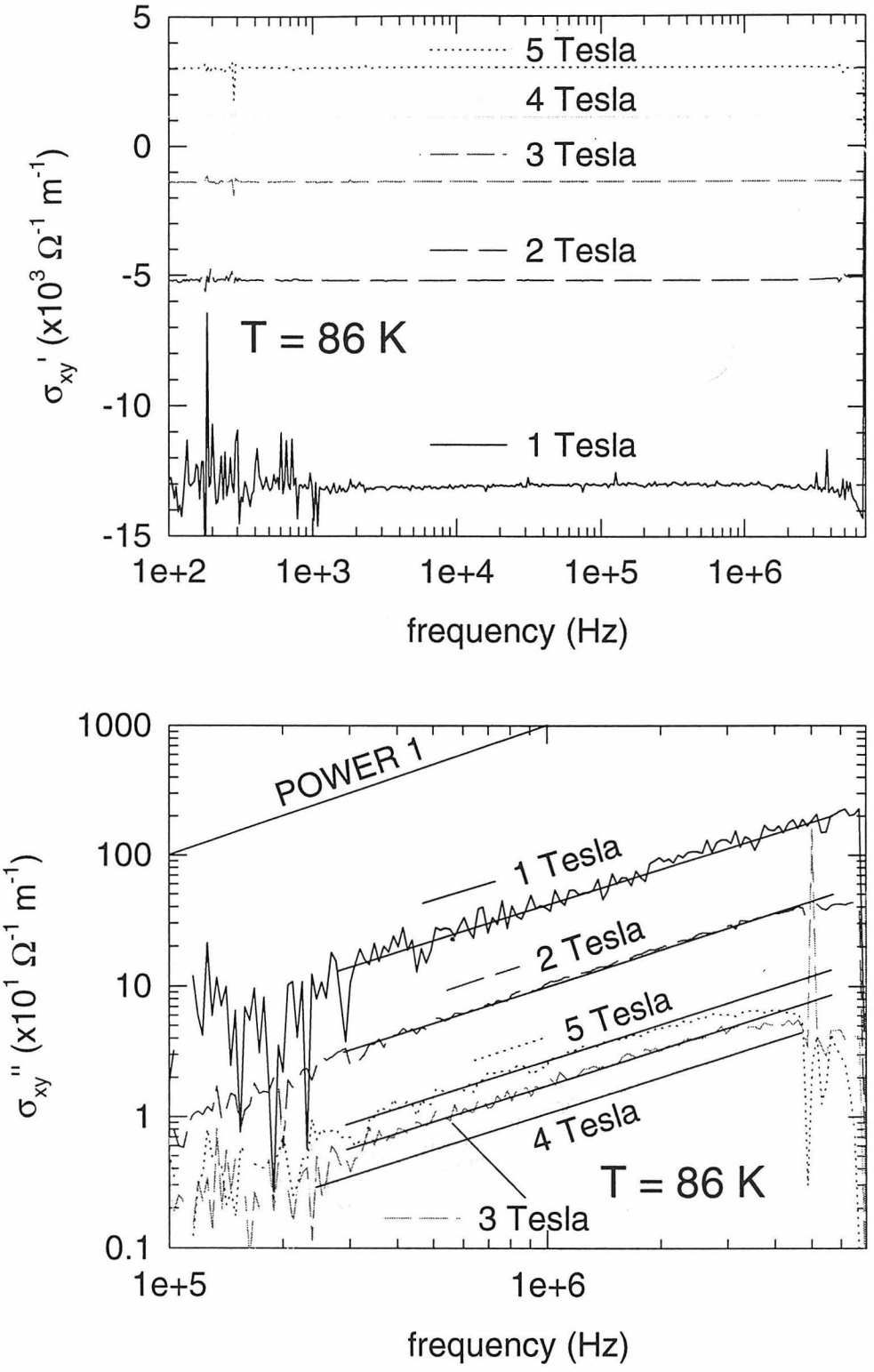

Figure 5-15 σ_{xy}' and σ_{xy}'' at various fields and T = 86 K
(b) 4 Tesla and 5 Tesla data are plotted as $-\sigma_{xy}''$

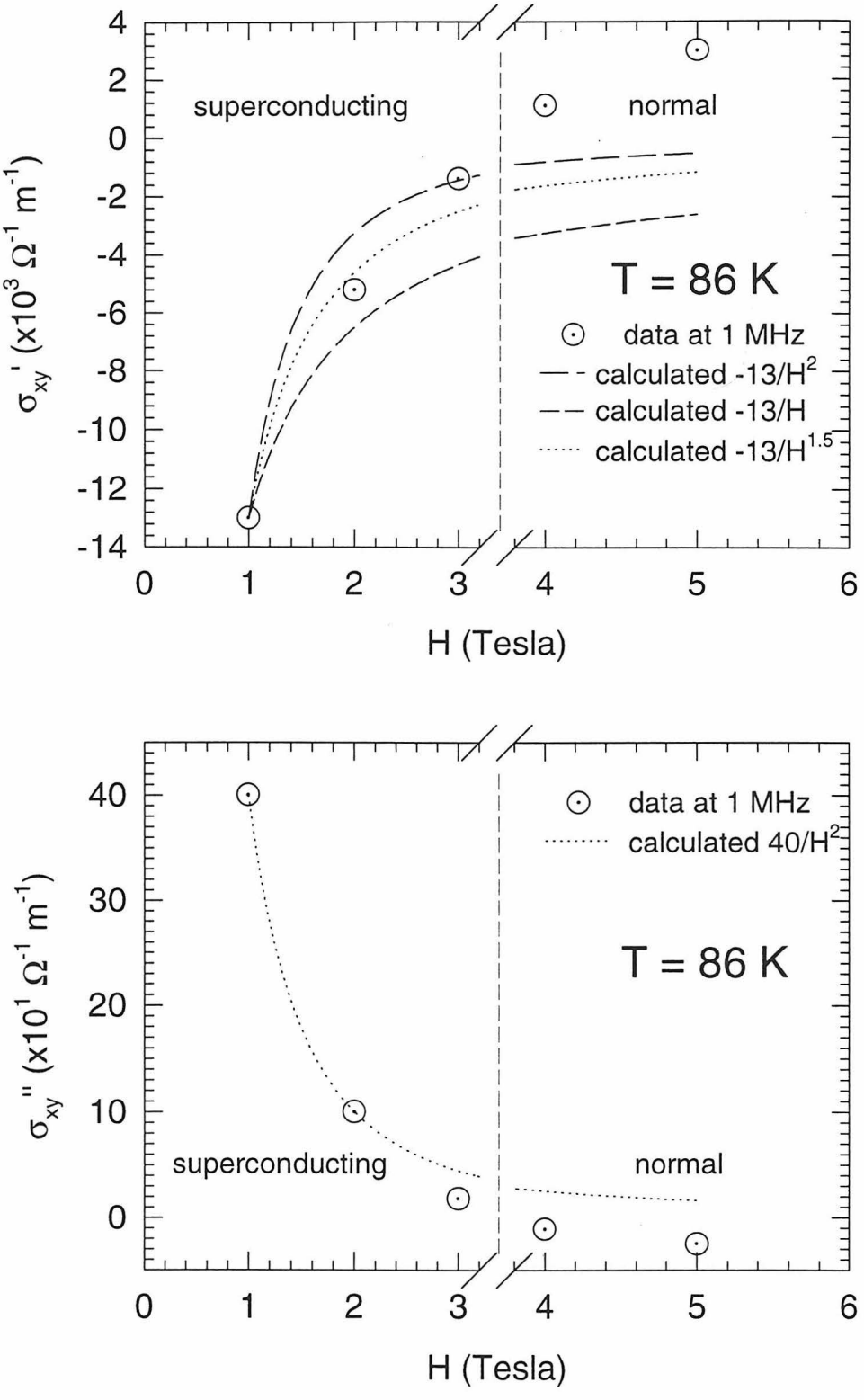

Figure 5-16 (a) σ_{xy}' vs H at 1 MHz compared with $-13/H^2$, $-13/H^{1.5}$, and $-13/H$, and, (b) σ_{xy}'' vs H at 1 MHz compared with $40/H^2$ vs H

Chapter Six: THESIS SUMMARY

This chapter is a brief description of the key developments in this thesis and closes with outlines of investigations that are logical extensions of the developments reported in this thesis.

Key Developments - DC Vortex-State Hall Conductivity

Clearly, the report of the universal vortex-state Hall conductivity of $YBa_2Cu_3O_7$ single crystals, independent of density and orientation of columnar defects, supported by experiment, is the highlight of the DC work. This is particularly enlightening in view of the strong effect correlated defects have on the vortex-state Hall and longitudinal resistivities, and that there is no theory predicting the defect independence. That the correlated defects also had no effect on the anisotropy of the Hall conductivity, independent of the orientation of the of the columnar defects, is also interesting. (The anisotropic Hall effect was accounted for using the effective mass anisotropic scaling transformation, independent of the presence or absence of columnar defects.) Although mass anisotropic scaling of as-grown $YBa_2Cu_3O_7$ single crystals had previously been reported (Harris, et al., 1994), this work and (Beam et al., 1997) are the first reports of scaling $YBa_2Cu_3O_7$ single crystals versus temperature. That the scaling occurred independent of the density and orientation of the columnar defects makes this report all the more important.

Key Developments - AC Vortex-State Hall Conductivity

A new technique to determine the AC vortex-state Hall conductivity was developed (the AC Hall conductivity setup and calibration procedures) and validated (the linear field dependence of the normal-state Hall resistivity, and the field independence, except for paraconductivity, of the longitudinal resistivities), a new device was made (the low noise, high gain differential amplifier), old technology (read as, initially thought inappropriate for the application, even by the "expert" (Honda, 1996)) was adapted to new uses (using a device, the HP 4194A, designed to measure a two-port device under test for four-point measurements, and developing cable length compensation to be able to measure samples at a distance of more than twice the rated distance from the HP 4194A), a new experiment was conducted (the first look at complex Hall conductivity in the 100 to 7 MHz frequency range), novel and meaningful results were obtained (temperature and field dependencies of the complex vortex-state Hall resistivity and conductivity versus frequency), and compared with a theoretical model developed by Yeh (1997) from the DC model by Feigel'man et al.(1995), and a theoretical model was ended (that of Spielman et al., (1994)).

The key scientific developments of the AC vortex-state Hall conductivity work are fortunately experimental and theoretical. Experimentally, the observation of frequency independence of the real part of the complex vortex-state Hall conductivity, $\sigma_{xy}' \propto \omega^0$, and the linear frequency dependence of the imaginary part of the complex vortex-state Hall conductivity, $\sigma_{xy}'' \propto \omega$, and the decreasing vortex-state Hall conductivity with increasing

field are the key experimental results of the AC Hall conductivity work. The key theoretical contributions are the verification of the importance of vortex contribution to the vortex-state Hall conductivity, as suggested in the model by Feigel'man et al.(1995), and the added requirement of a component of Hall conductivity due to vortices in the model by Spielman et al.(1994).

Possible Extensions of the DC Experiment

(1) Critical scaling of the vortex-state Hall conductivity near the vortex-solid to vortex liquid phase transition. One approach to these measurements is using patterned thin film samples so that van der Pauw corrections, not applicable in nonlinear regimes, will not be necessary.

(2) A study of the vortex-state Hall conductivity in the thermally activated flux flow regime. (Although this work resolves the scientific debate about the effect of defects on Hall conductivity in the flux-flow regime, where the van der Pauw corrections were valid, interesting defect dependent behavior was observed in the regime in the raw resistances just below, in field or temperature, the flux-flow regime.) One approach to these measurements is using patterned thin film samples.

(3) An obvious experiment is to determine at what density of columnar defects the universal Hall conductivity breaks down, and that as a function of current density.

(4) Although the theoretical model by Feigel'man et al. is consistent with the majority of this work, the development of the model is clearly limited in temperature range, and does not clearly incorporate anisotropic mass scaling. In particular, the model implies using the thermodynamic reduced temperature, T / T_c, as a parameter, but a superconductor in a magnetic field becomes normal (ignoring fluctuation effects) at the upper critical temperature, T_{c2}. The model therefore implies features of superconductivity, that is the sample is mostly superconducting, well into the normal regime. Therefore, one necessary improvement is the incorporation of the magnetic field effects into the superconducting energy gap, Δ, so that $\Delta = \Delta(T, H)$, and $\Delta = 0$ at $T = T_{c2}$.

Possible Extensions of the AC Experiment

(1) Although a $YBa_2Cu_3O_7$ thin film was used for the complex vortex-state Hall conductivity, to ensure a significant signal-to-noise ratio for the newly developed technique, a single crystal could have also been used. To use a single crystal, one must add an additional linear amplifier (easily commercially obtained, e.g., from Analog Modules), and a variable attenuator with at least 1 dB resolution. The additional linear amplifier, in series after the 42 dB differential amplifier, will provide sufficient signal to noise for the HP 4194A, but will also probably over drive the HP 4194A, as the linear amplifier typically (reduced cost) has a fixed gain. To compensate for the fixed gain of

the commercially obtained linear amplifier, the least expensive option is the variable attenuator. The signal level is then simply adjusted, with the attenuator, to the proper input signal range of the HP 4194A.

(2) Increasing the frequency range of study. The 42 dB differential amplifier has a bandwidth from DC to more than 110 MHz. The limitation of bandwidth in this work was the HP 4194A. Two ways to increase the bandwidth of the AC experiment are to move the HP 4194A closer to the sample (the inexpensive solution, e.g., building a platform so that the HP 4194A terminals are in close proximity to the connectors of the sample probe; a saving of almost 1 m in cable length and a corresponding increase in useful frequency range of several MHz), and obtaining a high-frequency lock-in amplifier. Clearly, if a shorter probe was built, combined with moving the HP 4194A close to the probe, it is possible to reduce the cable length (closed potential path distance) to about 2.5 to 3 meters.

(3) Critical scaling of the complex vortex-state Hall conductivity as a function of frequency.

(4) Investigation of the vortex dynamics in the thermally activated flux flow regime.

Bibliography

Anderson P. W., 1962 Phys. Rev. Lett. **9**, 309.

Anderson, P. W., and Y. B. Kim, 1964, Rev Mod Phys 36, 39.

Almasan, C. C., S. H. Han, K. Yoshiara, M. Buchgeister, D. A. Gajewski, L. M. Paulius, J. Herrmann, M. B. Maple, A. P. Paulikas, C. Gu, and B. W. Veal, 1995, Phys. Rev. B **51**, 3981.

Ao, P., 1995, J. Superconductivity **8**, 503.

Audouard, A., E. Balanzat, S. Bouffard, J. C. Jousset, A. Chamberod, A. Dunlop, D. Lesuer, G. Fuchs, R. Spohr, J. Vetter, and L Thomé, 1990, Phys. Rev. Lett. **65**, 875.

Bardeen, J., L. N. Cooper, and J. R. Schrieffer, 1957, Phys. Rev. **108**, 1175.

Bardeen, J., and M. J. Stephen, 1965, Phys Rev. **140**, 1197A.

Beam, D. A., N.-C. Yeh, and F. Holtzberg, 1997, Phys. Rev. Lett. (submitted).

Beck, R. G., D. E. Farrel, J. P Rice, D. M. Ginsberg, and V. G. Kogan, 1992, Phys. Rev. Lett. **68**, 1594.

Bednorz, J. G., and K. A. Müller, 1986, Z. Phys. B - Condensed Matter **64**, 189.

Blatter, G., V. B. Geshkenbein, and A. I. Larkin, 1992, Phys. Rev. Lett. **68**, 875.

Blatter, G., M. V. Feigel'man, V. B. Geshkenbein, A. K. Larkin, V. M. Vinokur, 1994, Rev. Mod. Phys. **66**, 1125.

Bonn, D. A., P. Dosanjh, R. Liang, and W. N. Hardy, 1992, Phys. Rev. Lett. **68**, 2390.

Bonn, D. A., R. Liang, T. M. Riseman, D. J. Baar, D. C. Morgan, K. Zhang, P. Dosanjh, T. L. Duty, A. MacFarlane, G. D. Morris, J. H. Brewer, W. N. Hardy, C. Kallin, and A. J. Berlinsky, 1993, Phys. Rev. B **47**, 11 314.

Bonn, D. A., S. Kamal, K. Zhang, R. Liang, D. J. Baar, E. Klein, and W. N. Hardy, 1994, Phys. Rev. B **50**, 4051.

Budhani, R. C., S. H. Liou, and Z. X. Cai, 1993, Phys. Rev. Lett. **71**, 621.

Caroli, C., and K. Maki, 1967, Phys. Rev. **164**, 591.

Chen, J. L., and T. J. Yang, 1994, Phys. Rev. B **50**, 4064.

Clinton, T. W., A. W. Smith, Q. Li, J. L. Peng, R. L. Greene, C. J. Lobb, M. Eddy, and C. C. Tsuei, 1995, Phys. Rev. B **52**, R7046.

Civale, L., A. D. Marwick, T. K. Worthington, M. A. Kirk, J. R. Thompson, L. Krusin-Elbaum, Y. Sun, J. R. C.em, and F. Holtzberg, 1991, Phys. Rev. Lett. **67**, 648.

Colino, J., M. A. Gonzalez, J. I. Martín, M. Velez, D. Oyola, P. Prieto, and J. L. Vicent, 1994, Phys. Rev. B **49**, 3496.

Dorsey, A. T., 1992, Phys. Rev. B **46**, 8376.

Durán, C., P. L. Gammel, R. Wolfe, V. J. Fratello, D. J. Bishop, J. P. Rice, and D. M. Ginsberg, 1992, Nature **357**, 474.

Feigel'man, M. V., V. B. Geshkenbein, A. I. Larkin, and V. M. Vinokur, 1989, Phys. Rev. Lett. **63**, 2303.

Feigel'man, M. V., V. B. Geshkenbein, A. I. Larkin, and V. M. Vinokur, 1995, JETP Lett. **62**, 834.

Ferrell, R. A., 1992, Phys. Rev. Lett. **68**, 2524.

Fleshler, S., W.-K. Kwok, U. Welp, V. M. Vinnokur, M. K. Smith, J. Downey, and G. W. Crabtree, 1993, Phys. Rev. B **47**, 14 448.

Freimuth, A., C. Hohn, and M. Galffy, 1991, Phys. Rev. B **44**, 10 396.

Geshkenbein, V. B., and A. I. Larkin, 1994, Phys. Rev. Lett. **73**, 609.

Galffy, M. and E. Zirgiebl, 1988, Solid State Comm. **68**, 929.

González, M. A., P. Prieto, D. Oyola, and J. L. Vicent, 1991, Physica C **180**, 220.

Gurevich, A., 1992, Phys. Rev. B **46**, 3187.

Gyorgy, E. M., R. B. van Dover, K. A. Jackson, L. F. Schneemeyer, and J. V. Waszczak, 1989, APL **55**, 283.

Hagen, S. J., C. J. Lobb, R. L. Grene, M. G. Forrester, and J. H. Kang, 1990, Phys. Rev. B **41**, 11 630.

Hagen, S. J., C. J. Lobb, and R. L. Green, 1991, Phys. Rev. B **43**, 6246.

Hagen, S. J. A. W. Smith, M. Rajeswari, J. L. Peng, Z. Y. Li, R. L. Greene, S. N. Mao, X. X. Xi, S. Bhattacharya, Q. Li, and C. J. Lobb, 1993, Phys. Rev. B **47**, 1064.

Hall, E. H., 1879, Amer. J. Math., **2**, 287.

Harris, J. M., N. P. Ong, and Y. F. Yan, 1993, Phys. Rev. Lett. **71**, 1455.

Harris, J. M., P. Matl, N. P. Ong, Y. F. Yan, T. Kimura, and K. Kitazawa, 1994, Physica C. **235-240**, 235.

Harris, J. M., N. P. Ong, P. Matl, R. Gagnon, L. Taillefer, T. Kimura, and K. Kitazawa, 1995, Phys. Rev. B **51**, 12 053.

Hirsch, J. E., and F. Marsiglio, 1991, Phys. Rev. B **43**, 424.

Hofmann, S., and R. Kümmel, 1993, Phys. Rev. Lett. **70**, 1319

Honda, M., 1989 The Impedance Measurement Handbook, M. Honda, Yokogawa-Hewlett-Packard LTD.

Iye, Y., S. Nakamura, and T. Tamegai, 1989, Physica C **159**, 616.

Jeandupeux, O., et al., 1996, Phys. Rev. B **53**, 12 475.

Jiang, W., N.-C. Yeh, D. S. Reed, U. Kriplani, T. A. Tombrello, A. P. Rice, and F. Holtzberg, 1993, Phys. Rev. B **47**, 8308.

Jiang, W., N.-C. Yeh, D. S. Reed, U. Kriplani, D. A. Beam, M. Konczykowski, T. A. Tombrello, and F. Holtzberg, 1994, Phys. Rev. Lett. **72**, 550.

Kang, W. N., D. H. Kim, S. Y. Shim, J. H. Park, T. S. Hahn, S. S. Choi, W. C. Lee, J. D. Hettinger, K. E. Gray, and B. Glagola, 1996, Phys. Rev. Lett. **76**, 2993.

Kes, P. H., J. Aarts, J. van den Berg, C. J. van der Beek, and J. A. Mydosh, 1989, Supercond. Sci. Technol. **1**, 242.

Khomskii, D. I., and F. V. Kusmartsev, 1992, Phys. Rev. B **46**, 14 245.

Khomskii, D. I., and A. Freimuth, 1995, Phys. Rev. Lett. **75**, 1384.

Konczykowski, M., F. Rullier-Albenque, Ė. R. Yacoby, A. Shaulov, Y. Yeshurun, and P. Lejay, 1991, Phys. Rev. B **44**, 7167.

Konczykowski, M., 1994, private communication.

Krishana, K., J. M. Harris, and N. P. Ong, 1995, Phys. Rev. Lett. **75**, 3529.

Kwok, W. K., U. Welp, G. W. Crabtree, K. G. Vandervoort, R. Hulscher, and J. Z. Lieu, 1990, Phys. Rev. Lett. **64**, 966.

Kwok, W. K., S. Fleshler, U. Welp, V. M. Vinokur, J. Downey, G. W. Crabtree, and M. M. Miller, 1992, Phys. Rev. Lett. **69**, 3370.

Legris A., F. rullier-Albenque, and P. Lejay, 1993, Phys. Rev. B **48**, 10 634.

Liu, J. Z., Y. X. Jia, R. N. Shelton, and M. J. Fluss, 1991, Phys. Rev. Lett. **66**, 1354.

Lofland, S. E., S. M. Bhagat, M. Rajeswari, T. Venkatesan, D. Kanjilal, L. Senapati, and G. K. Mehta, 1995, Phys. Rev. B **51**, 8489.

Lofland, S. E., S. D. Tyagi, S. M. Bhagat, M. Rajeswari, T. Benkatesan, D. Kanjilal, and G. K. Mehta, 1996, Physica C **267**, 79.

Maggio-Aprile, Ch. Renner, A. Erb, E. Walker, and Ø. Fischer, 1995, Phys. Rev. Lett. **75**, 2754.

Majer, D., E. Zeldov, and M. Konczykowski, 1995, Phys. Rev. Lett. **75**, 1166.

Maki, K., 1971, Physica **55**, 124.

Mattis D. C., and J. Bardeen, 1958, Phys. Rev. **111**, 412.

Nagaoka, T., J. Matsuda, G. Sukzuki, K.-I. Kumagai, M. Suzuki, M. Sera, M. Hiroi, and N. Kobayashi, 1996, Czechoslovak J. Phys. **46**, 1755.

Nayfeh, M. H., and M. K. Brussel, 1985, Electricity and Magnetism, page 140, table 4.1, John Wiley & Sons, Inc., New York.

Nelson, D. R., and V. M. Vinokur, 1992, Phys. Rev. Lett. **68**, 2398.

Nelson, D. R., and V. M. Vinokur, 1993, Phys. Rev. B **48**, 13 060.

Niessen, A. K. and F. A. Staas, 1965, Phys. Lett. **15**, 26.

Nozières, P., and W. F. Vinen, 1966, Philos. Mag. **14**, 667.

Numssen, K., R. Schwab, T. Jacobs, R. Heidinger, and J. Halbritter, 1996, J. Low Temp Phys **105**, 1041.

Nuss, M. C., P. M. Mankiewich, M. L. O'Malley, E. H. Westerwick, P. B. Littlewood, 1991, Phys. Rev. Lett. **66**, 3305.

Olsson, H. K., R. H. Koch, W. Eidelloth, and R. P. Robertazzi, 1991, Phys. Rev. Lett. **66**, 2661.

Onsager, L., 1931, Phys. Rev. **38**, 2265.

Parks, B., S. Spielman, J. Orenstein, D. T. Nemeth, F. Ludwig, J. Clarke, P. Merchant, D. J. Lew, 1995, Phys. Rev. Lett. **74**, 3265.

Reed, D. S., N.-C. Yeh, W. Jiang, U. Kriplani, and F. Holtzberg, 1993, Phys. Rev. B **47**, 6150.

Reed, D. S., N.-C. Yeh, W. Jiang, U. Kriplani, D. A. Beam, and F. Holtzberg, 1994, Phys. Rev. B. **49**, 4384.

Reed, D. S., 1995, Ph. D. Thesis, California Institute of Technology.

Reed, D. S., N.-C. Yeh, W. Jiang, U. Kriplani, M. Konczykowski, and F. Holtzberg, 1996, Intl. J Mod. Phys. B **10**, 2723.

Reed, W. A., E. Fawcett, and Y. B. Kim, 1965, Phys. Rev. Lett. **14**, 790.

Rice, J. P., J. Giapintzakis, D. M. Ginsberg, and J. M. Mochel, 1991, Phys. Rev. B **44**, 10 158.

Rietveld, G., N. Y. Chen, and D. van der Marel, 1992, Phys. Rev. Lett. **69**, 2578.

Salamon, M. B., et al., 1993, Phys. Rev. B **47**, 5520.

Samoilov, A. V., Z. G. Ivanov, and L.-G. Johansson, 1994, Phys. Rev. B **49**, 3667.

Samoilov, A. V., A. Legris, F. Rullier-Albenque, P. Lejay, S. Bouffard, Z. G. Ivanov, and L.-G. Johansson, 1995, Phys. Rev. Lett. **74**, 2351.

Samoilov, A. V., 1994, Phys. Rev. B **49**, 1246.

Samoilov, A. V., 1997, comments submitted to Phys. Rev. Lett.

Smith, A. W., T. W. Clinton, C. C. Tsuei, and C. J. Lobb, 1994, Phys. Rev. B **49**, 12 927.

Smith, A. W., and C. J. Lobb, 1997, comments submitted to Phys. Rev. Lett.

Spielman, S., B. Parks, J. Orenstein, D. T. Nemeth, F. Ludwig, J. Clarke, P. Merchant, D. J. Lew, 1994, Phys. Rev. Lett. **73**, 1537.

Sudbø, A., E. H. Brandt, and D. A. Huse, 1993, Phys. Rev. Lett. **71**, 1451.

Tinkham, M., 1975, Introduction to Superconductivity, pages 251 to 256, Robert E. Krieger Publishing Company, Inc., Florida.

Tombrello, T. A., 1995, NIM B **95**, 232.

Ullah, S., and A. T. Dorsey, 1991, Phys. Rev. B **44**, 262.

Usui, N., T. Ogasawara, and K. Yasuukochi, 1968, Phys. Lett. A **27**, 140.

Usui, N., T. Ogasawara, K. Yasukichi, and S. Tomoda, 1969, J. Phys. Soc. Jpn. **27**, 574.

van Beelen, H., J. P. Van Braam Houckgeest, H. M. Thomas, C. Stolk, and R. De Bruyn Ouboter, 1967, Physica **36**, 241.

van der Pauw, L. J., 1958, Philips Res. Repts **13**, 1.

van der Pauw, L. J., 1961, Philips Res. Repts **16**, 187. Regarding the applicability of the van der Pauw technique to anisotropic materials, van der Pauw, in his second paper, entitled, "Determination of resistivity tensor and Hall tensor of anisotropic conductors," (van der Pauw, 1961) addresses "The resistivity tensor of an anisotropic conductor with respect to an arbitrarily chosen rectangular coordinate system..." Wasscher (1961, Philips Res. Repts 16, 301) and Montgomery (1971, J. Applied Phys **42**, 2971) demonstrate that for a square or rectangular geometry of the sample "...the three principal values of a resistivity tensor can be calculated from measurements on only the lane perpendicular to a direction corresponding to one of these principal values."

van Otterlo, A., M. Feigel'man, V. Geshkenbein, and G. Blatter, 1995, Phys. Rev. Lett. **75**, 3736.

Vlasko-Vlasov, V. K., L. A. Dorosinskii, A. A. Polyanskii, V. I. Nikitenko, U. Welp, B. W. Veal, and G. W. Crabtree, 1994, Phys. Rev. Lett. **72**, 3246.

Vinokur, V. M., M. V. Feigel'man, V. B. Geshkenbein, and A. I. Larkin, 1990, Phys. Rev. Lett. **65**, 259.

Vinokur, V. M., V. B. Geshkenbein, M. B. Feigel'man, and G. Blatter, 1993 Phys. Rev. Lett. **71**, 1242.

von Hipple, A. R., 1954, editor, Dielectric Materials and Applications, pages 332 and 327, The Technology Press of M. I. T and John Wiley & Sons, Inc. New York.

Wang, X. X., and Y. Y. Ting, 1991 Phys. Rev. Lett. **67**, 3618.

Wei, J. Y. T., C. C. Tsuei, P. J. M. van Bentum, Q. Xiong, C. W. Chu, and M. K. Wu, 1997, Phys. Rev. B submitted.

Weijsenfeld, C. H., 1968, Phys. Lett. **28A**, 362.

Yeh, N.-C., D. S. Reed, W. Jiang, U. Kriplani, F. Holtzberg, A. Gupta, B. D. Hunt, R. P. Vasquez, M. C. Foote, and L. Bajuk, 1992, Phys. Rev. B **45**, 5654.

Yeh, N.-C., D. S. Reed, W. Jiang, U. Kriplani,C. C. Tsuei, C. C. Chi, and F. Holtzberg, 1993, Phys. Rev. Lett. **71**, 4043.

Yeh, N.-C., 1997, private communications.